Critical Behaviour and Quantum Properties in (Ga,Mn)As

Robin Alexander Marshall

The University of Nottingham

School of Physics and Astronomy

Ferromagnetic Semiconductors and Spintronics

Professor B. L. Gallagher

September 2012

Abstract

Spintronics is a rapidly developing field in solid state physics based on the quantum property of spin angular momentum. It has the potential to offer a new generation of electronic devices exploiting spin properties instead of, or in addition to, charge. Such quantum-based devices are expected to demonstrate significant advantages over traditional charge based electronics with a promise of faster data processing speeds and lower power consumption.

One of the most widely studied spintronic materials is the dilute magnetic semiconductor gallium manganese arsenide ((Ga,Mn)As). This continues to be a valuable test ground for spintronics applications due to its close relation to the traditional, and well-characterised, semiconductor GaAs, and its relatively high Curie temperature despite values remaining some way off the much sought-after room temperature.

The two primary focuses of this thesis are phase-coherent transport and critical phenomena, both of which whilst well understood in metals have seen limited work in (Ga,Mn)As. Critical behaviour in particular has not been extensively studied despite continued disputes over theoretical models and resistance peak positions relative to Curie temperature.

Studies of both these areas are presented within this thesis split over four main chapters. The first of these chapters acts as a general introduction to spintronics, and includes both a brief history of the subject, and a theoretical overview focused on the structure and properties of (Ga,Mn)As. This introductory chapter also includes an in-depth review of nanofabrication including typical processing techniques and their applications to the study of spintronics in Nottingham.

The second chapter presents a comprehensive study of critical phenomena within (Ga,Mn)As, showing how the behaviour of magnetic properties close to T_c are strongly correlated between samples. Both magnetisation and susceptibility are found to demonstrate behaviour very close to that predicted by the Heisenberg model; a result in strong agreement with theoretical work.

The study of critical behaviour is carried over into the third chapter with transport measurements showing that resistance data can be directly used to accurately measure sample Curie temperature by finding the peak in the derivative $\frac{\mathrm{d}R}{\mathrm{d}T}$. This potentially offers an alternate approach to calculating T_c that is faster and cheaper than the more conventional magnetometry or Arrott plot methods. Analysis is also carried out on the resistance peak which is expected to follow the critical behaviour of the specific heat.

The final experimental chapter focuses on the development of nanoring fabrication processes in (Ga,Mn)As including the difficulties associated with fabricating nanoscale structures, the testing performed to achieve high quality, reproducible structures, and the final adopted recipe. This chapter then details early test measurements on these devices including an initial study on the first structures within a dilution refrigerator, and prelimenary work on a second improved batch at ^{4}He temperatures. This work will act as a foundation for the future aim of conducting a full phase-coherence phenomena study in highly optimised (Ga,Mn)As samples grown in Nottingham.

Acknowledgements

I would like to thank everyone who has helped to make my Ph.d possible and made it such an enjoyable experience; it has been a pleasure to work as part of such a wonderful group. First and foremost I would like to express my gratitude toward my supervisor Prof. Bryan Gallagher, both for giving me the opportunity to work in Nottingham, and for having the patience to offer continued support and guidance even during the more difficult latter stages. I am also very grateful to both Prof. Kevin Edmonds and Dr. Andrew Rushforth whose advice throughout my time in Nottingham has proven invaluable.

I would like to offer my sincerest thanks to everyone who has contributed toward the studies covered in this thesis. These include Dr. Richard Campion for growing the (Ga,Mn)As samples, Dr. Oleg Makarovsky for his early guidance with my very first low-temperature measurements, Dr. Ehsan Ahmad for teaching me how to use the SEM system, and guiding me in my first steps toward nanoring fabrication, and Dr. Chris Mellor for help and suggestions throughout the nanoring fabrication processing, and for setting up and organising the first dilution refrigerator measurements. I would also like to thank all the technicians, in particular Jas Chauhan and Dave Taylor in the cleanroom, Bob Chettle and Steve Booth in the electronics workshop, and Chris Pallendar for providing the liquid helium without which none of the measurements would have been possible.

I would also like to thank all of my friends and colleagues in office, past and present, who helped me through the highs and lows of Ph.D life both in and out of the lab. Thank you for the constant support and encouragement, and for making Nottingham such a fun place to be. I couldn't have done it without you guys. And finally, a special thank you to Dr. Mu Wang whose unrelenting and

insuppressible enthusiasm is only matched by his willingness to help. Thanks Mu, you've always gone above and beyond to help, but more importantly you've always been a great friend!

Contents

Chapter 1

Introduction and Background Theory

1.1 Introduction

Whilst modern silicon-based electronics continues to drive the industry forward the fundamental physics behind these devices has not significantly changed. Current technology is capable of producing, and makes extensive use of, nanoscale structures, but even for these the physics behind them remains purely classical-based. Any quantum effects demonstrated in such devices are generally seen as unwanted and can result in leakage or inefficiency.

This changed in 1988 when a potential new door for future electronics was opened in the form of giant magnetoresistance (GMR) observed within multilayer structures of iron and chromium (Baibich *et al.* (1988); Binasch *et al.* (1989)). Large changes in resistance resulted from the alignment of magnetic moments of successive ferromagnetic layers due an applied magnetic field with the effects found to be an order-of-magnitude greater than ordinary magnetoresistance previously seen in metals. This behaviour not only demonstrated that charge carrier spin could potentially be used within standard devices, but also introduced the possibility of a wide variety of completely original quantum-based structures. The GMR effect has since been widely exploited by hard drive manufacturers with the success of this technique ultimately leading to the 2007 Nobel Prize in physics being awarded to Albert Fert and Peter Grünberg for its discovery.

Interest in this area of physics has inevitably flourished due to the promise of faster data processing speeds and lower power consumption. The most prominent research in recent years has focused on spin polarisation within the field of spintronics creating a non-equilibrium spin population to manipulate electron flow. Prototype spintronic devices such as that used in hard drive read heads employed GMR within metallic structures due to the widespread availability of ferromagnetic metals. However, for full future electronics integration there are a number of fundamental requirements not met by such materials. The most notable of these is that the material should demonstrate standard semiconductor properties such as sensitivity to doping and external gate applied electric fields, both of which are widely used in conventional devices. Current research is therefore focused on ferromagnetic semiconductors with the much sought-after possibility of combining the physics of semiconductor electronics with that of magnetic data storage.

Despite this sudden increase of interest ferromagnetic semiconductors are not a new concept (Mauger and Godart (1986)), with carrier-mediated ferromagnetism demonstrated some time ago at liquid helium temperatures in PbSnMnTe (Story *et al.* (1986)). However, it is the alternative method of introducing local moments into well understood compound semiconductors originally pioneered in the late 1970s (Gaj *et al.* (1978); Jaczynski *et al.* (1978)) that has promoted such attention. Spurred on by the initial fabrication of (In,Mn)As (Munekata *et al.* (1989)) the resulting dilute magnetic semiconductors (DMSs) lead to a huge resurgence of research in the field (Munekata *et al.* (1993); Ohno *et al.* (1992, 1996); van Esch *et al.* (1997); Hayashi *et al.* (1997); Ohno (1998)) with several III-V compound semiconductors shown to become ferromagnetic when heavily doped with manganese. The resulting research has lead to huge steps being made in the understanding of the origins of ferromagnetism within such systems (Ohno (1999); MacDonald *et al.* (2005)), the optimisation of sample growth (Campion *et al.* (2003); Wang *et al.* (2005b)), and the increase of transition temperature (Matsukura *et al.* (1998); Wang *et al.* (2005a); Wang *et al.* (2008)).

This work on the doped III-V compounds has meant that one of the most widely studied spintronic materials is gallium manganese arsenide ((Ga,Mn)As) due in part to its relation to GaAs, the second most widely used semiconductor in modern electronics. In the case of (Ga,Mn)As dopant manganese (Mn) ions are substituted into the GaAs structure with the most stable position in the lattice on the gallium (Ga) site. Incorporated manganese then act as acceptors resulting in valence band holes that mediate ferromagnetic interactions.

Ferromagnetism is, however, only observed within systems with a gallium substitution greater than 1%; a value significantly higher than the equilibrium solubility limit of 0.1% (Jungwirth *et al.* (2006)). Nevertheless developments in growth techniques and post-processing have resulted in a steady rise in Curie temperatures from the initial record of 110 K (Matsukura *et al.* (1998)), with the latest samples in excess of 185 K (Wang *et al.* (2008); Olejník *et al.* (2008)). Theoretical calculations have predicted room-temperature ferromagnetism with a 10% Mn substitution (Jungwirth *et al.* (2005)), but this still remains a long way off with the slow progress in recent years suggesting that such a goal may never be attainable in this system.

Despite the ramifications of this to future practical applications, the quantum properties of (Ga,Mn)As are still widely studied due to the potential knowledge and insight gained being applicable to other promising spintronic materials. The main aims of this thesis are therefore to investigate the magnetic properties of (Ga,Mn)As with the principal focuses on phase coherence within nanoring structures and critical behaviour close to the sample Curie temperature.

The remaining sections of this chapter focus on the properties of (Ga,Mn)As including background theory behind the origins of its ferromagnetism, the basic crystallographic structure and electron configuration, material growth, as well as some of the standard techniques used to characterise samples. A comprehensive overview of nanofabrication is also given in this chapter, felt necessary by the amount of time invested in device fabrication for these studies, and its general applicability to most (Ga,Mn)As research. The thesis then comprises three chapters with the first of these presenting an in-depth study on the critical behaviour of the magnetic properties of high quality (Ga,Mn)As samples. Chapter 3 then revisits this subject focusing on the transport properties close to T_c, and the often refuted method of T_c measurement via resistance-temperature peak position.

Chapter 4 presents a study of (Ga,Mn)As nanoring devices with a large section devoted to their fabrication acting as a continuation of the general overview covered in section 1.4. This details the exact recipes and processes used to define the rings, and some of the preliminary work performed. This chapter also covers the initial measurements performed on these structures with the future aim of studying the Aharonov-Bohm effect and phase coherence within (Ga,Mn)As at dilution refrigerator temperatures. Specialised theory sections regarding phase coherence and critical phenomena are covered in their respective chapters with further information regarding the equipment used given in appendix B.

Appendix C details an earlier study of the low-temperature magnetoresistance properties of (Ga,Mn)As thin-films following on from previous work performed in Nottingham by Dr. Kaiyou Wang. Unlike these original studies measurements were performed at much lower millikelvin temperatures with data demonstrating corrections to the resistance at low applied magnetic fields due to weak localisation. Such quantum mechanical corrections are expected to be suppressed within perpendicular magnetic fields which in the past has raised the question as to whether these effects could be observed within ferromagnetic systems which have an intrinsic magnetic induction.

Past studies of this behaviour in (Ga,Mn)As have been limited (Neumaier *et al.* (2007); Rokhinson *et al.* (2007)) despite the system potentially offering the opportunity for a more definite experimental answer due to its small internal field compared to that of conventional ferromagnets. Whilst unfinished this study offers some insight into the magnetotransport behaviour of Nottingham-grown (Ga,Mn)As samples at millikelvin temperatures and the the effects of quantum mechanical corrections that could prove useful for the Aharonov-Bohm nanoring work presented in chapter 4.

1.2 Gallium Manganese Arsenide

From a fundamental perspective (Ga,Mn)As is now considered to be a textbook example of a rare group of DMSs that exhibit ferromagnetic behaviour due to a coupling of the dilute magnetic moments via delocalised charge carriers; both provided by the dopant manganese. It is this ferromagnetism that has lead to (Ga,Mn)As and several other (III,Mn)V DMSs being the most popular within spintronics with the first viable magnetic semiconductors based on the II-VI semiconductors only demonstrating paramagnetic behaviour. (Ga,Mn)As itself also has the advantage of being based on the second most widely used semiconductor, gallium arsenide (GaAs), making it easily compatible with current electronics technology.

The semiconductor GaAs has a Zinc-blende crystal structure composed of two interlocked face-centred cubic sublattices of gallium (Ga) and arsenic (As) displaced apart by $\frac{1}{4}$ of a body diagonal as shown in figure 1.2.1. This structure acts as a host for the introduced manganese (Mn) impurities with the most stable, and most favourable, position in the lattice on the gallium site ($\mathrm{Mn_{Ga}}$). The elements within (Ga,Mn)As have the atomic structure $[\mathrm{Ar}].3\mathrm{d}^{10}4\mathrm{s}^2 4\mathrm{p}^1$ for gallium, $[\mathrm{Ar}].3\mathrm{d}^5 4\mathrm{s}^2$ for manganese and $[\mathrm{Ar}].3\mathrm{d}^{10}4\mathrm{s}^2 4\mathrm{p}^3$ for arsenic. The two 4s electrons within the dopant manganese therefore take part in crystal bonding in the same way as that of the gallium. However, the gallium substitutional manganese ions also act as shallow acceptors due to the missing 4p electron, and have a localised magnetic moment of $S = \frac{5}{2}$ formed by the five occupied d-orbitals with the same spin orientations. Each ion provides a single itinerant valence band hole to the lattice, (Ga,Mn)As is thus a p-type material.

Long-range ferromagnetic ordering occurs within this system due to an anti-ferromagnetic p-d exchange interaction between the manganese acceptors and the delocalised holes. This model of carrier-mediated ferromagnetism was originally proposed by C. Zener for transitional-metal ferromagnets (Zener (1951)) with little success. However, the Zener exchange model has been applied to (Ga,Mn)As (Dietl *et al.* (2000)) assuming a merging of the manganese impurity band with the valence band with strong valence band hole spin-orbit coupling playing an important role in the magnitude of the critical temperature. Equation (1.2.1) shows the predicted relation between the Curie temperature T_c, the effective manganese density M_eff and the carrier density p that has been verified by experiment (Jungwirth *et al.* (2005)).

$$T_\mathrm{c} \propto M_\mathrm{eff} p^{\frac{1}{3}} \tag{1.2.1}$$

The result of this is that (Ga,Mn)As should have near-ideal controllable mag-

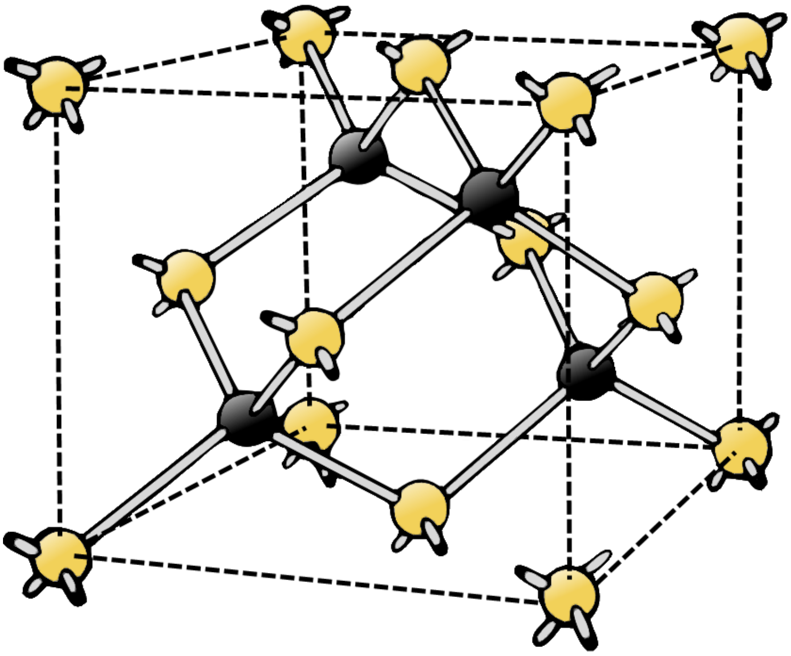

Figure 1.2.1: The zinc-blende structure of GaAs with gallium lattice sites represented in yellow and arsenic in black.

netic properties with theoretical calculations based on the Zener exchange model predicting room-temperature ferromagnetism in 10% manganese samples. Unfortunately, this model does not take into account the effects of disorder within the system that can significantly reduce T_c. Ferromagnetism is only observed on the metallic side of the Mott insulator-metal transition for substitution greater than 1%, well above the 0.1% equilibrium solubility limit. A non-equilibrium growth method is therefore required in order to avoid the formation of unwanted, but energetically favourable, Mn-rich precipitates such as manganese arsenide (MnAs). The use of such a non-equilibrium growth leads to defects within the structure which act to compensate the desired effects of the substitutional manganese.

In an ideal (Ga,Mn)As sample the carrier concentration is equal to that of the manganese with all impurity ions occupying substitutional positions within the GaAs lattice. Such a system is not realised in practice due to the presence of a number of other metastable impurity states within the structure because of the non-equilibrium growth process. The most important of these are the incorporation of manganese ions between lattice sites in interstitial states

($\mathrm{Mn_{int}}$), and the addition of arsenic on gallium antisites ($\mathrm{As_{Ga}}$). These both act as double donors therefore compensating two substitutional holes. Interstitial manganese atoms also act to compensate the $\mathrm{Mn_{Ga}}$ local moments by forming close pairs with substitutional atoms due to anti-ferromagnetic coupling. Both of these effects are clearly undesirable when growing high T_c (Ga,Mn)As samples with a serious effect on the electric and magnetic properties. The substitutional $\mathrm{Mn_{Ga}}$, interstitial $\mathrm{Mn_{int}}$ and $\mathrm{As_{Ga}}$ antisite positions are all shown within the GaAs crystal structure in figure 1.2.2.

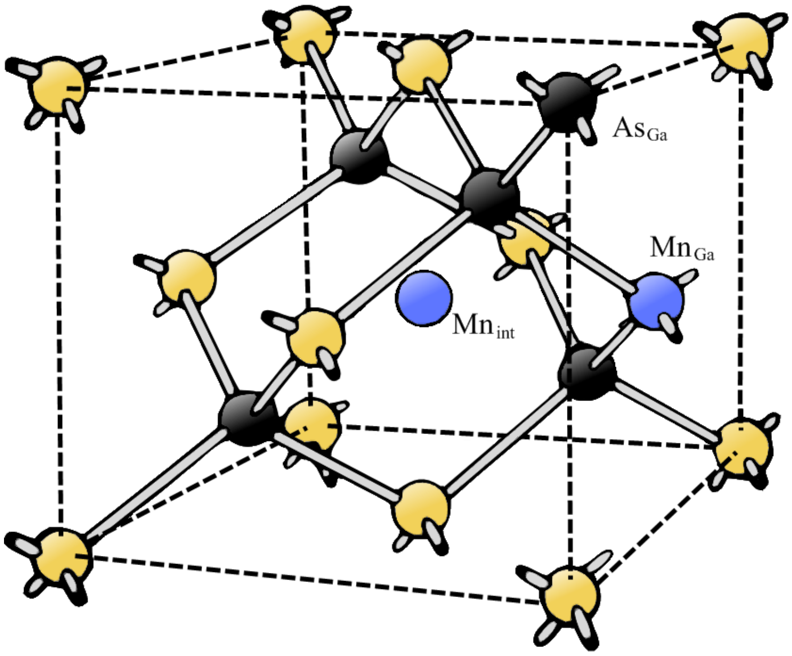

Figure 1.2.2: The lattice structure of (Ga,Mn)As based on the GaAs structure shown in figure 1.2.1 with the addition of both substitutional $\mathrm{Mn_{Ga}}$ and interstitial manganese $\mathrm{Mn_{int}}$ shown in blue, and an example of an arsenic antisite defect $\mathrm{As_{Ga}}$. As can be seen from this image the interstitial manganese atom does not occupy a position on the lattice and has no bonds to other atoms thus resulting in the donation of two 4s electrons.

1.3 Molecular Beam Epitaxy

The standard non-equilibrium growth process used to produce (Ga,Mn)As is low-temperature molecular beam epitaxy (MBE), first employed in (III,Mn)V semiconductors in the growth of (In,Mn)As (Munekata *et al.* (1989)). This process allowed doping levels high enough to make the first observations of ferromagnetism within DMS materials and has gradually been optimised to produce ever higher manganese concentration samples with corresponding increases in T_c.

Molecular beam epitaxy was originally developed for the growth of compound semiconductors in the late 1960s (Cho (1970)), and is essentially a refined ultra-high-vacuum (UHV) evaporation method for producing thin epitaxial structures. As implied by the name, beams of atoms or molecules of the required materials constituents are used as a source to form an ordered arrangement of atoms on a growth substrate. This substrate is sufficiently heated to provide enough thermal energy to the arriving atoms for them to migrate over the surface to lattice sites. The UHV environment is required in order to reduce contamination of the growth surface and allows beam atoms to take near-collision-free paths before arriving at the substrate. The use of a UHV also permits the use of a variety of analytical methods to monitor the substrate before, after and even during the growth process. A typical growth temperature for GaAs is 550°C with very slow rates of roughly one monolayer per second ensuring a two-dimensional growth and allowing single layer thickness control with the use of fast shutters. MBE is also a relatively simple process in comparison to other growth techniques and can be explained with simplified models resulting in a greater understanding and therefore the possibility of higher quality materials.

A schematic diagram of a typical MBE growth chamber is shown in figure 1.3.1. During growth a crystalline substrate is mounted onto the rotating holder and separate Knudsen effusion cells used to produce the required beams of atoms or molecules by heating ultra-pure elements such as gallium and arsenic until atoms of the source material are able to escape by evaporation or sublimation. Mechanical shutters are then used to regulate the fluxes from each source oven effectively turning the beams on and off. The walls of the growth chamber are liquid nitrogen cooled in order to condense unused source atoms thus retaining the UHV environment of the system and preserving the purity of the growing film. Samples are rotated during the growth process to reduce the effects of non-uniform beam fluxes and concentration gradients across the wafer caused by

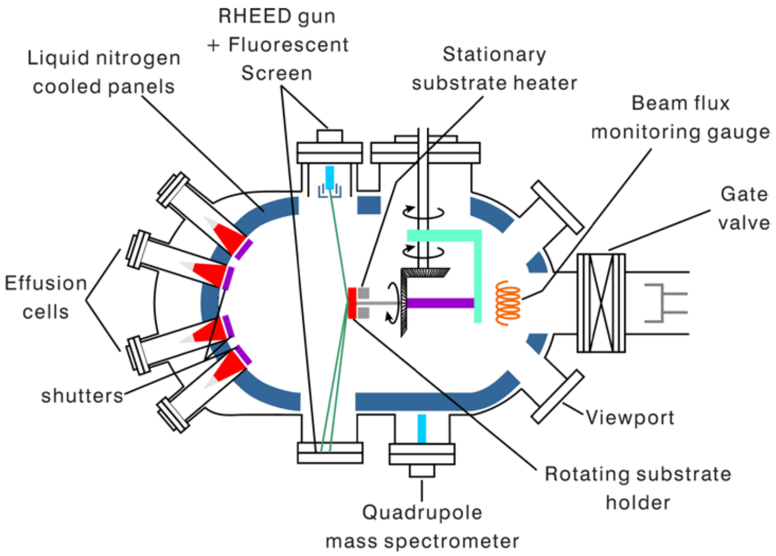

Figure 1.3.1: A top-down view of a typical MBE growth chamber containing four effusion cells, a RHEED and mass spectrometer for *in situ* sample monitoring, and a rotating stage to avoid non-uniform beam fluxes. Figure taken from the web page of the MBE Laboratory in the Institute of Physics of the ASCR, Czech Republic.

the angled directions of the incoming atoms. Samples are monitored within the growth chamber through the use of a reflection high-energy electron diffraction (RHEED) system and mass spectrometer providing real time information about the growth rate and composition. This allows the observer to immediately see the effects of beam intensity and substrate temperature on the film growth.

The RHEED system consists of an electron gun and a phosphor-coated screen. Electrons are emitted from the gun at a very small glancing angle to the substrate, these are then reflected and diffracted from the surface to form a distinct pattern on the screen related to the surface ordering and material structure. When the substrate is atomically flat electrons are only weakly scattered from the surface resulting in a pattern of well-defined intense dots. As material is deposited onto the substrate epitaxial islands are formed resulting in an increase in scattering and a drop in the intensity of the RHEED pattern dots forming long streaks normal to the substrate surface. These islands then gradually coalesce to form a new flat surface with unfilled areas of the previous layer. Electron scattering therefore begins to drop again until finally the voids

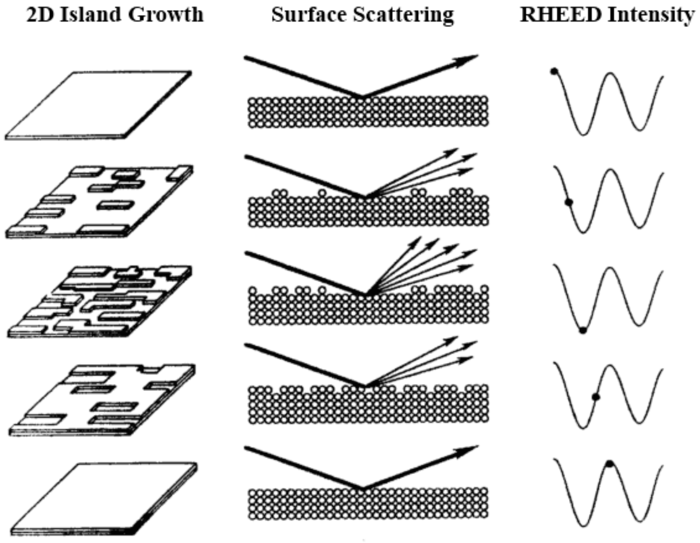

Figure 1.3.2: A diagram showing the gradual progression of the RHEED intensity as a single layer of material is deposited onto the substrate. The first column shows the development of islands on the surface, and the second how the incoming electrons are scattered from this surface. The final column then shows the resulting oscillations of the RHEED intensity.

are filled leading to a peak in reflectivity. This process then repeats with the resulting oscillations in the RHEED diffraction pattern intensity related to the rate of growth. Figure 1.3.2 shows a simplified diagram of this process with idealised RHEED oscillations.

As well as the growth chamber shown in figure 1.3.1 modern MBE systems also include separate substrate introduction, and analysis chambers. Introduction chambers act as load-locks to mount substrates into the system without the necessity to evacuate the growth chamber. These much smaller volume chambers also mean that heating can be performed in order to outgas both the substrate and holder before being moved into the main chamber. Analysis chambers are used for further substrate preparation and allow the use of surface characterisation techniques such as AES and XPS not possible within the main chamber UHV environment.

Standard (Ga,Mn)As films are grown on semi-insulating GaAs wafers using temperatures between 150°C and 200°C. Optimum growth conditions occur at the 2D-3D RHEED phase boundary (Campion *et al.* (2003)) with higher

Mn doping levels requiring lower temperatures. Such low temperatures inhibit surface diffusivity and result in less surface Mn, but also make the measurement and control of temperature more difficult than a standard GaAs growth. Substrate temperatures are traditionally measured within MBE systems using either a thermocouple or an optical pyrometer. However, both these techniques are limited at (Ga,Mn)As growth temperatures with thermocouples being much more sensitive to the heater than the substrate and optical pyrometers typically inaccurate below 500°C. Temperature monitoring for (Ga,Mn)As growth in Nottingham is therefore performed by measuring the GaAs substrate band edge absorption using a k-Space BandiT solid state spectrometer system. Growth is performed using two gallium cells for near exact stoichiometry and the Mn density determined from the Mn/Ga flux ratio calibrated by secondary ion mass spectroscopy.

1.4 Nanofabrication

After the MBE growth process most (Ga,Mn)As samples need to be fabricated into structures in preparation for measurements. For typical structures such as a Hall bar this procedure can frequently be completed within a couple of days or even a matter of hours. However, for smaller nanoscale structures such as the Aharonov-Bohm rings studied in chapter 4, fabrication can form a large, and integral part of the work. Given the significant amount of time devoted, and its application to almost all areas of (Ga,Mn)As study, this section extensively details the subject of nanofabrication acting as a preface to the fabrication work on nanorings detailed in chapter 4.

When fabricating nanostructures the first fundamental obstacle to overcome is always how to define areas of the required size. In the case of Aharonov-Bohm rings the diameter requirement is related to the sample phase coherence length as detailed in chapter 4. For (Ga,Mn)As this is expected to be close to 150 nm, the nanorings therefore have to have a comparable diameter. Fortunately one of the main aims within the electronics industry has always been the miniaturisation of circuit components in an effort to improve device performance. The driving technology behind the fabrication of such increasingly complex and compact electronics is lithography of which there are two predominant variants:

photolithography and electron beam lithography (EBL).

Fabrication within industry has always been dominated by increasingly complex forms of high resolution photolithography because of the high cost and slow device output of EBL. Unfortunately, due to the source wavelength, photolithography as offered by standard mask aligners in research only provide resolutions of around two microns. The prime focus of this section for the nanorings is therefore the higher resolution EBL; however, it must be noted that a lot of the basic principles and steps remain the same for both techniques.

1.4.1 Principles

Whether using photolithography or EBL the sole objective of lithography is always to transfer a pattern or design onto the surface of a sample. This is always done by creating a temporary mask over the sample in which the design has been defined using a chemical known as a resist. Areas on the sample can then be selectively removed via etching. During this process the resist, as implied by the name, is either unaffected or removed at a reduced-rate to that of the sample. The remaining resist can then be removed leaving an imprint of the design in the surface. As well as removing from the surface of samples it is also possible to selectively deposit materials by choosing appropriate resists, set-ups and pattern designs. Within electronic structure fabrication the whole purpose of this is to create electrically isolated shapes and contacts on substrates; full devices are fabricated via the use of multiple lithography-based processing stages.

The design within the resist is produced by exposing it to some form of radiation to which it is sensitive. In photolithography this is high frequency ultraviolet radiation, and in EBL it is electrons from a focused thermionic or field emission source. Once exposed to the given radiation the resist becomes either more or less soluble to a developing solution. Thus when soaked in the appropriate developer for the correct period of time some areas are removed and others retained.

Figure 1.4.1 shows a simple flow diagram of a typical structure fabrication procedure. Fabrication for a standard Hall bar for example would consist of

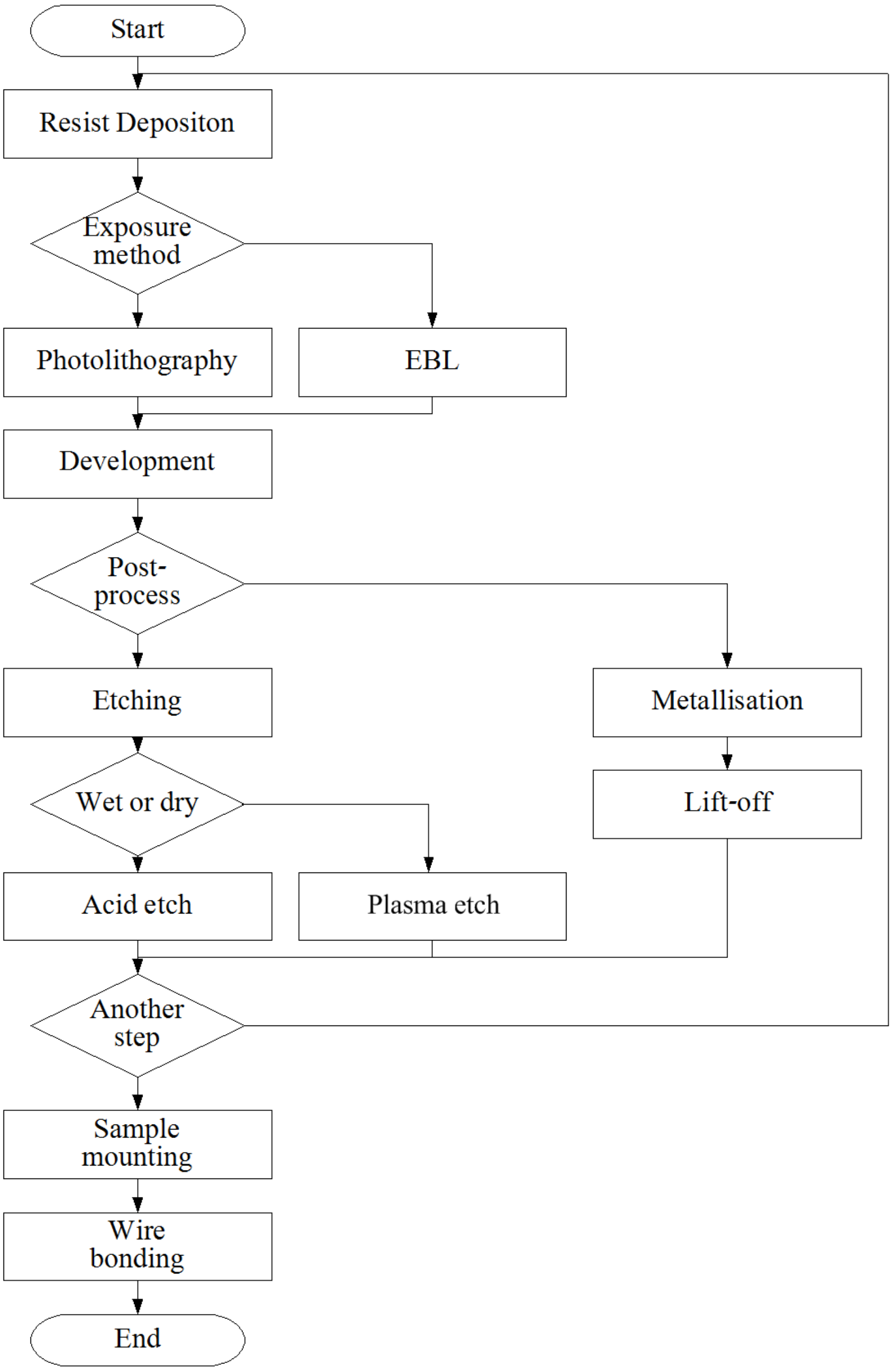

Figure 1.4.1: A flowchart showing the basic steps taken when fabricating structures using lithography. This diagram also acts as a visual summary of the information covered in this chapter.

a first photolithography exposure followed by wet etching, and then a second exposure followed by gold evaporation. However, it is entirely possible to carry out steps in various orders and multiple times depending on the final structure requirements.

1.4.2 Electron Beam Lithography

Systems

Electron beam lithography systems can vary between being a converted scanning electron microscope (SEM) with pattern generator to a professionally manufactured beamwriter by such companies as Leica, Etec or Raith. In all cases, however, the basic components remain the same: a high voltage power supplied electron gun, an electron beam column, a moveable stage within a vacuum chamber and a pattern generator. Figure 1.4.2 shows a diagram of the basic components of a standard EBL system taken from the SPIE Handbook of Microlithography, Micromachining and Microfabrication (Rai-Choudhury (1997)).

As can be seen from this diagram the electrons are emitted from the gun and passed through a set of electrostatic and electromagnetic lenses within the beam column. These act to focus the beam and correct for any astigmatism; in this case electron optics follows along similar principles to that of light optics. Due to the fact that the electron source is generally never turned off a beam blanker is used to divert the beam when the sample is not to be exposed or no imaging is carried out. As with a number of the lenses the blanker simply makes use of an applied electrostatic field which allows fast response switching.

With the beam blanker off the electrons then pass through a deflection system that allows the beam to be quickly scanned across the sample through an objective lens. Again this system works along the same principle as both the lenses and the blanker, and deflects the beam over a square on the sample called the writefield. Larger patterns can be written in blocks in which one whole writefield is completed before the stage is moved, and the exposure process repeated. This avoids the high deflection of electrons that can cause focus issues, but can also lead to misalignments between adjacent fields. System calibration

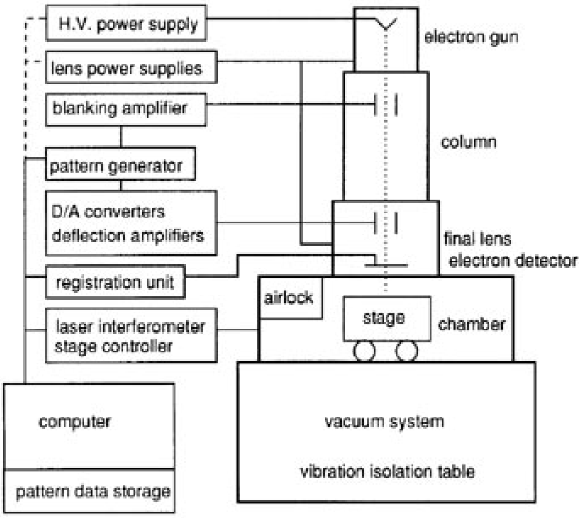

Figure 1.4.2: A block diagram showing the main components of a standard EBL system.

and a high resolution substage are therefore required to avoid poor writefield stitching. Typically higher specification systems have a laser interferometer controlled stage allowing accurate movements to within less than 5 nm. More information regarding the operation of electron columns including potential electron sources, various lens types, stigmators and apertures can be found in Rai-Choudhury (1997).

Whilst the basic component parts within most systems remains the same there are still various strategies for pattern writing each of which offers distinct advantages and disadvantages. The most common method is to use a round (Gaussian) beam to either vector or raster scan the pattern, but more complicated shaped-beam structures can also be employed for quicker writing. Raster scanning involves moving the stage and scanning over the whole writefield line by line blanking the beam where exposure is not required. This produces very reproducible results, but means that sparse pattern designs take just as long as much denser ones. Vector scanning, however, involves only scanning over the required areas following a meander or line path using the blanker to move between exposure areas. This leads to faster sparse pattern writing because unwritten areas are skipped, but it does mean settling and hysteresis must first be calibrated.

The system used in Nottingham for nanoring fabrication is a converted Jeol

JSM-7000f SEM with an in-lens Schottky field emission source capable of acceleration voltages between 0.5 kV and 30 kV, and probe currents as high as 200 nA. This offers a resolution of up to 3 nm, maximum magnification of ×500,000 and detectors for secondary, backscattered (Composition, Topography) and forward scattered electron imaging. This is combined for EBL with a XENOS XPG 2 pattern generator with a maximum writing clock speed of 20 MHz, and a Deben PCD beam blanker. Exposures are carried out using a Kleindiek substage with a 10 mm travel and resolution of 0.5 nm with a maximum 1 nm/min drift. However, imaging can also be performed with a variety of holders including an angled platform for surface profiling.

Resists

With the EBL system chosen the next step is the choice of resist; this is always very important and depends very much on the intended outcome. The choice of resist and its dilution determines the resolution, the contrast, the etch resistance and the thickness. These ultimately lead to the minimum structure size attainable, the edge profile after exposure, the sensitivity to proximity effects and the quality of lift-off. Standard resists are generally polymers dissolved in a liquid solvent with a larger proportion of solvent leading to a thinner film after deposition.

The exposure of resist always results in a change in solubility to the appropriate developer. The reaction caused separates resists into two main categories: positive and negative. Positive resists become more soluble after exposure generally caused by the breaking down of molecules to leave behind lower weighted fragments. Negative resists on the other hand become less soluble due to the cross-linking of polymer chains to form larger molecules. The positive tone resists are usually better suited to contact pattern writing whilst negative are suitable for mask patterns or gates.

Poly(methyl methacrylate)

The most widely used resist in EBL for the fabrication of nanostructures is poly(methyl methacrylate) (PMMA), and it is this that was used to fabricate the (Ga,Mn)As nanorings. It is primarily the most popular electron beam resist because of its extremely high resolution, versatility, ease of handling and simplicity. It does, however, have a very poor dry etch resistance; etch rates are close to that of (Ga,Mn)As therefore posing a problem when fabricating the nanoscale rings.

PMMA is a positive tone resist consisting of a synthetic polymer composed of carbon (C), oxygen (O) and hydrogen (H) dissolved in either chlorobenzene or the much safer anisole. The base molecule of PMMA is $C_5O_2H_8$ which is repeated many thousand times over to produce the 495k and 950k polymer resist variants. Once exposed to an electron beam a scission of the polymer chains is caused as shown in figure 1.4.3.

The top of this diagram shows a portion of a PMMA polymer in which carbon is represented by grey circles, oxygen blue and hydrogen red. When this is exposed to an electron beam, as shown by the e^- arrows, the bond between carbon atoms is broken. This promotes the formation of covalent bonds and leads to the much smaller molecules shown at the bottom of the diagram. Such break down occurs along the whole polymer resulting in many thousands of fragments that can be removed by the developer.

PMMA comes in various molecular weights and concentrations each of which is suitable for different lithographic steps. The two most commercially available weights are 495k and 950k. The higher molecular weight version has a better resolution and is thus more appropriate for nanoscale fabrication, but the lower weight does have a higher sensitivity and can be used in the fabrication of the nanoring contacts. On top of this a number of different concentrations are available as denoted by their C- or A-rating. The C or A indicates the dilution solvent and the number indicates the percentage of PMMA, thus an A5 495k resist consists of 5% 495k molecule PMMA and 95% anisole.

The thickness of the resist after sample deposition is dependent on both the solvent concentration and molecular weight. The thickness required depends on the post-exposure process, and also has an effect on the required dose. Typical doses for 950k PMMA are $100\,\mu\mathrm{Ccm}^{-2}$ at 10 kV, $200\,\mu\mathrm{Ccm}^{-2}$ at 20 kV and $300\,\mu\mathrm{Ccm}^{-2}$ at 30 kV.

The conventional developer for PMMA is a solution of methyl isobutyl ketone

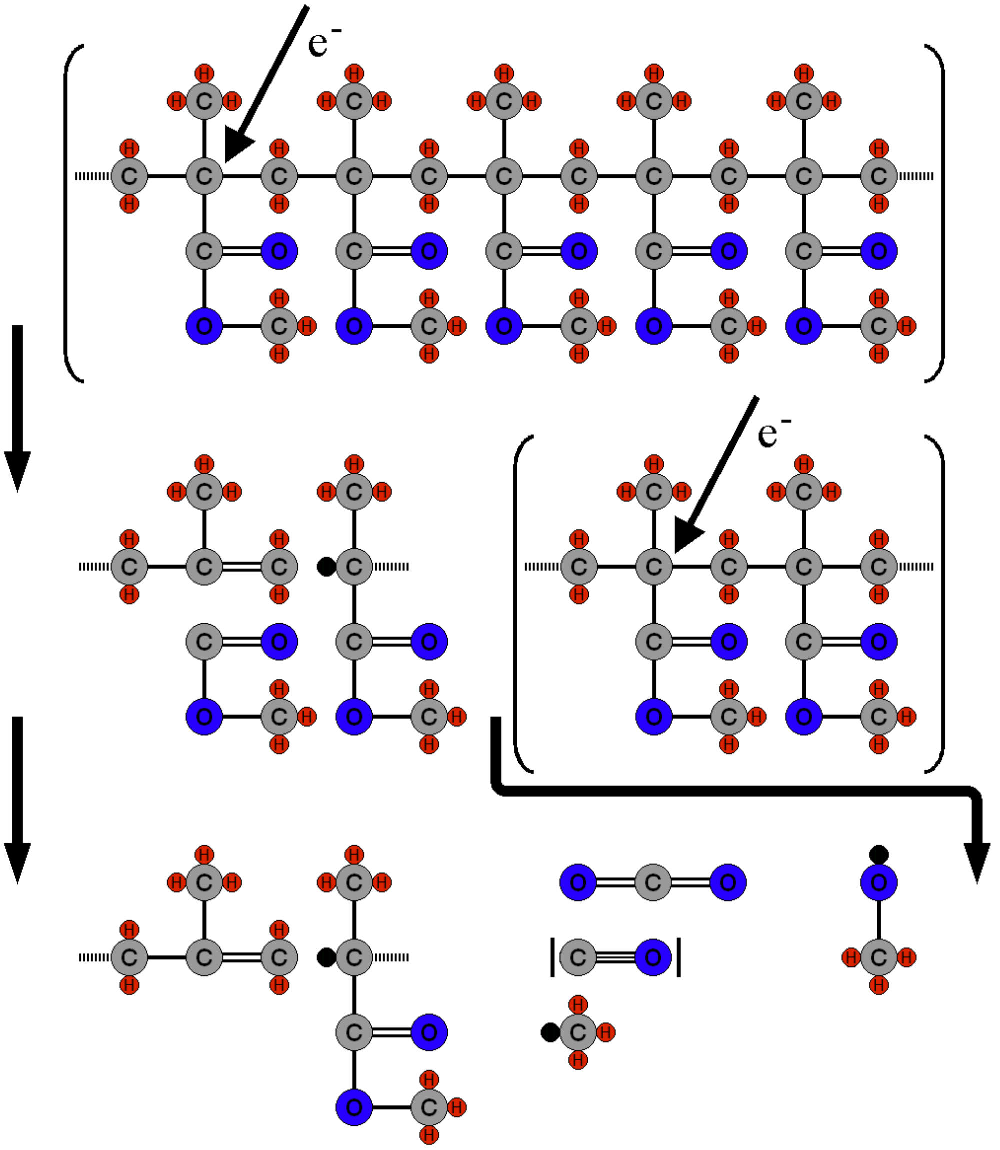

Figure 1.4.3: A diagram of the EBL exposure of PMMA with a splitting of the original $C_5O_2H_8$ base shown at the top down to the smaller fragments at the bottom.

(MIBK) and isopropyl alcohol (IPA). For larger features samples are usually developed in a 1:1 mixture for between one and two minutes. However, smaller features require a higher ratio of IPA; a composition of 1:3 leads to a very high resolution, but lower sensitivity. An alternative developer, and that used during nanoring fabrication testing, is IPA (7):(3) DIW as first employed by Cambridge (Yasin *et al.* (2002)). This can offer improvements in contrast, sensitivity, exposure dose latitude and roughness. The development time depends very much on the resist concentration, thickness and feature size; typically a time of 10 to 15 seconds is used.

Although usually used as a positive resist PMMA can also act as a negative resist via the use of very high exposure doses. By applying a dose of more than ten times the typical amount the polymer molecules crosslink forming a carbon-like structure that can only be removed via oxygen (O_2) plasma (Zailer *et al.* (1996)). This effectively creates a high-resolution negative resist that with optimisation can be used for nanostructure fabrication.

Dose

When exposing any resist the most important parameter that must be considered is the dose. Within photolithography this is simply related to the exposure time and system used. For the most frequently used resists this is usually between five and ten seconds. In EBL, however, it is a little more complicated because of the write-like method of exposure.

In order to clear an area of resist a certain number of electrons must hit the sample within that region; the number of electrons is proportional to the beam current and the dwell time. Thus simple equations can be derived relating the dwell time to the area D_{area}, line D_{line} and dot D_{dot} doses (1.4.1).

$$D_{\text{area}} = \frac{I_{\text{beam}}.T_{\text{dwell}}}{s^2} \qquad \mu\text{Ccm}^{-2} \qquad (1.4.1a)$$

$$D_{\text{line}} = \frac{I_{\text{beam}}.T_{\text{dwell}}}{s} \qquad \text{pCcm}^{-1} \qquad (1.4.1b)$$

$$D_{\text{dot}} = I_{\text{beam}}.T_{\text{dwell}} \qquad \text{pC} \qquad (1.4.1c)$$

The beam current I_{beam} is defined by the filament, aperture and excitation voltage of the beam column used; most of which can be set by the user. The dose is defined by the process to be carried out and depends very much on the resist, developer, temperature and excitation voltage. And finally, both the dwell time T_{dwell} and the step size s are exposure parameters that depend on the required accuracy, pattern design, and throughput.

Proximity Effects

Unfortunately, no matter which resist or method is chosen EBL is always limited by electron scattering within the resist that can lead to unwanted proximity effects in the desired pattern. As electrons enter the resist a lot of their initial energy is lost in the form of lower energy secondary electrons resulting in two main types of scattering event. The first form is small angle forward scattering as the electrons penetrate the resist causing the exposure profile deeper within the resist to be wider than that of the beam diameter. This effect can easily be reduced through the use of thinner resists and higher acceleration voltages. However, as electrons pass further into the resist many undergo much larger angle backscattering. It is this second form of scattering along with a small contribution from high energy secondary electrons that results in exposure away from the beam and hence the proximity effect.

There are a number of methods used to try and avoid or minimise this effect, again each offering their own advantages and disadvantages. The standard technique is dose correction that involves giving every shape within the pattern a specific dose such that smaller more isolated areas become more exposed. A lot of the professional beamwriters, such as that by Raith, include proprietary software that can be applied to pattern designs before exposure. These generally model the electron distribution as a double Gaussian, sometimes with an exponential decay, in the form of Monte Carlo simulations. It must be noted, however, that before such simulations can be made a number of mathematical parameters need to be measured through the use of various specifically designed test exposures. Unfortunately, not all systems offer dose correction programs making large pattern designs extremely time consuming using even a very basic form of this technique. Another method that can sometimes be employed is pattern biasing in which individual shapes and elements are resized whilst retaining the same dose.

Dose correction and pattern biasing offer a simple, but effective, approach to proximity correction; however, both require long calculation times prior to each exposure. A slightly more time efficient approach is that of background dose equalisation in which a GHOST consisting of the reverse pattern is first exposed using a defocused beam (Owen and Rissman (1983)). This mimics the shape of the backscatter distribution resulting in a roughly uniform background dose after the main exposure, and thus avoids the need for additional computation. Depending on the pattern design, however, sample throughput can still remain low because of the need for a second exposure and can also lead to a loss of both contrast and resolution.

Finally, multiple layer resists can be used during the processing stages as a form of compensation by reducing the effect in the top layer via the absorption of backscattered electrons in the lower layer. This does mean that the processing time and cost is increased, but can also offer the advantage of a clean lift-off after metal deposition.

1.4.3 Pre-exposure processing

Before even applying a chosen resist to the sample the very first thing that must be done, and is repeated multiple times throughout the fabrication process, is sample cleaning. Whilst this may seem a trivial process, and can easily be overlooked, without it difficulties can immediately arise in the form of surface chemical residues and unwanted particles. If present either can result in an uneven resist layer on the sample that can significantly affect the quality of the upcoming exposure and processing.

The general method of sample cleaning is to soak the chips in various solvents and then blow dry using a nitrogen (N_2) gun. The primary solvent used is acetone which is then cleaned off using IPA. In certain circumstances, such as at the very beginning of fabrication and after wafer cleavage, ethyl lactate and methanol may also be employed along with an ultrasonic bath. When using some resists it is also sometimes necessary to bake the sample after cleaning to completely dry it and remove any solvent residue left on the surface.

Once the sample has been cleaned resist is applied in single drops onto the surface using some form of small disposable pipette. This is then spun at high speed to cover the surface with a thin uniform layer; an even distribution across the whole sample is crucial for high quality lithography. Once spun with the resist the sample should have a level film across the surface except close to the edges and corners. It is for this reason that all structures must be fabricated close to the centre of the chip when using lithography in order to avoid exposure on uneven resist.

For EBL this thicker corner resist poses no problem; however, for contact photolithography it can affect how close the exposure resist can be moved to the glass mask. This can result in the projection of UV light being out of focus and the exposure edges being poorly defined. This can be overcome by removing the thicker resist, either by a relatively long window exposure (20 s), or by simply brushing it off carefully without touching the required surface at the centre.

The speed and time for which a sample is spun depends very much on the resist used, the thickness required and the chip size. For a standard 5 mm x 5 mm chip, a typical speed at which the resist is spun on is 5000 rpm for between 30 seconds and 1 minute. The resulting resist thickness is then dependent on the concentration and, for PMMA at least, the molecular weight. Resists containing more solvent are spread more thinly; an A8 dilution of PMMA would have a much greater thickness than the equivalent A1. Similarly lower weight variants would have a lower thickness than higher ones.

The overall thickness of the resist is a very important consideration, and the requirement is decided by the processing to be carried out after exposure. When etching the whole purpose of the resist is to withstand the etchant, the most obvious choice is therefore to make it as thick as possible especially when creating deep trench-like structures. Unfortunately using a thick resist can severely limit the resolution meaning that for smaller features a thinner resist is much more preferable. The thickness must be balanced with the etch resistance and the etch depth needed. For metallisation the thickness is determined by the depth of metal to be deposited. For a successful lift-off the resist should be at least one and a half times as thick as the required metal layer.

After the sample has been spun with resist it must be heated in order to evaporate the dilution solvent and harden the surface. Temperatures, times and even methods vary, with photoresists often only requiring a couple of minutes on a hotplate, but many EBL resists need a full oven bake. PMMA is usually cured in an oven at a constant temperature of between 100°C and 200°C for one hour.

1.4.4 Post-exposure processing

Wet and Dry Etching

After exposure and development the next stage is to transfer the pattern design onto the sample; there are two standard processes by which this can be done. Etching is the first of these and offers two distinct methods: wet and dry. Wet etching involves immersing samples in a solution containing acids, and dry etching employs the bombardment of ions or the use of plasma. Each offers slightly different benefits as summarised in table 1.1.

	Wet	**Dry**
Advantages	• Low cost and easy to carry out • High etch rate • High selectivity	• High resolution
Disadvantages	• Low resolution • Potential chemical hazards • Potential wafer contamination	• High cost • Poor selectivity • Potential radiation damage

Table 1.1: The advantages and disadvantages of wet and dry etching.

A typical wet etch for GaAs, which can also be used for (Ga,Mn)As, is a solution containing sulphuric acid (H_2SO_4), hydrogen peroxide (H_2O_2) and water (H_2O). These can be mixed with different ratios of various concentrations to control the etch rate with a higher quantity of acid leading to higher etch rates. A standard mixture of 1:5:5 for 80 s is used in Nottingham when fabricating (Ga,Mn)As Hall bars resulting in an etch depth of roughly 2.2 μm.

Unfortunately, due to its isotropic nature wet etching is not usually suitable for nanostructure fabrication. Dry etching was originally developed to resolve this flaw. There are three main techniques: sputtering, plasma etching and reactive-ion etching (RIE). Each of these is significantly more directional than wet etching with vertical etch rates that are far greater than the lateral etch rates. Of the three of these it is RIE that is used when fabricating the (Ga,Mn)As nanorings.

RIE effectively acts as an intermediate between sputtering and plasma etching with both beam energy and chamber pressure generally somewhere between the two. It makes use of both ion bombardment (sputtering) and chemical reactions. A standard RIE set-up consists of a low pressure vacuum chamber within which two electrodes are used to create an electric field to accelerate ions towards the sample. A gas is pumped through the chamber and a strong oscillating RF field applied which ionises the molecules to form a plasma that generates both ions and free radicals. When ions strike the sample they remove material via the transfer of kinetic energy, whilst free radicals react chemically with the exposed surface atoms forming volatile products. Both processes act to etch the sample and it is this strongly vertical approach that leads to such anisotropic properties when using RIE.

A high quality and reproducible etch relies on conditions in the system being held constant; the pressure, gas flow rates and radio frequency (RF) power must all be closely monitored. Typically a system needs a few seconds to settle before controllable and constant etching can be carried out. The choice of gases used within the chamber depends on the material to be etched with different gas combinations promoting different ion species. The RIE of GaAs is frequently carried out using $SiCl_4$-based plasmas.

Metallisation

The second process that may be performed after development is metallisation: selectively coating the sample with metal. Whilst etching is usually used for defining the actual structures within the chip, metallisation is used to create contacts to the device, or alignment marks. Contact pads can be bonded to in order to make electrical measurements, and alignment marks used to position further processing steps. The most widely used metal for both is gold.

Metallic layers are deposited onto samples via controlled evaporation in purpose built systems. These consist of a large bell jar containing a windowed sample holder with shutter, metal coils and a piezoelectric crystal. Pieces of high purity metal are heated by passing a high current through the coils resulting in an angular distribution of emitted atoms that uniformly cover all surfaces in line-of-sight. Deposition onto the sample is controlled by the shutter whilst the crystal is used to measure the rate.

The general procedure after fitting the sample is to pump the system down to around 10^{-6} to 10^{-7} Torr, and then with the shutter still closed to begin heating the metal. The deposition rate is then adjusted via the applied current, and the pressure left to stabilise before uncovering the sample. This stabilisation is required in order to release any trapped gases or unwanted surface impurities from the metal before deposition. In most cases before the evaporation of the main metallic layer a thin wetting layer is needed to improve adhesion to the sample surface. Standard adhesion layers for gold are chromium or titanium with a thickness of around 20 nm.

The next step after evaporation is to remove the resist and with it the unwanted metal; a process that is usually made much easier by well-defined edges in the resist from an accurate exposure and development. Lift-off is performed simply by immersing the sample in a solvent such as acetone. In most cases the resist-metal will easily separate from the surface after a short period of soaking, but sometimes it can also be necessary to agitate it either by spraying further solvent across or, in the worst case scenarios, by using a short burst of ultrasound in a sonicator. However, this is generally considered to be a last resort because it can easily result in damage to the metal layer if used for too long.

1.5 Post-growth Annealing

The strong magnetic behaviour of a ferromagnetic material is derived from the quantum-mechanical exchange interaction between unpaired electron spins. This acts to align spins resulting in a net magnetic moment even in the absence of an external magnetic field. However, rather than being composed of a single region of parallel moments these materials consist of a number of domains each spontaneously magnetised to saturation. The alignment within these magnetic domains varies from one to another with the directions based on the minimisation of internal energy. This can result in largely random directions and a total magnetisation close zero, however, certain directions can be preferred based on the crystal structure, stress or shape. Ferromagnets usually have easy-axes which are energetically favourable crystallographic directions for the spontaneous magnetisation resulting from magnetocrystalline anisotropy. Further information about magnetic anisotropy within (Ga,Mn)As can be found in section 1.7.2.

The application of a small external magnetic field to this structure causes domains to line up with one another until the magnetisation becomes saturated when all domains are aligned in the direction of the external field. Ferromagnets then tend to stay magnetised once the field is removed with the fraction of the saturation magnetisation retained called the remanence. All ferromagnetic materials have a maximum temperature at which this alignment of spins and domain structure is destroyed resulting in zero spontaneous magnetisation. The Curie temperature T_c is the point where the thermal energy becomes great enough to overcome the effects of the exchange interaction. Above this temperature the material loses its ferromagnetism and becomes paramagnetic with random spin orientations.

The first ferromagnetic (Ga,Mn)As samples, grown in the mid-nineties, displayed relatively low Curie temperatures around 60 K (Ohno *et al.* (1996)) due in part to their low Mn doping levels. Sample growths performed over the subsequent couple of years therefore focused on increasing this value both through the use of post-growth annealing and by improving the MBE growth process. These early low concentration samples showed behaviour consistent with the Zener model (1.2.1), however, in 1998 a plateau was reached at 110 K (Matsukura *et al.* (1998)) with higher concentrations resulting in values lower than that predicted and samples demonstrating significant magnetisation deficits. Very little progress was made for almost five years with increased annealing temperatures and times leading to very similar results or even drops in T_c from as-grown (Potashnik *et al.* (2001); Yu *et al.* (2002)). This value was even proposed as a fundamental upper limit (Yu *et al.* (2002)) related to the self-compensation covered in section 1.2.

Work on improving sample Curie temperatures from this apparent limit therefore concentrated on the reduction or removal of the unwanted interstitial manganese and arsenic antisite defects. Unfortunately, self-compensation is an important property connected to the lattice stability with the formation of interstitial manganese crucial to (Ga,Mn)As growth beyond the equilibrium solubility limit. Avoiding the formation of $\mathrm{Mn_{int}}$ defects is therefore impossible during the MBE growth process itself. The solution to this problem was found in 2002 by annealing samples following a similar approach to that used previously, but at much lower temperatures for longer periods of time (Edmonds *et al.* (2002); Ku *et al.* (2003); Wang *et al.* (2005a)). Careful control of both the growth and annealing conditions allowed samples to be produced with Curie temperatures as high as 173 K, well in excess of the original record.

This pronounced increase in T_c arises from the metastable nature of the unwanted $\mathrm{Mn_{int}}$ defects. The low activation energies of these atoms allows them to be removed by annealing samples at temperatures below 200 K. Prior to this work samples had always been annealed around 250 K at temperatures potentially high enough to not only remove the interstitial manganese, but also the higher activation energy substitutional manganese. The resulting reduction in $\mathrm{Mn_{Ga}}$ could explain the observed drops in T_c in some of the earlier work when annealing for longer periods of time.

These initial studies showed that sample Curie temperatures are very sensitive to both the annealing temperature and time with optimum conditions dependant on sample thickness. Samples consisting of thinner (Ga,Mn)As layers were found to be annealed quicker than their thicker counterparts with *in situ* monitoring showing more rapid resistivity drops with reduced film thicknesses. From this behaviour it was deduced that the most dominant mechanism in the removal of interstitial defects is a diffusion to the surface leading to $\mathrm{Mn_{int}}$ passivation via oxidation. Models of the diffusion of interstitial manganese to the free surface gave an excellent agreement with the resistivity data assuming the increases in carrier concentration are entirely caused by the removal of compensating $\mathrm{Mn_{int}}$ defects (Edmonds *et al.* (2004)). The expected surface accumulation of manganese from this behaviour was confirmed by auger electron spectroscopy (AES) on samples both before and after annealing.

It is this resulting rise in carrier concentration that leads to an increase in

T_c as predicted by the mean-field Zener model (1.2.1). Hole densities within 6% manganese samples typically increase by a factor of two whilst changes in mobility remain below 10% (Edmonds *et al.* (2004)). Low-temperature annealing also results in an increase in saturation moment, and changes in the forms of both the magnetisation $M(T)$ and the resistivity $\rho(T)$. However, not all of the effects of these defects are reversible with lattice constants still remaining higher than that expected without interstitials due in part to the survival of some Mn_{int} atoms even after an optimised annealing process.

Whilst the effects of interstitial manganese can be greatly reduced via sample annealing, arsenic antisite defects are not as easily removed. This is due to their stability up to 450°C well above the temperature at which manganese precipitation starts to dominate the properties of (Ga,Mn)As. However, antisites can be minimised by growing samples using As_2 dimers rather than As_4 tetramers (Campion *et al.* (2003)).

1.6 Measuring Sample Curie Temperatures

1.6.1 Remanent Magnetisation

The standard method used to obtain the Curie temperature of ferromagnetic materials is through the use of a SQUID system by measuring the remanent magnetisation as a function of temperature. This involves field-cooling the sample in order to saturate the magnetisation in the direction of the field before warming up and measuring the remanence. The measured remanence is equal to the spontaneous magnetisation because of the strong uniaxial anisotropy and single domain structure of high T_c (Ga,Mn)As samples. Typical applied fields used when measuring the T_c of (Ga,Mn)As samples are between 500 Oe and 1000 Oe. This has to be high enough to saturate the magnetisation, but low enough to avoid unwanted fields caused by trapped flux within the superconducting magnet. Figure 1.6.1 shows remanent magnetisation plots of a 12%, 25 nm (Ga,Mn)As sample taken from wafer Mn437 both as-grown and annealed. These datasets demonstrate the significant rise in T_c after annealing as well as a move to more uniaxial behaviour along the $[1\bar{1}0]$ direction.

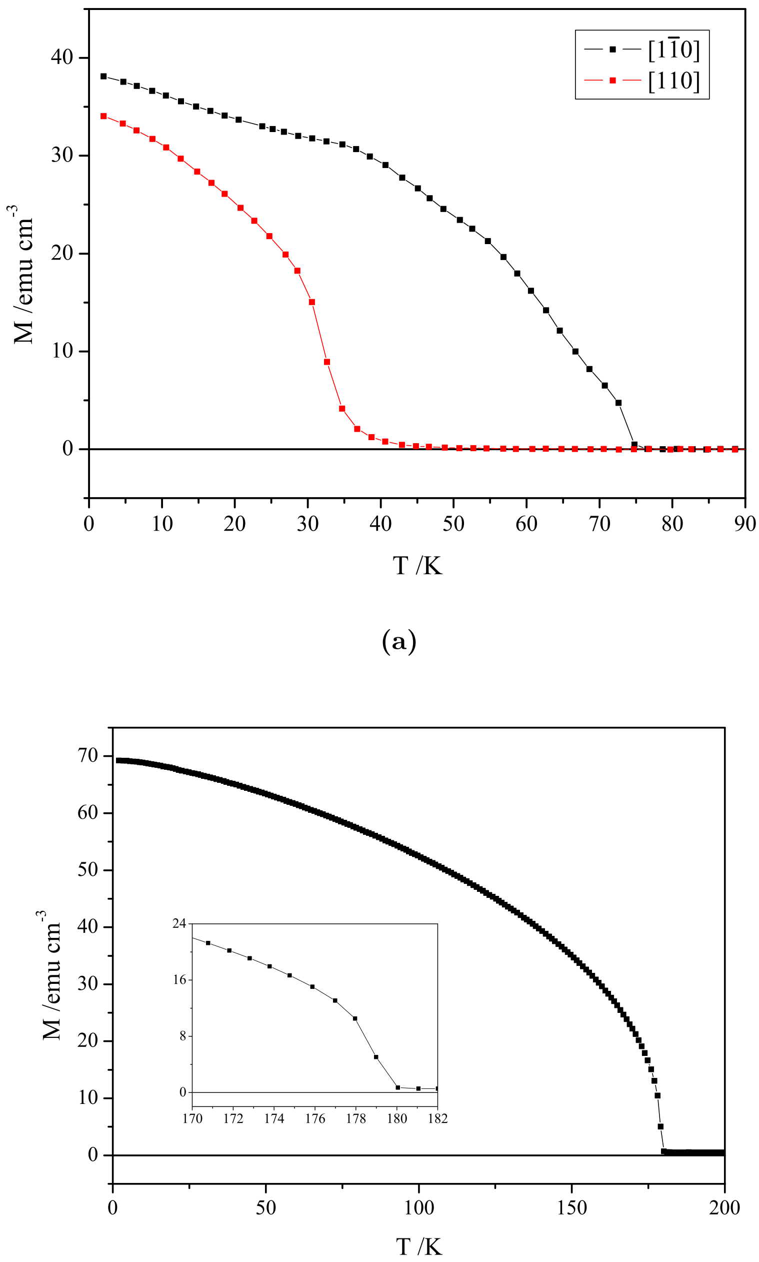

(a)

(b)

Figure 1.6.1: Typical remanent magnetisation curves for a high T_c (Ga,Mn)As sample both as-grown (a) and fully annealed (b) after a field-cool at 1000 Oe. The inset in (b) shows the annealed data close to T_c and demonstrates how even for high quality samples a small non-zero magnetisation can be present above T_c.

The magnetisation of a ferromagnetic material is expected to drop sharply to zero at the Curie temperature. However, as can be seen from the inset in figure 1.6.1b this is not usually the case within (Ga,Mn)As samples. A small tail is frequently observed which can potentially result in poorly defined measured Curie temperatures. This behaviour is caused by sample inhomogeneity effectively resulting in a non-uniform Curie temperature across the sample, and the presence of small unwanted external magnetic fields.

This inhomogeneity arises from the high-sensitivity of the material to its growth temperature. During MBE growth the temperature is controlled by a centrally mounted heater resulting in a temperature gradient from the centre of the wafer to the outside edge. For a typical two inch wafer this drop in temperature is roughly 2 K which can lead to radial T_c variations of as much as 3 K. A more in-depth overview of this T_c broadening can be found in the critical phenomena chapter in section 2.5.5. The small external magnetic fields are also very difficult to remove within a SQUID due to the use of a superconducting magnet. Whilst the applied fields during cooling are kept below 1000 Oe to minimise this effect small magnetic fields are still always present, and can be enough to alter the behaviour upon approaching T_c.

1.6.2 Arrott Plots

These problems with remanent magnetisation measurements of (Ga,Mn)As are further exacerbated when measuring as-grown samples with additional difficulties associated when samples are biaxial. An alternative technique frequently used to calculate sample Curie temperatures is through the use of Arrott plots (Arrott (1957)). In his original paper Arrott made use of a power series expansion of the magnetic field H derived from the mean-field Brillouin function.

$$M = N\mu \tanh\left(\frac{\mu H + \mu\lambda M}{k_\mathrm{B}T}\right) \tag{1.6.1}$$

By rewriting this function and expressing the inverse hyperbolic tangent as a Taylor series a relation can be found between H and M. Equation (1.6.2) shows this expansion having substituted in for the susceptibility $\chi = \frac{H}{M}$ at zero field, and $a = \frac{k_\mathrm{B}T}{\mu}$.

$$H = \frac{1}{\chi}M + \frac{a}{3}\left(\frac{M}{N\mu}\right)^3 + \frac{a}{5}\left(\frac{M}{N\mu}\right)^5 + \cdots \tag{1.6.2}$$

By ignoring the higher order terms in this expansion it can be seen that a plot of M^2 against $\frac{H}{M}$ for a given temperature close to T_c should be linear. At $T = T_\mathrm{c}$ the susceptibility is theoretically infinite, and therefore the associated Arrott plot should pass through the graph origin. The Curie temperature can therefore be calculated by making a series of magnetisation against field measurements at temperatures around that expected, plotting their respective Arrott isotherms, and then making linear fits to each to find the intercept values.

The use of Arrott plots can potentially avoid the uncertainty faced when performing standard magnetisation measurements. However, this techniques does require a much greater amount of time to complete, and relies on a number of assumptions and simplifications, most notably the use of the mean-field approximation. Another advantage of this method is that it can also be performed via magnetotransport measurements due to the presence of the anomalous Hall effect within ferromagnetic materials. This allows a relatively accurate calculation of the sample Curie temperature without the need for a SQUID system.

The transverse resistivity ρ_xy of a ferromagnet such as (Ga,Mn)As can be described as the sum of both the ordinary and anomalous Hall components. The first term representing the effects of the Lorentz force on charge carriers, and the second the Hall effect contribution due to the spontaneous magnetisation.

$$\rho_\mathrm{xy} = R_0 H_\mathrm{z} + R_\mathrm{A} M_\mathrm{z} \tag{1.6.3}$$

The ordinary Hall coefficient R_0 depends mainly on the charge carrier density p whilst the anomalous Hall coefficient R_A depends on a variety of material specific parameters and, in particular, the longitudinal resistivity ρ_xx.

$$R_0 = \frac{1}{ped} \tag{1.6.4}$$

$$R_\mathrm{A} \propto \rho_\mathrm{xx}^n \tag{1.6.5}$$

The anomalous Hall contribution is typically much greater than that of the ordinary Hall effect. Equation (1.6.3) can therefore be simplified and rewritten to relate M directly to ρ_{xy} and ρ_{xx}.

$$M \propto \frac{\rho_{\mathrm{xy}}}{\rho_{\mathrm{xx}}^{n}} \tag{1.6.6}$$

Measurements of both the longitudinal and transverse resistances can therefore be used in place of the magnetisation plotting $(\frac{\rho_{\mathrm{xy}}}{\rho_{\mathrm{xx}}^{n}})^2$ against $\frac{H}{(\rho_{\mathrm{xy}}/\rho_{\mathrm{xx}}^{n})}$ for a series of isotherms following the same approach as the standard Arrott plots. Competing theories on metals suggest the scaling exponent between R_{A} and ρ_{xx} to be either $n = 1$ due to anisotropic (skew) scattering (Smit (1955, 1958)) or $n = 2$ due to a side-jump mechanism (Berger (1970)). More recent theoretical work focused on the (III,Mn)V semiconductors suggests that for (Ga,Mn)As this exponent should be equal to two (Jungwirth *et al.* (2002)).

1.7 Properties of (Ga,Mn)As

1.7.1 Transport Properties

Whilst the techniques given in section 1.6 are the most widely accepted methods of calculating a material's Curie temperature, early work on (Ga,Mn)As suggested a potential alternative without the need for a SQUID system or the time required for Arrott plot analysis. Past papers studying both the transport and magnetic properties of (Ga,Mn)As demonstrated a close correlation between the Curie temperature from the magnetisation and the peak in resistance (Potashnik *et al.* (2001); Eid *et al.* (2005)). A number of theories were postulated to try to explain this behaviour based on the coherent scattering from long wavelength spin fluctuations and the early work of De Gennes and Friedel (1958).

With a high number of the early studies also showing similar behaviour, measuring the sample resistance as a function of temperature became an accepted approach to quickly calculating T_{c} to such an extent that groups continue to apply this method when characterising the highest T_{c} (Ga,Mn)As (Chen *et al.*

(2011)). Unfortunately, work performed by Novák *et al.* (2008) has shown that this technique does not give reliable values for fully annealed samples, and is only approximately true for lower T_c as-grown samples. Applying this method to fully annealed samples tends to overestimate the value by as much as 10 K to 20 K. It is therefore only useful as a guide for T_c when limited to transport measurements.

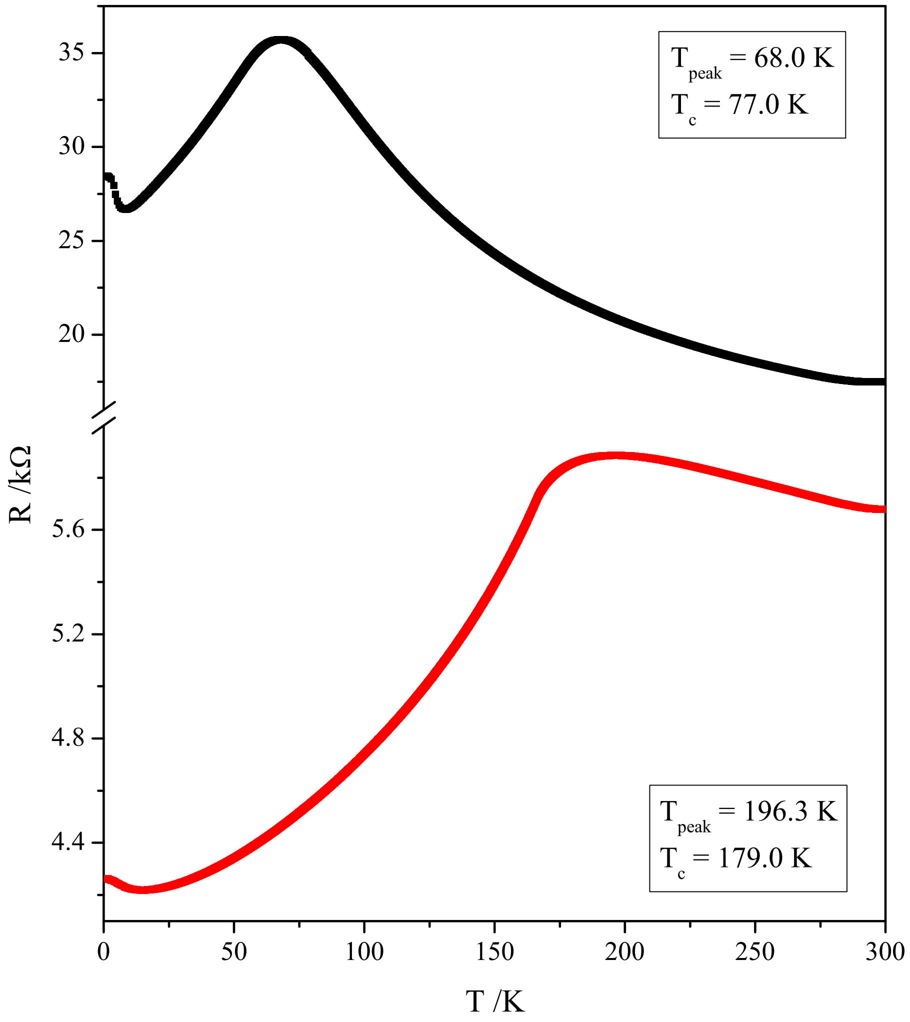

Figure 1.7.1: Typical resistance against temperature plots for as-grown (black) and annealed (red) (Ga,Mn)As samples performed using a standard Hall bar structure. These datasets were taken from an Mn437 sample adjacent to that used to measure the magnetisation shown in figure 1.6.1. The Curie temperature values are therefore that taken from these magnetisation plots on a different sample as rough a comparison to the position of the peak in resistance.

The reason for such a dramatic difference is the change in resistance behaviour seen after annealing. Figure 1.7.1 shows typical examples of both as-grown and annealed behaviour from a 12%, 25 nm (Ga,Mn)As sample taken from the same wafer as that used in figure 1.6.1. The annealed behaviour shown in red not only demonstrates a significant drop in overall resistance and a peak shift to higher temperatures, but also a pronounced change in the shape of the peak.

A typical as-grown sample's resistance tends to increase as the temperature is reduced following an exponential-like form up to a peak. This is frequently found to be close to the sample Curie temperature. In contrast annealed sample behaviour is almost linear at higher temperatures with a much smaller, shallower increase before reaching a peak. The peak itself is also much flatter and broader than that of an as-grown sample with an appreciable shift to higher temperatures relative to the Curie temperature. This shift is clearly demonstrated by the T_c values taken from the adjacent sample magnetisation measurements shown in figure 1.6.1. As-grown datasets also show a more pronounced rise in resistance at lower temperatures due to an additional resistive term on top of that of the expected peak behaviour. It is this added component that results in a peak at lower temperatures close to T_c for as-grown samples.

1.7.2 Magnetic Anisotropy

As briefly discussed at the beginning of section 1.5, magnetic materials such as (Ga,Mn)As exhibit preferred directions of magnetisation called easy axes. These are energetically favourable directions along which moments tend to align under zero applied field. This directional dependence of a material's magnetic properties is called magnetic anisotropy. There are three main types of magnetic anisotropy in ferromagnets: magnetocrystalline, magneto-elastic and shape.

Magnetocrystalline is the most common form of magnetic anisotropy. It is an intrinsic property of ferromagnetic materials that arises from the atomic structure of the crystal. The primary source of the magnetocrystalline anisotropy is spin-orbit coupling: the interaction of the spin magnetic moments with the crystal lattice. Magneto-elastic anisotropy is also derived from the spin-orbit interaction, however, rather than being an intrinsic property it is dictated by strain on the sample. If the lattice is changed by strain the distance between magnetic moments is altered leading to a change in the interaction energies, and therefore the magnetic behaviour.

Whilst the magnetocrystalline is independent of the dimensions of a sample, magnetic anisotropy can also be caused by shape. Shape anisotropy exists in any non-spherical magnetic domain due to the formation of magnetic poles at the edges caused by a dipolar magnetostatic interaction. This creates demagnetising fields that act to oppose the total magnetic moment. Within a spherical domain the magnitude of this field is the same for any given direction due to symmetry, but for a non-symmetric domain the field can be stronger in certain directions. For a long and narrow magnetic domain, for example, the demagnetising field is stronger across the width, this leads to a magnetic easy axis parallel to the length.

The strength of the demagnetising field depends on the magnitude of the sample magnetisation and a demagnetising factor: a coefficient between zero and one which determines the preferred direction. For a cube this takes a value of $\frac{1}{3}$ along each of the orthogonal axes, but for a wire the value is roughly 1 across its width, but close to 0 along the length.

The magnetic anisotropy of (Ga,Mn)As is dominated by the the magnetocrystalline and magnetoelastic terms with shape anisotropy being much less significant due to the low moment density. The cubic symmetry of the (Ga,Mn)As lattice provides a cubic magnetocrystalline term resulting in a specific case of bi-axial anisotropy in which the two easy axes are at ninety degrees. Typically (Ga,Mn)As films demonstrate a competition between this cubic anisotropy, and a uniaxial component of unknown origin. Both of these components lie in-plane due to a symmetric, compressive growth strain arising from a lattice mismatch between the (Ga,Mn)As film and GaAs substrate.

The exact details of the magnetic anisotropy in (Ga,Mn)As varies greatly betweem samples, but in general the cubic term is found to have a stronger temperature dependence with samples tending toward uniaxial behaviour upon approaching T_c. For annealed samples this uniaxial anisotropy can persist down

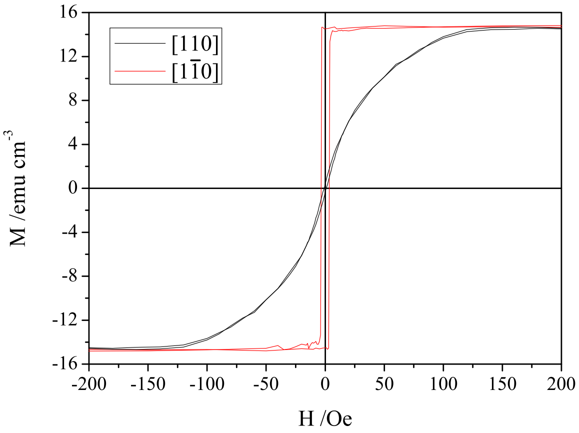

(a) Uniaxial

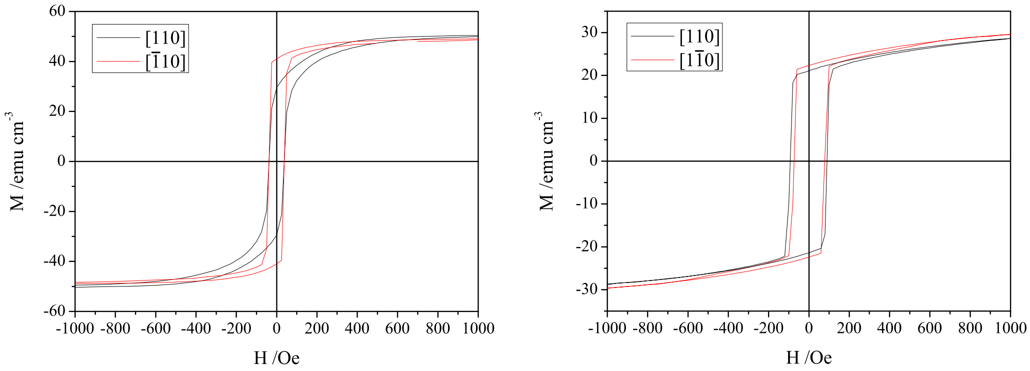

(b) Bi-axial **(c)** Cubic

Figure 1.7.2: Typical examples of (Ga,Mn)As datasets dominated by (a) uniaxial, (b) bi-axial and (c) cubic anisotropy.

to low temperatures, but cubic or biaxial can frequently become dominant at lower temperatures, particularly in as-grown samples. The anisotropic behaviour of samples can even be changed by the annealing process due to the sensitive dependence of the anisotropy on hole concentration and strain. The behaviour of the magnetic anisotropy in (Ga,Mn)As films has been modelled in the past using a single domain model with the unknown uniaxial term included via an artificial anisotropic shear strain (King *et al.* (2011)).

Figure 1.7.2 shows field-loop datasets from three as-grown samples which exhibit dominant (a) uniaxial, (b) bi-axial and (c) cubic behaviour. These are all past datasets performed by different members of the group, both the bi-axial and cubic examples were taken at 2 K, and the uniaxial at 60 K. As with many as-grown samples the uniaxial sample becomes bi-axial at lower temperatures.

Figure 1.7.2a demonstrates strong uniaxial behaviour along the $[1\bar{1}0]$ direction with a quick switch at low fields. The sample in 1.7.2b also shows a sharp change at low field, however, this is accompanied by a more gradual curved profile at higher fields. This behaviour is seen in both the $[1\bar{1}0]$ and [110] directions, but with clear difference between them. The behaviour seen in 1.7.2c is very similar to that in 1.7.2b, however, unlike the bi-axial sample both directions are the same suggesting a largely cubic dominated anisotropy.

References

Arrott, A. 'Criterion for ferromagnetism from observations of magnetic isotherms'. *Physical Review*, **108** (6) 1394–1396, (1957).

Baibich, M. N., Broto, J. M., Fert, A., Van Dau, F. N., Petroff, F., Etienne, P., Creuzet, G., Friederich, A., and Chazelas, J. 'Giant magnetoresistance of (001)Fe/(001)Cr magnetic superlattices'. *Physical Review Letters*, **61** (21) 2472–2475, (1988).

Berger, L. 'Side-Jump Mechanism for the Hall Effect of Ferromagnets'. *Physical Review B*, **2** (11) 4559–4566, (1970).

Binasch, G., Grünberg, P., Saurenbach, F., and Zinn, W. 'Enhanced magnetoresistance in layered magnetic structures with antiferromagnetic interlayer exchange'. *Physical Review B*, **39** (7) 4828–4830, (1989).

Campion, R. P., Edmonds, K. W., Zhao, L. X., Wang, K. Y., Foxon, C. T., Gallagher, B. L., and Staddon, C. R. 'High-quality GaMnAs films grown with arsenic dimers'. *Journal of Crystal Growth*, **247** (1) 42–48, (2003).

Chen, L., Yang, X., Yang, F., Zhao, J., Misuraca, J., Xiong, P., and von Molnár, S. 'Enhancing the Curie Temperature of Ferromagnetic Semiconductor (Ga,Mn)As to 200 K via Nanostructure Engineering'. *Nano Letters*, **11** (7) 2584–2589, (2011).

Cho, A. Y. 'Morphology of Epitaxial Growth of GaAs by a Molecular Beam Method: The Observation of Surface Structures'. *Journal of Applied Physics*, **41** (7) 2780–2786, (1970).

De Gennes, P. G. and Friedel, J. 'Anomalies de résistivité dans certains métaux magníques'. *Journal of Physics and Chemistry of Solids*, **4** 71–77, (1958).

Dietl, T., Ohno, H., Matsukura, F., Cibert, J., and Ferrand, D. 'Zener Model Description of Ferromagnetism in Zinc-Blende Magnetic Semiconductors'. *Science*, **287** (5455) 1019–1022, (2000).

Edmonds, K. W., Wang, K. Y., Campion, R. P., Neumann, A. C., Farley, N. R. S., Gallagher, B. L., and Foxon, C. T. 'High-Curie-temperature GaMnAs obtained by resistance-monitored annealing'. *Applied Physics Letters*, **81** 4991, (2002).

Edmonds, K. W., Bogusławski, P., Wang, K. Y., Campion, R. P., Novikov, S. N., Farley, N. R. S., Gallagher, B. L., Foxon, C. T., Sawicki, M., Dietl, T., Buongiorno Nardelli, M., and Bernholc, J. 'Mn Interstitial Diffusion in (Ga,Mn)As'. *Physical Review Letters*, **92** (3) 037201, (2004).

Eid, K. F., Sheu, B. L., Maksimov, O., B., S. M., Schiffer, P., and Samarth, N. 'Nanoengineered Curie temperature in laterally patterned ferromagnetic semiconductor heterostructures'. *Physical Review Letters*, **86** (15) 152505, (2005).

Gaj, J. A., Ginter, J., and Galazka, R. R. 'Exchange Interaction of Manganese 3d^5 States with Band Electrons in Cd$_{1-x}$Mn$_x$Te'. *Physica Status Solidi (b)*, **89** (2) 655–662, (1978).

Hayashi, T., Tanaka, M., Seto, K., Nishinaga, T., and Ando, K. 'III–V based magnetic (GaMnAs)/nonmagnetic (AlAs) semiconductor superlattices'. *Applied Physics Letters*, **71** 1825, (1997).

Jaczynski, M., Kossut, J., and Galazka, R. R. 'Influence of Exchange Interaction on the Quantum Transport Phenomena in Hg$_{1-x}$Mn$_x$Te'. *Physica Status Solidi (b)*, **88** (1) 73–85, (1978).

Jungwirth, T., Niu, Q., and MacDonald, A. H. 'Anomalous Hall Effect in Ferromagnetic Semiconductors'. *Physical Review Letters*, **88** (20) 207208, (2002).

Jungwirth, T., Wang, K. Y., Mašek, J., Edmonds, K. W., König, J., Sinova, J., Polini, M., Goncharuk, N. A., MacDonald, A. H., and Sawicki, M. 'Prospects for high temperature ferromagnetism in (Ga,Mn)As semiconductors'. *Physical Review B*, **72** (16) 165204, (2005).

Jungwirth, T., Sinova, J., Mašek, J., Kučera, J., and MacDonald, A. H. 'Theory of ferromagnetic (III, Mn) V semiconductors'. *Reviews of Modern Physics*, **78** (3) 809–864, (2006).

King, C. S., Zemen, J., Olejník, K., Horák, L., Haigh, J. A., Novák, V., Irvine, A. Kučera, J., Holý, V., Campion, R. P., Gallagher, B. L., and Jungwirth, T. 'Strain control of magnetic anisotropy in (Ga,Mn)As microbars'. *Physical Review B*, **83** (11) 115312, (2011).

Ku, K. C., Potashnik, S. J., Wang, R. F., Chun, S. H., Schiffer, P., Samarth, N., Seong, M. J., Mascarenhas, A., Johnston-Halperin, E., Myers, R. C., Gossard, A. C., and Awschalom, D. D. ‘Highly enhanced Curie temperature in low-temperature annealed [Ga,Mn]As epilayers’. *Applied Physics Letters*, **82** (14) 2302–2304, (2003).

MacDonald, A. H., Schiffer, P., and Samarth, N. ‘Ferromagnetic semiconductors: moving beyond (Ga,Mn)As’. *Nature Materials*, **4** (3) 195–202, (2005).

Matsukura, F., Ohno, H., Shen, A., and Sugawara, Y. ‘Transport properties and origin of ferromagnetism in (Ga,Mn)As’. *Physical Review B*, **57** (4) 2037–2040, (1998).

Mauger, A. and Godart, C. ‘The magnetic, optical, and transport properties of representatives of a class of magnetic semiconductors: the europium chalcogenides’. *Physics Reports*, **141** (2-3) 51–176, (1986).

Munekata, H., Ohno, H., Von Molnar, S., Segmüller, A., Chang, L. L., and Esaki, L. ‘Diluted magnetic III-V semiconductors’. *Physical Review Letters*, **63** (17) 1849–1852, (1989).

Munekata, H., Zaslavsky, A., Fumagalli, P., and Gambino, J. ‘Preparation of (In,Mn)As/(Ga,Al)Sb magnetic semiconductor heterostructures and their ferromagnetic characteristics’. *Applied Physics Letters*, **63** (21) 2929–2931, (1993).

Neumaier, D., Wagner, K., Geißler, S., Wurstbauer, U., Sadowski, J., Wegscheider, W., and Weiss, D. ‘Weak Localization in Ferromagnetic (Ga,Mn)As Nanostructures’. *Physical Review Letters*, **99** (11) 116803, (2007).

Novák, V., Olejník, K., Wunderlich, J., Cukr, M., Výborný, K., Rushforth, A. W., Edmonds, K. W., Campion, R. P., Gallagher, B. L., Sinova, J., and Jungwirth, T. ‘Curie Point Singularity in the Temperature Derivative of Resistivity in (Ga,Mn)As’. *Physical Review Letters*, **101** (7) 077201, (2008).

Ohno, H. ‘Making nonmagnetic semiconductors ferromagnetic’. *Science*, **281** (5379) 951, (1998).

Ohno, H. ‘Properties of ferromagnetic III-V semiconductors’. *Journal of magnetism and magnetic materials*, **200** (1-3) 110–129, (1999).

Ohno, H., Munekata, H., Penney, T., Von Molnar, S., and Chang, L. L. ‘Magnetotransport properties of p-type (In,Mn)As diluted magnetic III-V semiconductors’. *Physical Review Letters*, **68** (17) 2664–2667, (1992).

Ohno, H., Shen, A., Matsukura, F., Oiwa, A., Endo, A., Katsumoto, S., and Iye, Y. ‘(Ga,Mn)As: A new diluted magnetic semiconductor based on GaAs’. *Applied Physics Letters*, **69** 363, (1996).

Olejník, K., Owen, M. H. S., Novák, V., Mašek, J., Irvine, A. C., Wunderlich, J., and Jungwirth, T. ‘Enhanced annealing, high Curie temperature, and low-voltage gating in (Ga,Mn)As: A surface oxide control study’. *Physicsal Review B*, **78** (5) 054403, (2008).

Owen, G. and Rissman, P. ‘Proximity effect correction for electron beam lithography by equalization of background dose’. *Journal of Applied Physics*, **54** (6) 3573–3581, (1983).

Potashnik, S. J., Ku, K. C., Chun, S. H., Berry, J. J., Samarth, N., and Schiffer, P. ‘Effects of annealing time on defect-controlled ferromagnetism in $\mathrm{Ga}_{1-x}\mathrm{Mn}_x\mathrm{As}$’. *Applied Physics Letters*, **79** (10) 1495, (2001).

Rai-Choudhury, P. *Handbook of microlithography, micromachining, and microfabrication, Vol. 1 & 2.* SPIE Press and IEE Press, (1997).

Rokhinson, L. P., Lyanda-Geller, Y., Ge, Z., Shen, S., Liu, X., Dobrowolska, M., and Furdyna, J. K. ‘Weak localization in (Ga,Mn)As: evidence of impurity band transport’. *Physical Review B*, **76** (16) 161201, (2007).

Smit, J. ‘The spontaneous hall effect in ferromagnetics I’. *Physica*, **21** (9) 877–887, (1955).

Smit, J. ‘The spontaneous hall effect in ferromagnetics II’. *Physica*, **24** (1) 39–51, (1958).

Story, T., Gałązka, R. R., Frankel, R. B., and Wolff, P. A. ‘Carrier-concentration–induced ferromagnetism in PbSnMnTe’. *Physical Review Letters*, **56** (7) 777–779, (1986).

van Esch, A., van Bockstal, L., de Boeck, J., Verbanck, G., van Steenbergen, A. S., Wellmann, P. J., Grietens, B., Bogaerts, R., Herlach, F., and Borghs, G. ‘Interplay between the magnetic and transport properties in the III-V diluted magnetic semiconductor $Ga_{1-x}Mn_xAs$'. *Physical Review B*, **56** (20) 13103–13112, (1997).

Wang, K. Y., Campion, R. P., Edmonds, K. W., Sawicki, M., Dietl, T., Foxon, C. T., and Gallagher, B. L. 'Magnetism in (Ga,Mn)As Thin Films With T_c Up To 173 K'. *AIP Conference Proceedings*, **772** (1) 333–334, (2005)a.

Wang, K. Y., Edmonds, K. W., Zhao, L. X., Sawicki, M., Campion, R. P., Gallagher, B. L., and Foxon, C. T. '(Ga,Mn)As grown on (311) GaAs substrates: Modified Mn incorporation and magnetic anisotropies'. *Physical Review B*, **72** (11) 115207, (2005)b.

Wang, M., Campion, R. P., Rushforth, A. W., Edmonds, K. W., Foxon, C. T., and Gallagher, B. L. 'Achieving high Curie temperature in (Ga,Mn)As'. *Applied Physics Letters*, **93** (13) 132103, (2008).

Yasin, S., Hasko, D. G., and Ahmed, H. 'Comparison of MIBK/IPA and water/IPA as PMMA developers for electron beam nanolithography'. *Microelectronic Engineering*, **61** 745–753, (2002).

Yu, K. M., Walukiewicz, W., Wojtowicz, T., Kuryliszyn, I., Liu, X., Sasaki, Y., and Furdyna, J. K. 'Effect of the location of Mn sites in ferromagnetic $\mathrm{Ga_{1-x}Mn_xAs}$ on its Curie temperature'. *Physical Review B*, **65** (20) 201303, (2002).

Zailer, I., Frost, J. E. F., Chabasseur-Molyneux, V., Ford, C. J. B., and Pepper, M. 'Crosslinked PMMA as a high-resolution negative resist for electron beam lithography and applications for physics of low-dimensional structures'. *Semiconductor Science and Technology*, **11** (8) 1235–1238, (1996).

Zener, C. 'Interaction Between the d Shells in the Transition Metals'. *Physical Review*, **81** (3) 440–444, (1951).

Chapter 2

Critical Behaviour in (Ga,Mn)As

2.1 Introduction

One of the most important areas within condensed-matter physics is the study of phase transitions. These are points in parameter space at which a system moves from state in thermodynamic equilibrium to another. They are manifested as sudden or sharp changes in various physical quantities. There are two types of phase transition: discontinuous phase transitions which are accompanied by the release of latent heat, and continuous phase transitions that are not. Critical phenomena are the behaviour of a material's properties at or around a continuous phase transition.

Phase transitions can be driven by a number of parameters; a typical example of this is the temperature with systems tending to move from an ordered state at low-temperatures to a disordered state at higher temperatures. One of the most studied continuous phase transitions driven by temperature is that of a ferromagnetic material which becomes paramagnetic above a certain critical point. The temperature at which this transitions occurs is called the Curie temperature T_c named after the French physicist Pierre Curie.

One of the most interesting aspects of continuous phase transitions is that the behaviour of a material's properties close to the critical point is found to be the same across many different physical systems, and that this behaviour only depends on a small number of parameters. Power-law scaling relations can be derived between different quantities, such as the specific heat and magnetic susceptibility, described by critical exponents which fall into a number of distinct universality classes. The study of this behaviour close to T_c within ferromagnets is very useful in the understanding of their magnetic and electronic properties.

Studies of critical phenomena and continuous phase transitions were originally performed in the sixties and seventies on transition-metal ferromagnets such as nickel (Kouvel and Fisher (1964)) and iron (Lederman *et al.* (1974)). Measurements and detailed analysis of the magnetic properties of these materials close to the Curie temperature allowed the calculation of power-law exponents with strong agreements to theoretical models.

With these 3d elemental ferromagnets now fairly well understood more recent work on critical phenomena has focused on more complex systems such as perovskite structures and the DMSs. Measurements within various perovskite manganites (Kar *et al.* (2006); Ghosh *et al.* (2006); Fan *et al.* (2010)) have shown that it is possible to make calculations of the critical exponents of such systems applying similar methods to that used on the aforementioned metals. Despite this, conclusions drawn from papers on the same material are frequently in disagreement due to only small differences between the expected mean-field, Heisenberg or Ising modelled critical exponents. Work on the pervoskite $\mathrm{SrRuO_3}$ has also demonstrated critical behaviour within $\frac{\mathrm{d}R}{\mathrm{d}T}$ (Kats *et al.* (2001); Kim *et al.* (2003)), however, in similar manner to that seen in the manganite studies, conclusions regarding the exponent values have been varied.

This disparity between results suggests that there are a number of inherent difficulties associated with these more complex structures over the metals. This would also imply that critical behaviour studies on (Ga,Mn)As are likely to pose a number of problems when trying to calculate accurate, reproducible critical exponent values. The limited number of experimental papers focused on the subject supports this with observations of critical behaviour (Jiang *et al.* (2009); Khazen *et al.* (2010); Yuldashev *et al.* (2011)) leading to very mixed or imprecise results. Section 2.4 gives a more in-depth overview of some of the experimental work performed up to this point on the critical behaviour of (Ga,Mn)As.

With this past work in mind the focus of this chapter will be on the measurement of the magnetic properties of (Ga,Mn)As close to T_c with the aim of confirming the Heisenberg-like critical behaviour predicted by Priour and Das Sarma (2010). Both magnetisation and susceptibility measurements will be performed in order to calculate exponents β and γ respectively, and field-sweep measurements made to accurately calculate sample Curie temperatures. The next section will cover the background theory of critical phenomena, including phase transitions and universality classes, before giving a basic overview of a number of the more well known ferromagnetic models. The chapter will then move on to discuss the measurements themself with information regarding setup optimisation, the data analysis techniques used to obtain accurate exponent values, and comparisons to past datasets to confirm the observed behaviour over a wider range of samples.

2.2 Theoretical Background

2.2.1 Phase Transitions

Before considering critical behaviour the first thing that must be understood is the concept of phases and the types of transition from one phase to another. All systems in thermodynamic equilibrium exist in different phases throughout which all physical properties are essentially uniform. The most well known examples of this within the real world are the states of matter. The solid, liquid and gas states of H_2O particularly are a regular feature, and even a requirement, of everyday life.

In general, phase transitions are defined as points in parameter space at which the thermodynamic potential becomes non-analytic. Such a failure of analyticity can only occur at the thermodynamic limit when the system size is assumed to be infinite. Theoretical models therefore always consider this bulk limit. Within experiment this limit is not strictly reached; however, a typical macroscopic system does contain roughly 10^{23} degrees of freedom enough to observe the effects of critical behaviour.

Transitions can be classified in a number of ways, the first was proposed by P. Ehrenfest based on the behaviour of the free energy at or around a phase boundary. This method results in two main groups: first order and second order phase transitions. The changes between states of matter are an example of first order transitions, and the magnetic transition of (Ga,Mn)As studied within this chapter an example of a second order transition.

In the Ehrenfest classification system a first order transition involves discontinuous behaviour in one or more of the first partial derivatives of the free energy; for example the entropy $-\frac{\partial F}{\partial T}$. Within second order transitions these remain continuous, and it is the second order derivatives that demonstrate a discontinuity. Two examples of this in a magnetic system such as (Ga,Mn)As are the specific heat and the susceptibility. Unfortunately, whilst such classification does group similar transitions together it is limited to a purely thermodynamic view of the phenomena and is not always precise.

A more complete form of classification based on the theoretical work of L. D. Landau involves the presence of a latent heat and a breaking of symmetry at the phase transition. In 1937 Landau suggested that continuous phase transitions are a manifestation of a broken symmetry, and noted that transitions without a break in symmetry are accompanied by a latent heat. Therefore within this new system first order, or discontinuous, phase transitions are classified as that which involve a latent heat, and second order, or continuous, phase transitions classified as that which do not involve a latent heat. Figure 2.2.1 shows examples of both types of phase transition.

Landau's approach to second order phase transitions also involves the introduction of the idea of order parameters that are zero in one state and non-zero in the other. A zero value means that the symmetry of the ground state is the same as that of the Hamiltonian whilst a non-zero value means that the symmetry has been broken. In most cases the order parameter is found to vanish on the high-temperature side of the transition. Systems are generally more ordered at lower temperatures because the interactions between atoms are able to overcome the effects of thermal motion. The order parameter is therefore a measure of the order present within a system.

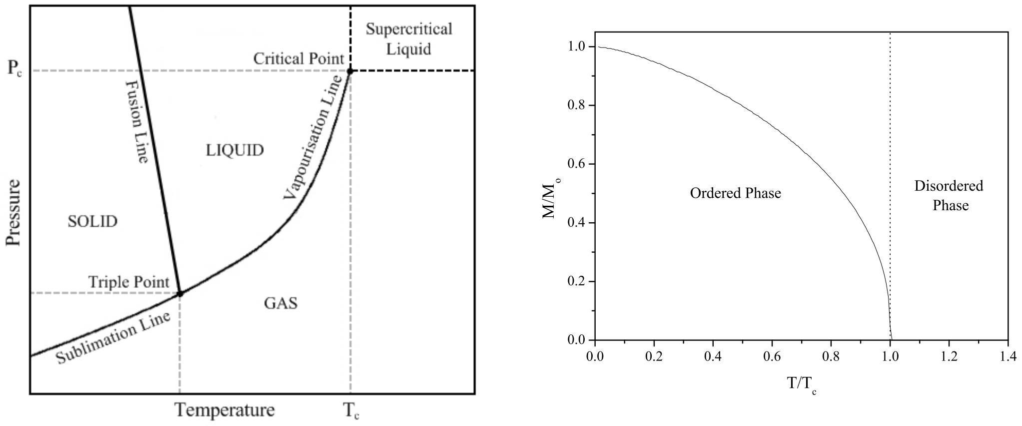

(a) (b)

Figure 2.2.1: (a) A typical phase diagram of a thermodynamic system at equilibrium showing three distinct states of matter. This is an example of a first order phase transition in which the order parameter is the density. (b) A magnetisation against temperature plot from (Ga,Mn)As sample Mn438_a2 measured in Nottingham. A second order phase transition occurs at the Curie temperature T_c.

Within ferromagnetism the order parameter of a system is the spontaneous magnetisation M. In this case the critical point is called the Curie temperature T_c which separates the disordered paramagnetic phase above T_c from the ordered ferromagnetic phase below T_c. The magnetisation is zero in the paramagnetic phase above T_c, and non-zero in the ferromagnetic phase below T_c. The order parameter is therefore a physical quantity that clearly distinguishes between phases.

An idealised ferromagnetic system can be modelled by a Hamiltonian consisting of a lattice of elementary magnets. Interactions between these magnets are rotationally invariant such that the Hamiltonian itself is rotationally invariant. Above T_c the system is paramagnetic and the magnetisation zero, consequently the ground state is also rotationally invariant. However, below T_c the system becomes spontaneously magnetised in a certain direction resulting in the ground state not being rotationally invariant. The state of the system therefore does not show the symmetry of the Hamiltonian. Further information regarding the Landau-Ginzburg model, order parameters and spontaneous symmetry breaking can be found in Binney *et al.* (1992).

The first basic model developed for the understanding of magnetic phase transitions was mean-field theory. Below the Curie temperature within a ferromagnet there is a spontaneous magnetisation with no applied magnetic field suggesting an ordered arrangement of the electron spins. This alignment is then broken down by thermal motion above T_c. Within mean-field theory this behaviour is modelled via an internal interaction between moments called the exchange field equivalent to a magnetic field B_E. Each magnetic moment is assumed to experience a field proportional to the magnetisation as shown by equation (2.2.1). This mean-field approximation effectively simplifies the many-body statistical problem to a single-body problem.

$$B_\mathrm{E} = \lambda M \tag{2.2.1}$$

This can be combined with the simplified paramagnetic Brillouin function for the magnetisation using a total angular momentum $J = \frac{1}{2}$ to form equation (2.2.2) with an external magnetic field of H. Here N is the number of moments, μ the magnetic moment per site, and k_B the Boltzmann constant.

$$M = N\mu \tanh\left(\frac{\mu H + \mu\lambda M}{k_\mathrm{B}T}\right) \tag{2.2.2}$$

This can then be rewritten in terms of the reduced field h, reduced magnetisation m, and reduced temperature t as defined by (2.2.4).

$$m = \tanh\left(\frac{h+m}{1-t}\right) \tag{2.2.3}$$

$$\begin{aligned} h &= \frac{H}{H_0} & m &= \frac{M}{M_0} & t &= \left|\frac{T-T_\mathrm{c}}{T_\mathrm{c}}\right| \\ &= \frac{H}{N\mu\lambda} & &= \frac{M}{N\mu} & &= 1 - \frac{k_\mathrm{B}T}{N\mu^2\lambda} \end{aligned} \tag{2.2.4}$$

By expanding (2.2.3) as a Taylor series to the second term (2.2.5) and rearranging, the mean-field equation of state close to T_c can be derived as shown by equation (2.2.6).

$$m \cong \frac{h+m}{1-t} - \frac{1}{3}\left(\frac{h+m}{1-t}\right)^3 \tag{2.2.5}$$

$$\frac{h}{m} = -t + \frac{m^2}{3} \tag{2.2.6}$$

This equation predicts that under zero field the remanent magnetisation should show a power law behaviour of t^{β} close to T_{c} in which the exponent $\beta = \frac{1}{2}$. Similarly just above T_{c} the magnetic susceptibility $\chi = \frac{M}{H}$ is predicted to show a $t^{-\gamma}$ dependence in which $\gamma = 1$. However, such behaviour is not observed experimentally: within three-dimensional systems the exponents are found to be closer to $\beta = \frac{1}{3}$ and $\gamma = \frac{4}{3}$.

A disagreement with experiment is also observed at lower temperatures with the experimental results demonstrating a much more rapid temperature dependence of the magnetisation. For $T \ll T_{\mathrm{c}}$ equation (2.2.2) with zero external field can be approximated to

$$\Delta M = M(0) - M(T) \cong 2N\mu \exp\left(\frac{-2\lambda\mu^2}{k_{\mathrm{B}}T}\right) \tag{2.2.7}$$

However, experimental results show the magnetisation to follow a $T^{\frac{3}{2}}$ dependence as seen in equation (2.2.8).

$$\frac{\Delta M}{M(0)} = AT^{3/2} \tag{2.2.8}$$

This behaviour is the result of collective oscillations of the coupled magnetic moments called magnons. It can be derived from the total number of magnons excited at a given temperature as shown in most solid state textbooks (Kittel (2005), p.334).

2.2.2 Universality

One of the major disadvantages of the mean-field theory is that it does not take in to account the effects of fluctuations resulting in the large disagreement with experiment. However, it does offer a basis for the theory of phase transitions that is partially correct. Mean-field theory suggests a single universal behaviour of properties close to T_c that is found not to be the case. Measurements across a wide variety of very different systems show that there are a restricted number of universality classes which arise from the types of order parameter, system symmetry and dimensionality.

Each class has its own set of critical exponents that describe the power law behaviour of properties in the critical region close to T_c. The expected power law behaviour of the properties most relevant to the (Ga,Mn)As measurements taken in this chapter are shown by (2.2.9). Both the magnetisation M and susceptibility χ dependences on the reduced temperature t are effectively generalisations of that found from the mean-field theory.

$$M \propto t^{\beta} \qquad T \rightarrow T_\mathrm{c} \text{ from below, } H = 0 \tag{2.2.9a}$$

$$\chi \propto t^{-\gamma} \qquad T \rightarrow T_\mathrm{c} \text{ from above, } H = 0 \tag{2.2.9b}$$

$$M \propto H^{\frac{1}{\delta}} \qquad \text{at } T = T_\mathrm{c} \tag{2.2.9c}$$

$$C_H \propto t^{-\alpha} \qquad T \rightarrow T_\mathrm{c},\ H = 0 \tag{2.2.9d}$$

Here the specific heat is shown to diverge in a way similar to that of the susceptibility with a critical exponent $\alpha > 0$. However, within real systems C_H can also be seen to show a much slower $\log(\frac{1}{t})$ divergence or even a finite peak.

Equation (2.2.10) shows how the logarithmic behaviour can be considered to be the case in which $\alpha = 0$.

$$\log\left(\frac{1}{t}\right) = \lim_{\alpha \rightarrow 0+} \frac{1}{\alpha}\left(t^{-\alpha} - 1\right) \tag{2.2.10}$$

In the case of a finite peak favourable fitting is usually found to equation (2.2.11). Comparing this to (2.2.10) suggests that these are examples of negative α.

$$C_H = \frac{A}{|\alpha|}\left(1 - t^{|\alpha|}\right) \tag{2.2.11}$$

All three cases are generally embraced within the single formula

$$C_H \propto \frac{1}{\alpha}\left(t^{-\alpha} - 1\right) \tag{2.2.12}$$

The power laws shown by (2.2.9) can be derived from the Widom scaling hypothesis in which the Gibb's free energy $f(T,H)$ close to T_c is approximated to a function of the form

$$f(T,H) = t^{\frac{1}{w}}\Psi_{\pm}\left(\frac{H}{t^{u/w}}\right) \tag{2.2.13}$$

where $\Psi_+(z)$ and $\Psi_-(z)$ are two different functions of a single variable for $T > T_\mathrm{c}$ and $T < T_\mathrm{c}$ respectively. This scaling form of the free energy guarantees that the critical exponents are the same above and below T_c. The magnetic properties of a system are related to the free energy by the equations shown below.

$$M|_{H=0} = -\left(\frac{\partial f}{\partial H}\right)_T \qquad = -t^{\left(\frac{1-u}{w}\right)}\Psi'_{\pm}(0) \tag{2.2.14a}$$

$$\chi|_{H=0} = -\left(\frac{\partial^2 f}{\partial H^2}\right)_T \qquad = -t^{\left(\frac{1-2u}{w}\right)}\Psi''_{\pm}(0) \tag{2.2.14b}$$

$$M|_{T=T_\mathrm{c}} = -\left(\frac{\partial f}{\partial H}\right)_T \qquad = -\frac{1}{u}H^{\left(\frac{1}{u}-1\right)}\tilde{\Psi}_{\pm}(\infty) \tag{2.2.14c}$$

$$C_H = -T\left(\frac{\partial^2 f}{\partial T^2}\right)_H \simeq \frac{\Psi_{\pm}(0)}{T_\mathrm{c}}\frac{1}{w}\left(\frac{1}{w} - 1\right)t^{\left(\frac{1}{w}-2\right)} \tag{2.2.14d}$$

When calculating the relation between M and H at $T = T_\mathrm{c}$ (2.2.14c) the Widom scaling hypothesis is re-expressed as

$$f(T,H) = H^{\frac{1}{u}}\tilde{\Psi}\left(\frac{H}{t^{u/w}}\right) \qquad \text{where} \qquad \tilde{\Psi}(z) \equiv z^{\frac{-1}{u}}\Psi(z) \tag{2.2.15}$$

Comparing these results to that shown by (2.2.9) leads to

$$\beta = \frac{1-u}{w} \qquad \gamma = \frac{2u-1}{w} \qquad (2.2.16)$$

$$\delta = \frac{u}{1-u} \qquad \alpha = 2 - \frac{1}{w}$$

Relations can therefore be derived between critical exponents from the same universality class. Those most relevant to this work are shown by (2.2.17).

$$\alpha + 2\beta + \gamma = 2 \qquad \text{Rushbrooke's scaling law} \qquad (2.2.17a)$$

$$\alpha + \beta\,(1+\delta) = 2 \qquad \text{Griffiths' scaling law} \qquad (2.2.17b)$$

$$\gamma = \beta\,(\delta - 1) \qquad \text{Widom's scaling law} \qquad (2.2.17c)$$

These laws were originally derived as inequalities phenomenologically via thermodynamic arguments and are converted to equalities by the scaling hypothesis. An example of such a derivation for the Rushbrooke inequality is shown below by first considering the purely mathematical relation (2.2.18) for the entropy S.

$$\left(\frac{\partial S}{\partial T}\right)_M = \left(\frac{\partial S}{\partial T}\right)_H + \left(\frac{\partial S}{\partial H}\right)_T \left(\frac{\partial H}{\partial T}\right)_M \qquad (2.2.18)$$

Substitutions into this can be made using equations relating the entropy to the specific heat (2.2.19), the Maxwell relation shown by (2.2.20), and the partial derivative relation (2.2.21).

$$C_M = T\left(\frac{\partial S}{\partial T}\right)_M \qquad C_H = T\left(\frac{\partial S}{\partial T}\right)_H \qquad (2.2.19)$$

$$\left(\frac{\partial S}{\partial H}\right)_T = \left(\frac{\partial M}{\partial T}\right)_H \qquad (2.2.20)$$

$$\left(\frac{\partial H}{\partial T}\right)_M = -\left(\frac{\partial H}{\partial M}\right)_T \left(\frac{\partial M}{\partial T}\right)_H \qquad (2.2.21)$$

Equation (2.2.22) shows the result of these substitutions rearranged as the difference between the specific heats at constant field C_H and constant magnetisation

C_M.

$$C_H - C_M = \frac{T}{\chi_T}\left(\frac{\partial M}{\partial T}\right)_H^2 \tag{2.2.22}$$

This can be combined with the scaling functions shown by (2.2.9), and an inquality formed by removing C_M since the specific heat at constant magnetisation is always greater than zero. Equation (2.2.23) shows the inequality within the critical region below T_c.

$$(T_\mathrm{c} - T)^{-\alpha'} \geq A(T_\mathrm{c} - T)^{\gamma'}(T_\mathrm{c} - T)^{2(\beta-1)} \tag{2.2.23}$$

Therefore for sufficiently small reduced temperature values close to T_c

$$\begin{aligned} -\alpha' &\leq \gamma' + 2(\beta - 1) \\ \therefore \quad \alpha' + 2\beta + \gamma' &\geq 2 \end{aligned} \tag{2.2.24}$$

2.2.3 Ferromagnetic Models

The standard method for modelling ferromagnetism is to consider an idealised magnetic system in which magnetic atoms sit on a periodic lattice. Each atom has an elementary magnetic moment or spin of fixed magnitude. The simplest and most famous form of this is the Ising model first proposed by W. Lenz and put forward in the doctoral thesis of E. Ising (Ising (1925)).

Within the Ising model the spins are described as discrete variables that can exist in one of two states $s_i = \pm 1$. Each spin can then only interact with its nearest neighbours in the lattice through an exchange coupling. The energy of this system is determined by the sum of the interactions between spins and their neighbours on the lattice as shown by (2.2.25).

$$E = -J \sum_{<ij>}^{N} s_i s_j - \mu H \sum_{i}^{N} s_i \tag{2.2.25}$$

where J denotes the exchange coupling energy between nearest neighbours and μ the magnetic moment per spin. The $< ij >$ indicates that the exchange energy is counted only for nearest neighbours. If neighbouring spins point in the same direction then the energy contributed is $-J$, and if they are anti-parallel then the energy is $+J$.

The most straightforward case of this model is in one-dimension consisting of a chain of nearest neighbour interacting spins. Within his original paper Ising numerically solved the 1D case which displayed a T_c value of zero and hence no phase transition or spontaneous magnetisation. However, later analytical work by L. Onsager (Onsager (1944)) showed that a transition is present in two-dimensions.

The Ising model is an example of a scalar model of ferromagnetism identical to the lattice gas model within thermodynamics. Each site on the lattice effectively contains a scalar variable taking one of two values; within the Ising model this is $s = \pm 1$, and within a lattice gas it is whether the site is occupied or unoccupied. The Ising model therefore only describes magnetic systems with an extremely uniaxial anisotropy.

Rather than simply assuming spins can only take parallel or antiparallel values a more general method is to assign a vector to each site. The three-dimensional vector case of this is called the Heisenberg model which allows the moments to point in any direction of space. The Ising model is effectively a simplified case of this in which the direction of the spin vector is restricted to a single axis. The spin vector can therefore be replaced by a scalar with positive and negative signs.

The force aligning neighbouring spins within the Heisenberg model is derived from an energy dependant on the angle between the two spins, and not on their orientation with respect to a fixed axis. Thus if all spins within the system are rotated by the same amount the energy is unchanged. The Heisenberg model is therefore symmetric under arbitrary rotations of the spin; this symmetry is then broken below T_c.

The mean-field, Ising and Heisenberg models are all part of separate universality classes each with their own unique critical exponents. Table 2.1 shows the α, β, γ and δ values of the models detailed in this section and those most relevant to the work in this chapter. As stated earlier the system dimensionality takes a crucial role in determining the universality class, thus the exponent values are different for one-, two- and three-dimensional variants of each respective

	α	β	γ	δ
Mean-Field	0	0.5	1	3
Ising 2D	0	$\frac{1}{8}$	$\frac{7}{4}$	15
Ising 3D	0.11	0.326	1.237	4.8
Heisenberg 3D	-0.13	0.365	1.396	4.8

Table 2.1: The critical exponents of various statistical spin models of magnetism. Samples of (Ga,Mn)As are expected to show Heisenberg-like behaviour.

model.

Section 2.2.1 showed an exact solution to the mean-field model deriving the exponents shown within this table. However, whilst the 1D Ising model is a relatively simple problem to solve, higher dimensional systems are far more complex. The analytical solution derived by Lars Onsager (Onsager (1944)) for the 2D Ising model is highly non-trivial, and the three-dimensional Ising model remains unsolved. There are currently no theories for providing exact predictions to the critical exponents in three-dimensional systems. The values given in table 2.1 for the 3D Ising and Heisenberg models are therefore estimates obtained via approximate methods using both Monte Carlo simulations and perturbation field-theory.

2.2.4 Fluctuations and Renormalisation

When considering the critical phenomena within a magnet the system is built up of atoms placed on a lattice. The spins within this system are coupled over a distance of the order of the correlation length ξ. As the temperature of the system approaches the critical point, fluctuations of increasingly longer wavelength become apparent in the magnetisation. The correlation length is the maximum wavelength of these fluctuations which is infinite at T_{c}.

This divergence results in a serious problem when trying to formulate a model of these fluctuations at a macroscopic scale. Within hydrodynamics, fluid waves can be described by equations that make no reference to the atomic structure because such waves are characterised by a single definite wavelength with very little motion at shorter scales. However, when considering the critical fluctuations in a magnet the longer wavelengths are not dominant. Instead fluctuations occur over all wavelength scales between the correlation length and the atomic spacing of the lattice. All intermediate wavelengths are crucial for the physics of critical phenomena.

Such behaviour requires the taking into account of more than simply the nearest neighbour interactions seen in the previous models. The main theoretical difficulty therefore faced when dealing with critical phenomena is the large number of degrees of freedom involved, and the fact that there is no clear-cut method to decouple them in a systematic way. The most important advancement to this problem came in the 1970s (Wilson (1971)) with the development of a set of mathematical techniques known as renormalisation group theory based on the earlier scaling work of L. P. Kadanoff (Kadanoff (1966)).

The renormalisation group technique establishes a relation between systems of different correlation length. Transformations generated from the renormalisation group effectively change the initial system to an equivalent one with a smaller correlation length and thus fewer degrees of freedom. Repeated transformation stages can therefore lead to a systematic reduction in the effective correlation length to which standard pair interaction models can be applied. Once this problem is solved the correspondences can then be followed back to produce the solution for the original system.

The renormalisation group techniques are not solely limited to critical phenomena, but are useful whenever dealing with fluctuations occurring simultaneously over many length or time scales. The repeated stages effectively eliminate remaining shortest-wavelength fluctuations until only a few macroscopic degrees of freedom remain. The effects of these shorter fluctuations are approximately accounted for by the renormalisation of the interactions among the remaining longer wavelength modes.

The renormalisation group theory justifies the scaling laws shown by (2.2.17). The method enables one to predict which details of a system are relevant to determining the universality class, and which microscopic features are unimportant close to the critical point. It also allows the calculation of the properties of any given universality class; the critical properties of simpler cases have been calculated to a high degree of accuracy, and confirmed by experiment.

Unfortunately, for more complicated cases such a high accuracy is not observed with further improvements to existing renormalisation group calculations still desperately needed. A much more comprehensive overview of renormalisation and renormalisation group theory can be found in Binney *et al.* (1992) chapters 5 and 11, or most textbooks on critical phenomena.

2.3 Measuring Critical Exponents

Before carrying out magnetometry measurements on samples there were number of basic problems that needed to be addressed in order to calculate accurate, reproducible critical exponents. Both the experimental methods and data analysis techniques posed difficulties that first needed to be overcome.

2.3.1 Data Analysis

In past measurements at Nottingham critical exponents were calculated from the magnetisation and susceptibility by simply plotting the appropriate dataset as a log-log graph against $\log(t)$. The exponent would then be taken to be the gradient close to T_c. Unfortunately, this method immediately runs into a number of problems that are not easily resolved. The main problem associated with this method is the requirement for a known single value of the Curie temperature, something that cannot accurately be taken from the raw data.

Whilst theoretically the remanent magnetisation of samples should drop very definitely to zero, measurements always display a slight tail above T_c due to a very small remaining magnetic field within the SQUID or the inhomogeneity of the sample. Changing the value of T_c even by a single Kelvin within the log-log plots can result in a broad range of calculated exponent values that can easily be classified into another one of the known universality classes.

Modified-Arrott Plots

The standard method used to avoid this problem is to perform additional measurements to accurately calculate the sample Curie temperature using Arrott plots as detailed in chapter 1. Unfortunately, this standard Arrott plot method assumes a mean-field model of the behaviour. This is not expected to be the case for the (Ga,Mn)As samples. One potential solution to this problem is to make use of a more general equation of state to that derived from mean-field theory (2.2.6).

Equation (2.3.1) shows an equation of state first proposed by Anthony Arrott and John Noakes (Arrott and Noakes (1967)) for the limit $T \to T_\mathrm{c}$. This was originally given as a partially empirical expression that fitted to earlier magnetisation measurements on Nickel that did not follow the expected mean-field behaviour. The β, γ and δ asymptotic relations shown by (2.2.9) can be derived from this by simply assuming $H \to 0$, $M \to 0$ or $t \to 0$ respectively, and making use of the Widom inequality. Both a and b are temperature-independent coefficients related to the critical amplitudes.

$$\left(\frac{H}{M}\right)^{1/\gamma} = at + bM^{1/\beta} \tag{2.3.1}$$

The Arrott-Noakes formula is an approximation appropriate close to the critical isotherm at $t = 0$ with a 1% level of precision as long as inequality (2.3.2) is satisfied (Campostrini *et al.* (2002)). Here M_0 is defined as the constant of proportionality of the β critical relation: the saturation magnetisation at zero temperature.

$$t\left(\frac{M_0}{M}\right)^{1/\beta} \lesssim 25 \tag{2.3.2}$$

From the Arrott-Noakes formula it can be seen that linear modified-Arrott graphs can be produced by plotting $M^{1/\beta}$ against $(\frac{H}{M})^{1/\gamma}$ using the appropriate universality class critical exponents. Given this requirement the log-log and Arrott method is clearly not a viable option when studying the critical phenomena with each of the steps requiring the result of the other. The only real use for the modified-Arrott plots in this case is therefore as a T_c consistency check after the calculation of β and γ.

Kouvel-Fisher Analysis

An alternative, and relatively simple, method is to use a Kouvel-Fisher plot (Kouvel and Fisher (1964)) in which the power law behaviour of the reduced temperature is effectively removed by dividing the magnetisation or susceptibility by its temperature derivative. A brief mathematical derivation of this can be seen below for the magnetisation case.

$$\begin{aligned} M &= M_0 t^{\beta} \\ t &= \frac{T_\mathrm{c} - T}{T_\mathrm{c}} \end{aligned} \quad \Rightarrow \quad \begin{aligned} \frac{\mathrm{d}M}{\mathrm{d}t} &= \beta \frac{M}{t} \\ \frac{\mathrm{d}t}{\mathrm{d}T} &= -\frac{1}{T_\mathrm{c}} \end{aligned} \quad \Rightarrow \quad \begin{aligned} \frac{\mathrm{d}M}{\mathrm{d}T} &= \frac{\mathrm{d}M}{\mathrm{d}t} \cdot \frac{\mathrm{d}t}{\mathrm{d}T} \\ &= -\beta \frac{M}{T_\mathrm{c} - T} \end{aligned}$$

$$\therefore -\frac{M}{\frac{\mathrm{d}M}{\mathrm{d}T}} = \frac{1}{\beta}(T_\mathrm{c} - T) \tag{2.3.3}$$

A linear fit over the critical region should therefore produce a gradient $m = -\frac{1}{\beta}$ and intercept $c = \frac{T_\mathrm{c}}{\beta}$ without the need for prior knowledge of the sample Curie temperature. This method can also be applied to the susceptibility relating the gradient and intercept to T_c and the critical exponent γ.

2.3.2 Diamagnetic Background

Whilst the Kouvel-Fisher approach to critical exponent data analysis offers a number of advantages over the previously used log-log plots, it still poses a couple of new problems. The most notable of these is related to a constant background or shift in the data. Within the log-log plots this would only manifest itself as a vertical shift with no effect on the gradient, and therefore the calculated critical exponent. Unfortunately, this is not true of the Kouvel-Fisher plots.

The most important example of this is within the susceptibility measurements in which the magnetic field is swept at each temperature. Any form of diamagnetic or paramagnetic material in the SQUID sample holder results in a shift of the measured susceptibility. For the (Ga,Mn)As samples the prominent form of this is caused by the GaAs substrate on which it is grown; this shows a diamagnetic contribution to the susceptibility.

In the past this problem was solved by calculating the background through fitting at higher temperatures and magnetic fields. However, this results in a relatively high associated error which whilst not usually a problem can have a significant effect on the Kouvel-Fisher analysis. Within the first set of measurements carried out on a (Ga,Mn)As sample this diamagnetic background was effectively removed by an iterative approach based on the fitting of a shifted power law (2.3.4) with a fixed T_c.

$$M = M_0\left(1 - \frac{T}{T_\mathrm{c}}\right)^{\beta} + M_\mathrm{shift} \tag{2.3.4}$$

The initial fixed Curie temperature was taken from a shifted Kouvel-Fisher plot with a diamagnetic background $10^{-8}\,\mathrm{emuOe}^{-1}$. This is a rough figure consistent both with previous samples of the same chip size and an open T_c fit to the data with equation (2.3.4). This value could be taken because whilst the Kouvel-Fisher calculated γ varies by a significant amount with background the variation in T_c remains relatively small $\pm 0.2\,\mathrm{K}$.

Given that this method demonstrates similar drawbacks to the original log-log plots, further sample measurements required a different approach in an effort to remove the substrate effects prior to analysis. The SQUID effectively measures the sample magnetisation by measuring the flux change through pick-up coils. The result of this is that a uniform length of material longer than the system coils and movement range would not be shown in measurements.

The most obvious solution to the diamagnetic background problem is therefore to have a sample consisting of a uniform rod of GaAs as the substrate with a region of (Ga,Mn)As at the central point. Unfortunately, standard (Ga,Mn)As samples are grown on 2 inch wafers seriously limiting the length of fabricated GaAs rods. Preliminary test measurements demonstrated that such samples were not long enough to avoid the effects of the substrate background. The fabrication of such unorthodox samples also resulted in a number of problems involving the definition and etching of the unwanted (Ga,Mn)As without significantly altering the underlying substrate thickness and roughness.

These initial tests did, however, show that the effective length of the rod could be increased by introducing further GaAs rods to each end. The gaps between rods were not apparent when making scans in the SQUID. Rods of equal width and thickness to the substrate were therefore introduced to the sample holder on either side of the existing (Ga,Mn)As chips fixed to a silicon rod. The second set of measurements performed on the original (Ga,Mn)As sample with this alternative mounting technique showed no signs of diamagnetic background.

2.3.3 Inhomogeneity

The second problem faced when conducting critical phenomena studies of (Ga,Mn)As is Curie temperature broadening related to the MBE growth process. Sample inhomogeneity was demonstrated in past (Ga,Mn)As samples by Mu Wang (Wang *et al.* (2008)). Measurements over a vast range of annealed wafers showed that T_c can change radially across a two inch wafer by as much as 3 K. This suggests a potential broadening across a standard chip of up to 0.6 K.

The sample inhomogeneity is the main reason for the difficulties in the original log-log plot method. The resulting broadening not only makes it impossible to directly read off the Curie temperature from the magnetisation data, but also distorts the expected power law behaviour. An incorrect T_c value can then be chosen which forces the behaviour to appear power law-like with erroneous critical exponents.

The effect of the broadening on Kouvel-Fisher plots is a drop-off upon approaching T_c resulting in a decrease in the calculated critical exponent. This immediately brings in to question the temperature range over which to fit. Unfortunately, the width of the critical region cannot easily be derived with different materials exhibiting different reduced temperature ranges of anything between $t = 0.01$ and $t = 0.1$. Previous Kouvel-Fisher plots of magnetisation measurements on (Ga,Mn)As samples of various manganese concentration demonstrated linear behaviour up to a reduced temperature of roughly 0.05.

The T_c broadening acts to further limit this temperature range. Temperatures close to T_c must be ignored in the Kouvel-Fisher plots in order to avoid the effects of sample inhomogeneity. Measurements therefore require a higher density of temperature points than that carried out previously in Nottingham in order to make accurate fits. The effects of sample inhomogeneity are explored in more detail in the T_c broadening section 2.5.5.

2.3.4 Practical Difficulties

Field Cooling

As well as these problems there were also a number of practical issues that first needed to be considered before finalising the experimental methods. When performing SQUID magnetometry on (Ga,Mn)As samples the application of a magnetic field is always a necessity. Even when measuring the magnetisation a field cool step is required prior to measurement.

The field cool step is required in order to saturate the sample. Whilst at the microscopic scale well below T_c the magnetic moments are aligned, samples as a whole can be composed of saturated domains that are not necessarily parallel. The application of an external magnetic field acts to align these domains.

Within the Nottingham SQUID system this external field is applied via the use of a superconducting magnet. Unfortunately, one of the results of this can be trapped flux within the coils after applying a large magnetic field. These remanent fields whilst less than 5 Oe can serious effect the magnetisation behaviour close to T_c in the critical region as well as leading to a shift in the susceptibility data. In order to minimise this effect the fields applied during the critical phenomena measurements had to be as small as possible, and yet large enough to saturate the samples. Magnetic fields of 300 Oe or less were therefore used throughout the measurements, and oscillatory demagnetisation used between samples.

Susceptibility Measurements

In addition to this minimising of the applied field, a decision also had to be made on whether to measure the sample susceptibility using either alternating current (AC) or direct current (DC) magnetometry. In DC measurements a constant magnetic field is applied producing a DC magnetisation curve $M(H)$

for each temperature. In AC magnetometry a small AC field is superimposed on top of this resulting in a time-dependent moment that allows measurement without sample motion. The advantages of this over the DC applied fields are a high sensitivity to small changes in $M(H)$ irrespective of the absolute value, and that it yields information regarding both the magnitude of the susceptibility χ and the dynamic effects within the sample.

Due to the potential additional information produced and speed of measurement, initial testing on sample Mn438_c6 was performed using AC magnetometry. Various frequencies were used to show how the AC susceptibility varied with temperature above T_c. Unfortunately, Kouvel-Fisher plots produced from these datasets resulted in calculated γ values close to 1.7 a long way from the expected Heisenberg value of 1.396. However, initial DC susceptibility data from the same sample was found to give a value almost half that of the AC test measurements demonstrating behaviour similar to that predicted by Heisenberg after diamagnetic background removal.

2.3.5 Experimental Methods

The magnetic properties of (Ga,Mn)As samples were characterised through the use of both remanent magnetisation and $M(H)$ hysteresis loop SQUID measurements using a reciprocating sample option (RSO). Samples measured were taken from wafers Mn433 and Mn438, both 25 nm thick (Ga,Mn)As grown on semi-insulating GaAs substrate, with nominal manganese concentrations of 11% and 12% respectively. These were originally prepared by scribing the wafers into 5 mm x 4 mm chips with the shorter length denoting the [110] axis. Previous magnetometry work carried out on these samples after annealing by fellow Ph.D student Mu Wang showed that they are both of high quality (high T_c) and uniaxial making them an ideal choice for the critical exponent measurements.

These original measurements were not intended for critical phenomena analysis consisting of both a high field-cool of 1000 Oe and a large temperature step size. However, rough Kouvel-Fisher plots resulted in calculated β exponents of 0.377 and 0.368; values that compare favourably with that predicted by the Heisenberg model as shown in table 2.1. The resulting intercept T_c values from these plots also acted as a guide for the critical exponent measurement ranges.

Remanence measurements were made by first field-cooling from room temperature at 300 Oe, and then measuring the sample magnetisation whilst warming in zero applied field. A temperature step size of 0.1 K was used from 10 K below the expected Curie temperature to increase the number of data points over the critical region from that of previous measurements. This data was then used to calculate the β critical exponent and an exact value for T_c via Kouvel-Fisher analysis.

Two full sets of DC $M(H)$ hysteresis loop measurements were carried out on each sample. The first sets were taken over a temperature range from the expected Curie temperature up to 10 K above at intervals of 0.5 K. These were then used to calculate the susceptibility as a function of temperature by averaging both the up and down sweeps, and linearly fitting around $H = 0$. Both fit and sweep range of each measurement were increased with temperature with a maximum sweep range of ±200 Oe from roughly 5 K above T_c. The susceptibility data was then used to calculate both a comparison T_c value and the γ critical exponent.

The second sets of loop measurements were taken at temperatures both above and below the expected T_c over a range of ±3 K and a magnetic field of ±20 Oe. In this case rather than using a constant temperature step size, hysteresis loops were taken at ever smaller intervals down to 0.1 K upon approaching the expected Curie temperature predicted by the remanence data. These $M(H)$ loops were used to produce modified- and standard-Arrott plots with the Heisenberg and mean-field exponent values respectively. Linear fitting to each of the isotherms was then used to calculate a value of T_c for both models. These second sets of $M(H)$ loops were then also used to produce an estimate for the δ critical exponent at the calculated Curie temperature to make a comparison to that predicted by the Widom function (2.2.17).

Two sets of each of these measurements were performed on sample Mn438_c6. The first using a conventional silver wire and GE varnish mounting technique, and the second on silicon with the addition of GaAs rods either side. This chapter presents these measurements as the averages of each respective datasets with the conventionally mounted susceptibility and Arrott data having been corrected for diamagnetic background as detailed in section 2.3.2. Only a single set of measurements were made on sample Mn433_c using the GaAs rod mounting method.

2.4 Previous Work

A number of studies in the past have focused on the behaviour of the magnetic or transport properties of (Ga,Mn)As close to the Curie temperature (van Esch *et al.* (1997); Matsukura *et al.* (1998); Jiang *et al.* (2009)). However, whilst theories about the behaviour and expected universality class (Kuivalainen (2001); Brey and Gómez-Santos (2003); Moca *et al.* (2009); Priour and Das Sarma (2010)) have been put forward, the search for an absolute description of the critical contribution still remains an open problem within the field.

Experimental measurements concentrated purely on the critical behaviour have been relatively limited (Novák *et al.* (2008); Khazen *et al.* (2010); Yuldashev *et al.* (2011)) with no definite conclusions drawn about whether the observed behaviours follow the expected Heisenberg model. This is due in part to the associated difficulties detailed within this chapter, but also the need for rather subtle, high-resolution measurements very close to T_c because of the relative close proximities of the mean-field and Ising values.

This is especially true of the β exponent with Novák *et al.* (2008) estimating the value to be somewhere between 0.3 and 0.4. This range comfortably covers both the Ising and Heisenberg critical exponents, but is based solely on standard magnetisation measurements with the paper stating the need for a much more in-depth study of the critical region in order to perform accurate calculations of the exponent.

A much more exact figure of $\beta = 0.407(5)$ is given by Khazen *et al.* (2010), a value slightly higher than that predicted by the Heisenberg model, but still appreciably lower than the mean-field value. However, this value is calculated via the log-log fitting method over a much larger reduced temperature range than that of the expected critical region, and on datasets with step-sizes close to 5 K. Assuming a reduced temperature critical region of 0.1 such a large step-size results in only two data points within the required range. By comparison the magnetisation measurements presented in this chapter have step-sizes of only 0.1 K close to T_c.

The paper cites a number of possible explanations for this apparent disparity with the Heisenberg model including referencing the single cluster defect model proposed by Muller-Krumbhaar (1976). Comparisons are also made to past amorphous ferromagnet studies many of which showed calculated exponent values close to 0.4. However, analysis of past sample datasets from Nottingham with similarly large step-sizes demonstrates that such values are only valid when fitting over larger temperature ranges outside the critical region. A summary of this analysis is presented in section 2.5.6.

2.5 Results

2.5.1 Remanent Magnetisation

Figure 2.5.1 shows remanent magnetisation data from both Mn438_c6 sets of measurements. Whilst the remanence and β calculation are not significantly affected by the diamagnetic background the measurements performed using the rod mounting technique serve to show that this method can cause further problems to be noted for future magnetometry.

The difference seen below T_c is most likely caused by a slight, unavoidable misalignment of the sample; one of the reasons why these measurements are usually performed together without removing the sample from the SQUID. The remanence of ~ $0.4\,\mathrm{emu\,cm^{-3}}$ above T_c is more difficult to explain, but could be due to unwanted impurities on the GaAs surface or silicon mounting rod. Despite these potential problems the 300 Oe field cooled datasets shown in figure 2.5.2 demonstrate that the introduction of the GaAs does dramatically reduce the effects of the substrate background.

Kouvel-Fisher analysis on earlier Mn438_c6 datasets with similarly small temperature step sizes resulted in noticeable oscillations in the plot making accurate linear fitting very difficult. The cause of this behaviour was found to be the numerical derivative which emphasises any noise in the data leading to

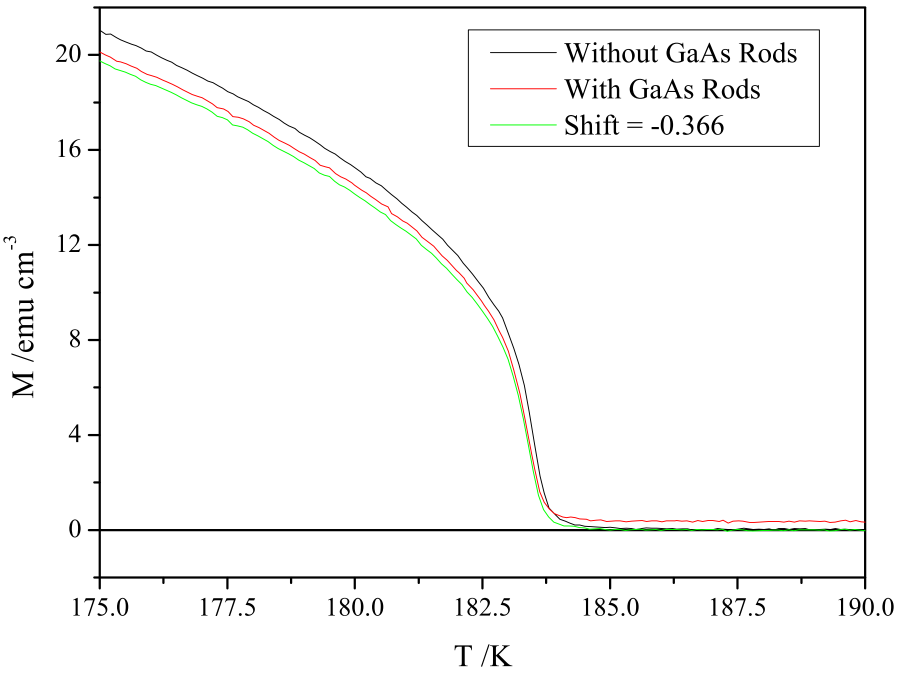

Figure 2.5.1: Remanent magnetisation data both with (red) and without (black) GaAs rods for sample Mn438_c6. The green plot shows the GaAs rods data shifted by -0.366 emu cm^{-3} calculated from the non-zero magnetisation above T_c.

pronounced unwanted fluctuations. Test measurements were performed prior to that shown in order to optimise both the temperature sweep rate and data step size.

In order to remove these unwanted fluctuations both interpolation and nearest neighbour adjacent averaging were carried out before differentiation, and then Fourier filtering used at lower temperatures to remove or reduce any remaining periodic noise. The final Kouvel-Fisher plots of the average of both Mn438_c6 datasets, and the single Mn433_c dataset are shown in figures 2.5.3a and 2.5.3b respectively. Figure 2.5.3c then shows a comparison between these plots for both samples shifted by their calculated T_c values.

Linear fitting on the non-shifted plots was performed over the same reduced temperature ranges avoiding both the noisier data at lower temperatures and the observed drop-off close to T_c. These apparent drop-offs in $-M/\frac{\mathrm{d}M}{\mathrm{d}T}$ and

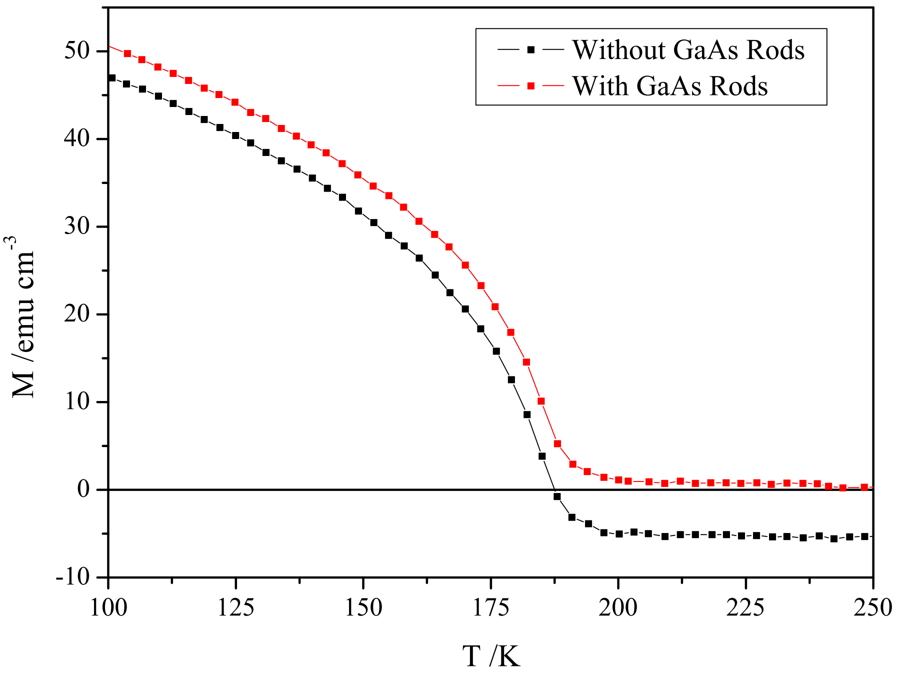

Figure 2.5.2: Field-cool data at 300 Oe for sample Mn438_c6 both with (red) and without (black) GaAs rods. The negative shift in the black plot is the result of the substrate diamagnetic background. This is almost completely removed once the GaAs rods have been added with only a slight moment above T_c in the red plot.

associated rise in calculated β exponent just below T_c are the result of sample inhomogeneity covered in sections 2.3.3 and 2.5.5. The calculated results of $\beta_{\mathrm{Mn438}} = 0.365$ and $\beta_{\mathrm{Mn433}} = 0.368$ are very close to that predicted by the Heisenberg model.

Larger step size magnetisation measurements were also performed on both samples down to 20 K. Kouvel-Fisher analysis on this data revealed linear behaviour not just close to T_c, but also below the critical region as shown by figure 2.5.4. Fitting to these datasets resulted in calculated exponents of roughly 0.4 in both samples down to 100 K; a value very similar to that found by Khazen *et al.* (2010). Analogous plots for the previously measured samples shown in section 2.5.6 revealed very similar behaviour over a wide range of manganese concentrations.

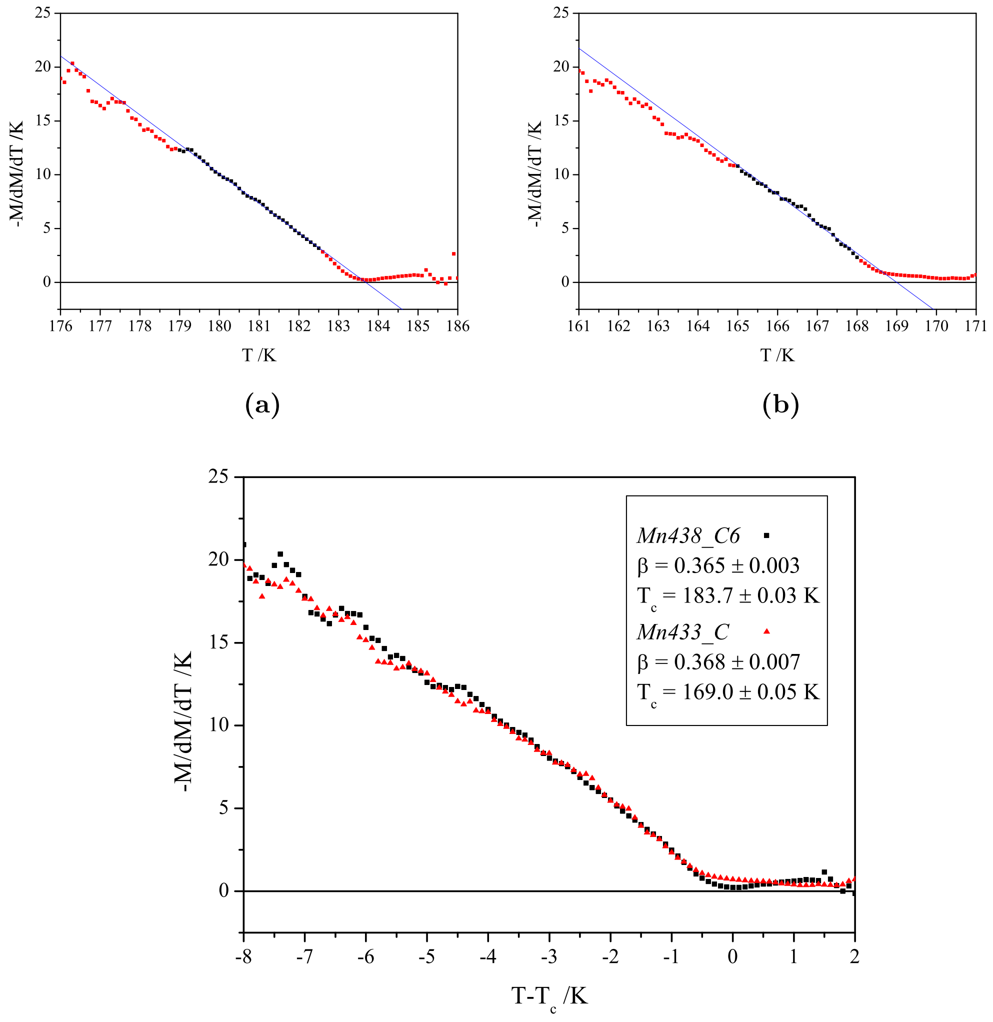

(a) **(b)**

(c)

Figure 2.5.3: Kouvel-Fisher plots of the averaged interpolated remanence from samples Mn438_c6 (a) and Mn433_c (b). Numerical differentiation was carried out using nearest neighbour least-squares smoothing to reduce the amplification of noise. Graph (c) then shows both of the Kouvel-Fisher plots shifted by their respective calculated T_c values.

Below this temperature range the Kouvel-Fisher plots then becomes non-linear with exponential growth down to 20 K. At such temperatures the effects of spin-wave excitations are expected to dominate following Bloch's law (2.2.8) as covered in section 2.2.1. Figure 2.5.5 shows $\log(1 - \frac{M}{M_0})$-$\log(T)$ graphs of both the Mn438_c6 and Mn433_c magnetisation datasets used to plot 2.5.4. Linear

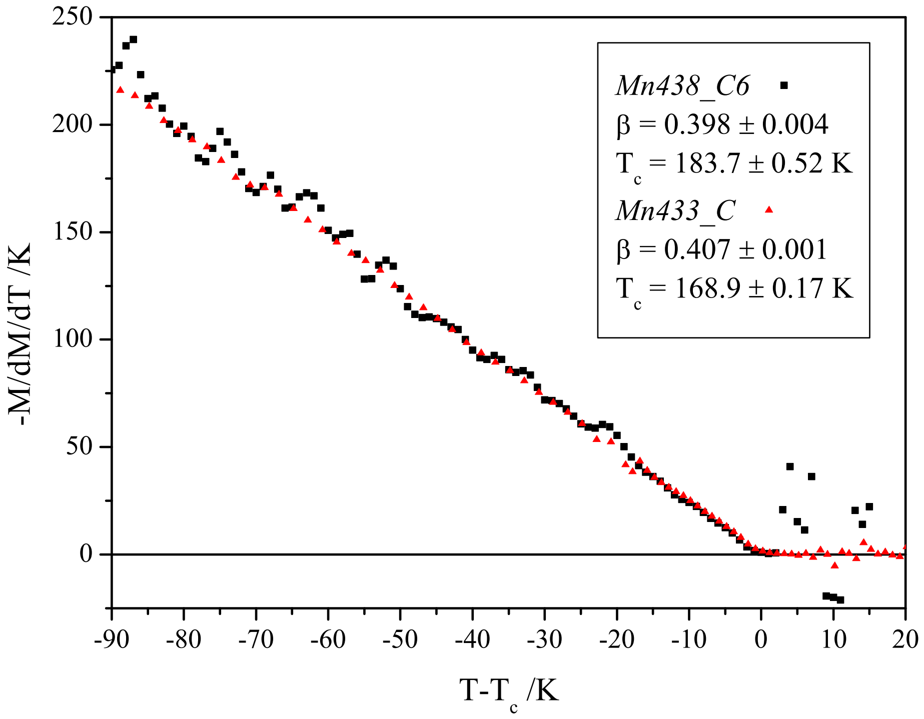

Figure 2.5.4: Shifted Kouvel-Fisher plots of larger step-size remanent magnetisation data for samples Mn438_c6 and Mn433_c. Linear fitting was performed from 100 K up to just below the respective critical regions shown in 2.5.3a and 2.5.3b. The calculated exponent values are found to be very close to that of a wide range of previously measured (Ga,Mn)As samples over the same reduced temperature range.

fitting between 20 K and 100 K resulted in power-law exponents approaching that of the Bloch $T^{3/2}$ law.

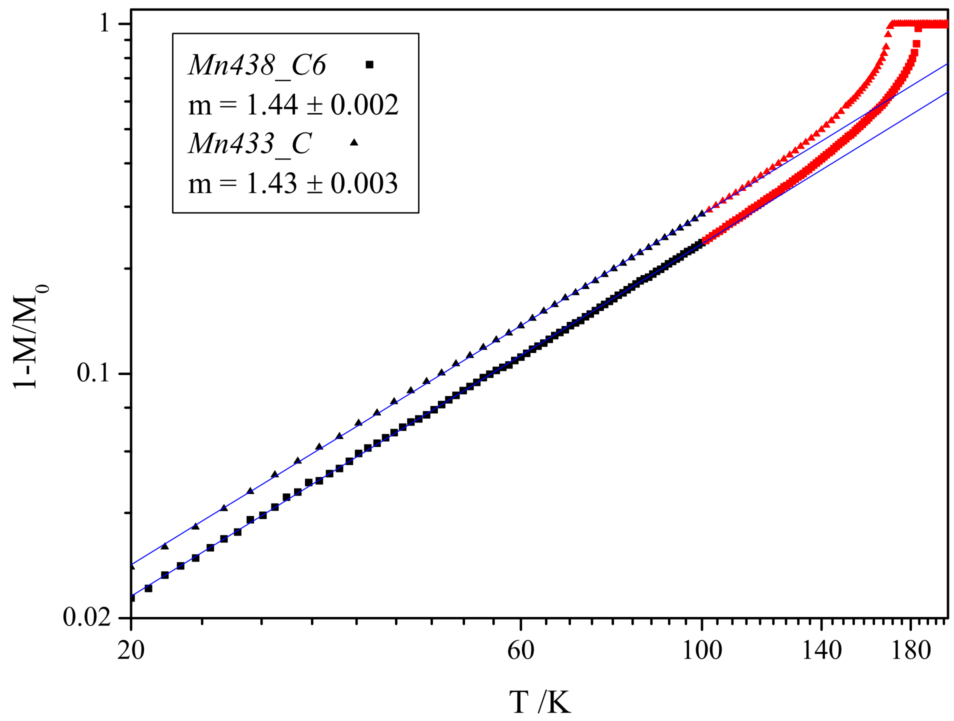

Figure 2.5.5: Logarithmic plots of $\frac{\Delta M}{M_0}$ against T for both Mn438_c6 (■) and Mn433_c (▲). The calculated power law exponents of 1.44 and 1.43 are comparable to that predicted by Bloch's law of magnons.

2.5.2 Susceptibility

Figure 2.5.6 shows both susceptibility datasets for sample Mn438_c6 with the standard silver wire mounting method data becoming negative above 188 K due to the substrate diamagnetic background contribution. The adjustment of 2.1x10^{-2} emu cm^{-3} Oe^{-1} to this data was calculated by the fitting of a shifted power-law as described in section 2.3.2. This corrected data closely matches that of the GaAs rod measurements especially at higher temperatures away from the effects of T_c broadening.

Kouvel-Fisher analysis was carried out on the average of the Mn438_c6 datasets shown in figure 2.5.6, as well as the single set of Mn433_c data. Plots are shown in figures 2.5.7a and 2.5.7b respectively. Linear fitting close to T_c reveals similar γ values close to that predicted by the Heisenberg model. However, whereas the Mn433_c plot appears to show linear behaviour of constant gradient over the full measured temperature range the Mn438_c6 γ-Kouvel-Fisher seems to

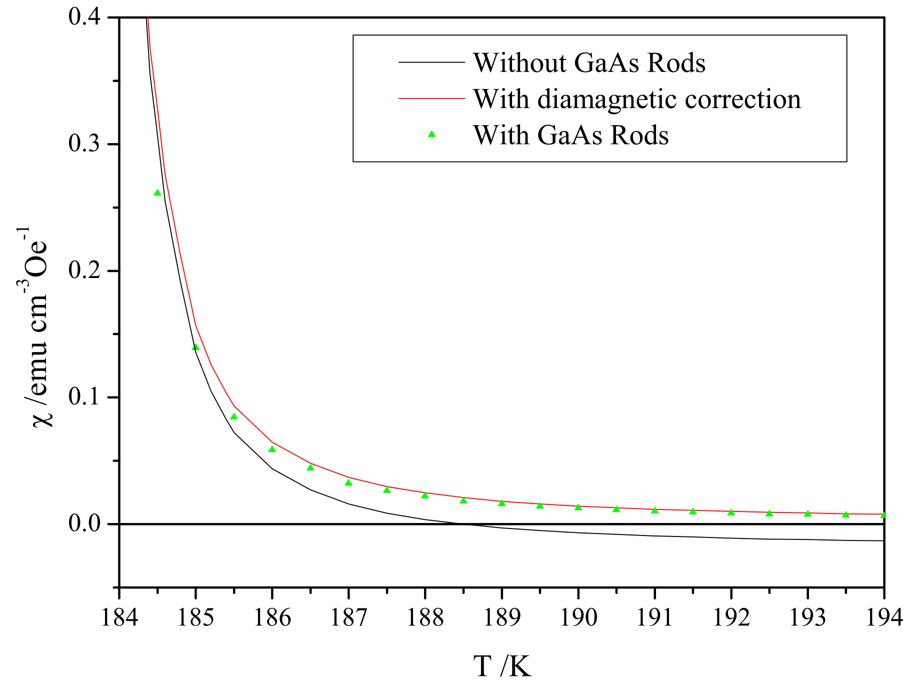

Figure 2.5.6: Mn438_c6 susceptibility data calculated from the low-field gradient of DC $M(H)$ loops. The black plot shows the susceptibility calculated from the measurements performed without the GaAs rods. The red plot then shows the black plot shifted by 2.1x10^{-2} emu cm^{-3} Oe^{-1} to correct for the substrate diamagnetic background. This is comparable to that calculated from the measurements performed with the GaAs rods shown by the green points.

have a change in gradient, and thus calculated γ, roughly 5 K above T_c.

This change in gradient could indicate a transition away from the Heisenberg critical behaviour similar to that observed in the remanence. Fitting to both sections in figure 2.5.7a revealed a change in γ towards that predicted by the mean-field model (γ_{MF} = 1). Unfortunately, unlike the magnetisation data this change in behaviour cannot be verified at higher temperatures due to the resolution of the SQUID; as the susceptibility approaches zero an increasing level of oscillatory noise is observed in the Kouvel-Fisher plot. An alternative reason for the apparent differences between samples could therefore simply be that this noise is distorting the underlying behaviour more than 5 K above T_c. Kouvel-Fisher plots of the separate Mn438_c6 datasets showed that the

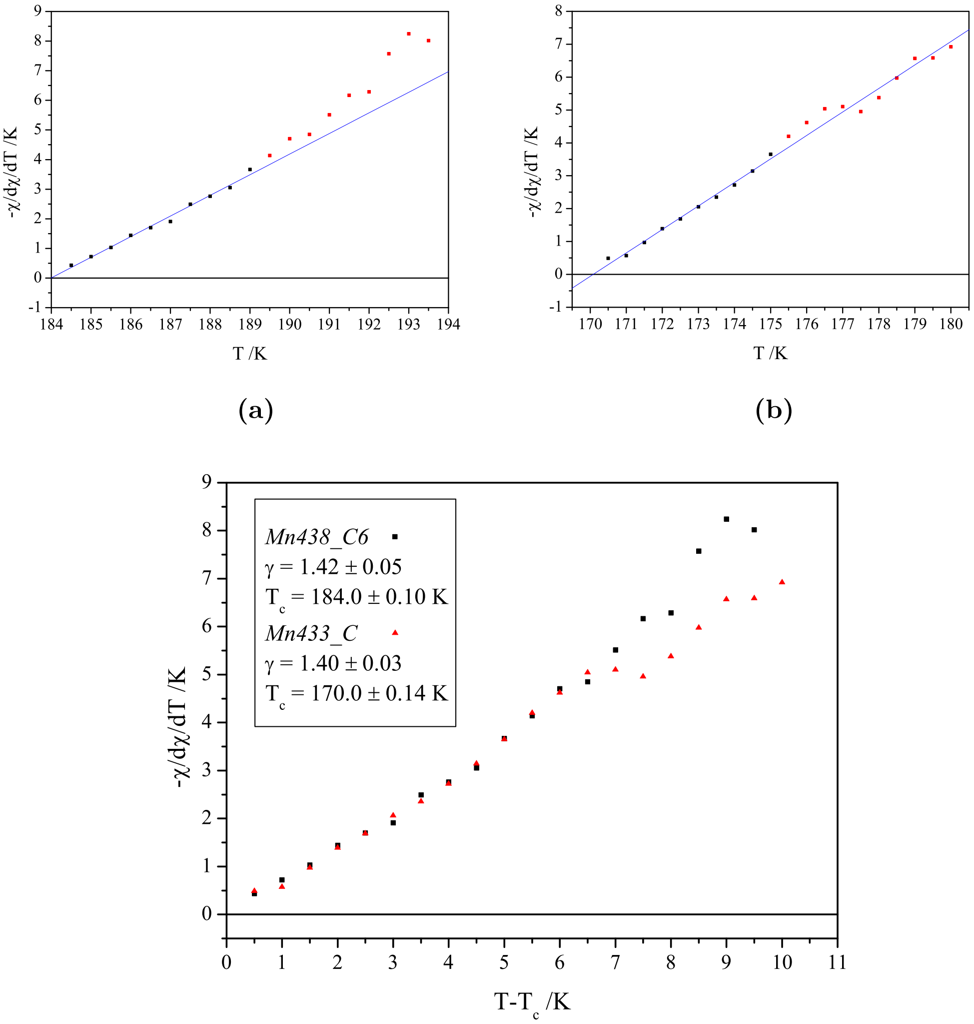

(a) **(b)**

(c)

Figure 2.5.7: Kouvel-Fisher plots of the DC susceptibility from samples Mn438_c6 (a) and Mn433_c (b). Graph (c) shows both these plots shifted by their respective calculated T_c values.

non-GaAs rod measurements accounted for most of the apparent change in gradient suggesting the noise to be the more likely source.

2.5.3 Modified-Arrott Plots

Figures 2.5.8 and 2.5.9 show both the standard mean-field Arrott and Heisenberg modified-Arrott plots for Mn438_c6 and Mn433_c respectively. These were produced by averaging the up and down sweeps and then plotting $|M|^{1/\beta}$ against $\left(\frac{H}{M}\right)^{1/\gamma}$ resulting in two parallel sections for each temperature originating from the positive and negative field regions of each loop. These were then averaged to produce a single Arrott plot for each temperature.

The Curie temperatures were calculated from both sets of plots by performing a linear fit to each isotherm and plotting the resulting y-intercepts against temperature. In both cases the mean-field intercept plot showed a change in gradient roughly 1 K below the expected Curie temperature. One possible reason for this could be the higher associated errors in the fitting due to the noticeably less linear behaviour compared to that of the Heisenberg plots. The T_c values from the standard Arrott plots were calculated from the 1 K fitting range close to the Curie temperature with fitting over the lower range resulting in calculated values roughly 0.5 K higher.

The modified-Arrott intercept plots showed no change in gradient below the expected Curie temperatures, but non-linear above them. Equation (2.3.2) shows that the modified-Arrott plots are only valid up until roughly the expected T_c values above which the inequality is not satisfied at low magnetic fields. The sample T_c values shown in figures 2.5.8a and 2.5.9a were therefore calculated by fitting to the linear regions below the expected Curie temperatures.

The resulting T_c values of 183.5 K and 169.1 K from the Heisenberg plots compare favourably to the corresponding β-Kouvel-Fisher values of 183.7 K and 169.0 K. The mean-field Arrott plots produce a calculated value only slightly higher that is still well within the expected T_c broadening demonstrated in section 2.5.5. However, the difficulties in fitting to these over the modified-Arrott plots due to both non-linear and non-parallel behaviour demonstrates the potential importance of the correct choice of universality class and fitting range when making use of Arrott plots.

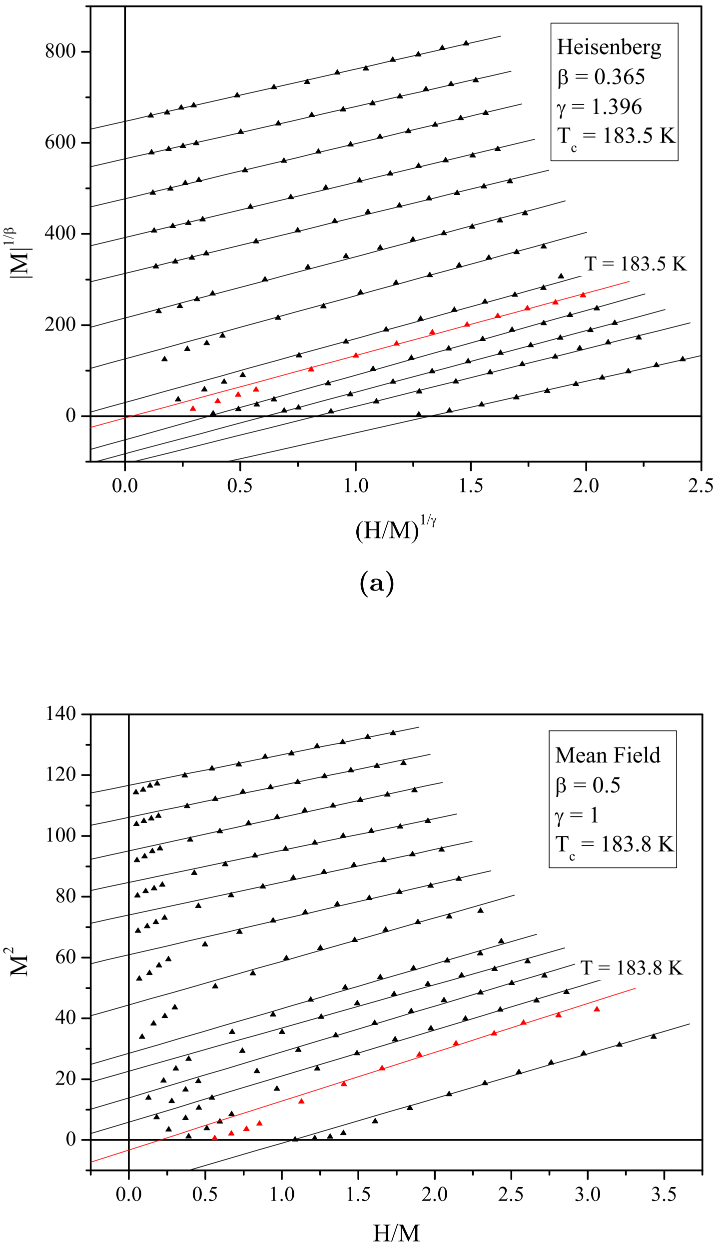

(a)

(b)

Figure 2.5.8: Heisenberg modified-Arrott (a) and standard mean-field Arrott (b) plots for sample Mn438_c6 close to the calculated T_c values of 183.5 K and 183.8 K respectively. Measurements performed without the GaAs rod mounting had a constant diamagnetic background of $-2.1\text{x}10^{-2}$ emu cm^{-3} Oe^{-1} removed prior to analysis.

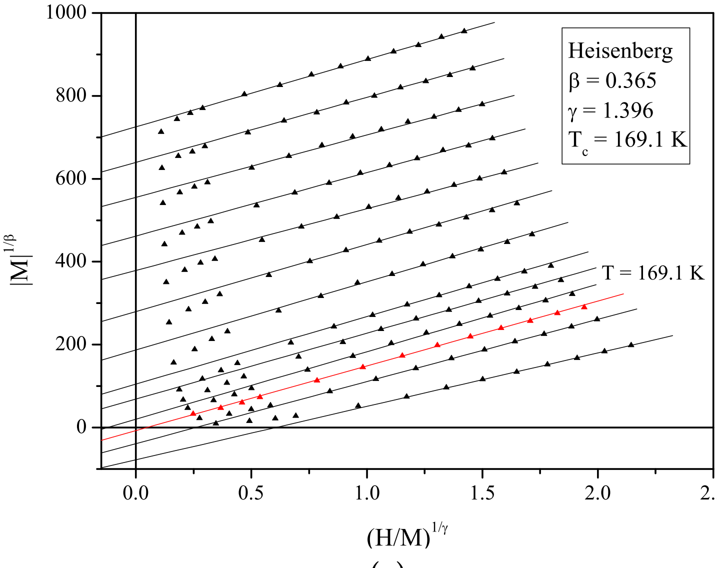

(a)

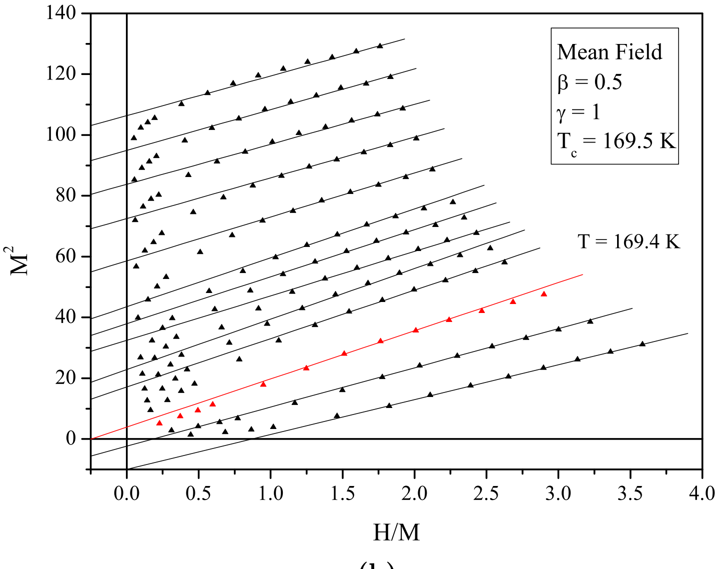

(b)

Figure 2.5.9: Heisenberg modified-Arrott (a) and standard mean-field Arrott (b) plots for sample Mn433_c close to the calculated T_c values of 169.1 K and 169.5 K respectively. In the case of the mean-field plots a 169.5 K isotherm was not measured due to this being 0.5 K away from the expected T_c value taken from the magnetisation. At this temperature measurements were performed in 0.2 K steps.

2.5.4 Consistent Fitting

Both remanent magnetisation and susceptibility data from sample Mn438_c6 show a T_c value variation of only 0.3 K, thus one possibility for a more accurate fit is to force both values to be equal by performing a consistent fit. Consistent fitting across both datasets was carried out by multiplying the γ-Kouvel-Fisher data by a constant $C = \frac{\gamma}{\beta}$ and fitting over a wide range of C values to find that with the highest correlation coefficient. The $M(H)$ data originally used to make both the standard and modified-Arrott plots in figure 2.5.8 was then used to make a third plot to test the T_c self-consistency using the Widom function:

$$\gamma = \beta\,(\delta - 1) \tag{2.5.1}$$

$$\therefore \quad \delta = 1 + \frac{\gamma}{\beta} = 1 + C \tag{2.5.2}$$

This can be combined with the $\frac{1}{\delta}$-scaling of M and H such that

$$\left(\frac{\mathrm{d}\log(M)}{\mathrm{d}\log(H)}\right)^{-1} - C + 1 \tag{2.5.3}$$

should equal zero at T_c, and thus if consistent cross with the intercept of the β and γ fits.

The highest fitting correlation coefficient occurred at $C = 4.00$ resulting in a calculated value of $\delta = 5.00$ at $T = 183.8$ K. However, as is shown in figure 2.5.10, this calculated value of T_c does not match that of the shifted δ plot which crosses zero at $T \approx 183.4$ K. The calculated value of δ from this plot at $T = 183.8$ K was only 1.35, much lower than that predicted by the Heisenberg model. This difference in T_c could again be linked to a broadening across the sample: the calculated β and γ values were noticeably further from the predicted values than that when performing separate fits.

Due to this problem appearing even more pronounced in Mn433_c between both the Kouvel-Fisher plots, full consistent fitting was not carried out for this sample. Figure 2.5.11 does, however, show the separate components of the plot without consistent β and γ fitting. It is clear from this graph that

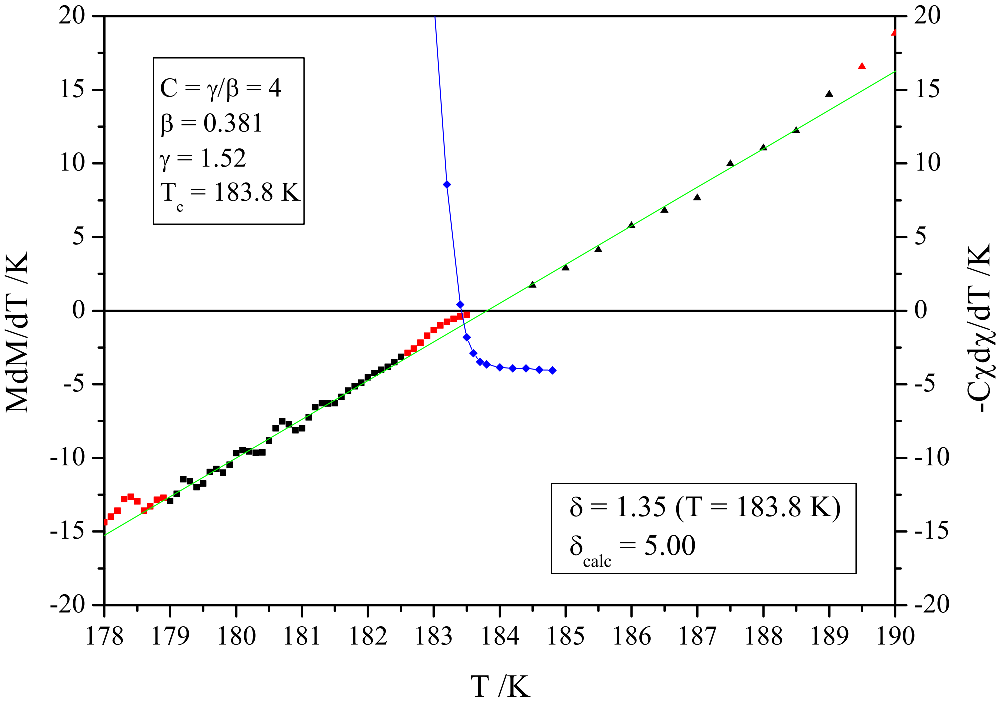

Figure 2.5.10: An averaged consistent fit plot for sample Mn438_c6 in which MatLab was used to linearly fit over a $C = \gamma/\beta$ range of 3 to 5 in 0.01 increments. Black points represent the fitting range over both the β- (■) and γ- (▲) Kouvel-Fisher plots, and the blue points the shifted δ curve.

both Kouvel-Fisher plots are not consistent even when varying the fit range. However, unlike Mn438_c6 the shifted δ plot is consistent with T_β with a calculated value of 5.08 at 169.0 K.

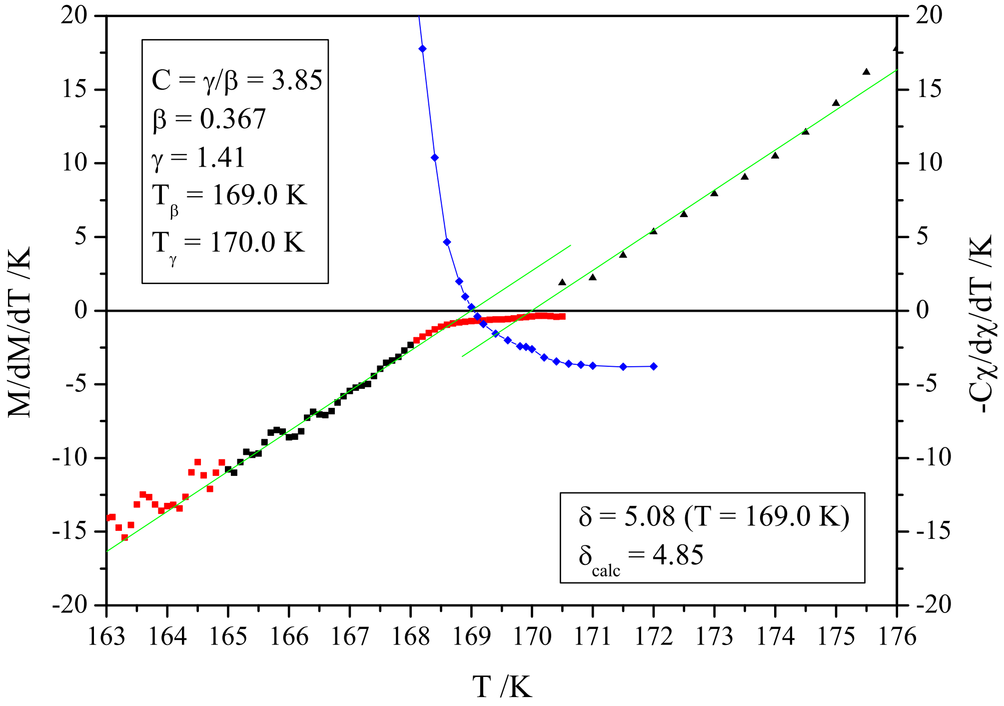

Figure 2.5.11: A consistent plot for sample Mn433_c in which both β and γ fits are separate as shown in figures 2.5.3b (■) and 2.5.7b (▲), and the δ plot calculated from the Arrott data.

2.5.5 Curie Temperature Broadening

Calculated T_c values can be seen to differ for both samples between the β-Kouvel-Fisher plots (2.5.3), γ-Kouvel-Fisher plots (2.5.7), and the modified-Arrott plots (2.5.8a, 2.5.9a). One possible reason for this variation is sample inhomogeneity as covered in section 2.3.3.

The effects of broadening within the magnetisation plots were modelled via a program written by Prof. Kevin Edmonds using a Gaussian distribution of T_c across the sample taking a similar method to that of Kuz'Min and Tishin (2006). Equations (2.5.4) and (2.5.5) show the standard Gaussian distribution and the broadened T_c integral used to model the magnetisation.

$$P(T_\mathrm{c}) = \frac{1}{\sqrt{2\pi}\Delta} \exp\left(-\frac{(T_\mathrm{c} - T_\mathrm{c0})^2}{2\Delta^2}\right) \tag{2.5.4}$$

$$M = \frac{M_0}{\sqrt{2\pi}\Delta} \int \left(1 - \frac{T}{T_\mathrm{c}}\right)^\beta \exp\left(-\frac{(T_\mathrm{c} - T_\mathrm{c0})^2}{2\Delta^2}\right) \mathrm{d}T_\mathrm{c} \tag{2.5.5}$$

Modelling was carried out using a mean value of $T_\mathrm{c0} = 180\,\mathrm{K}$ and exponent equal to that of the Heisenberg model. Plots of the magnetisation using Δ values of 0.125 K, 0.25 K, 0.5 K and 1.5 K showed a steady smoothing around the critical region with larger widths leading to an increasing non-zero tail above T_c0 similar to that observed in past samples with low T_c values. Figure 2.5.12 shows how both the $\Delta = 0.5\,\mathrm{K}$ and $\Delta = 1.5\,\mathrm{K}$ Gaussian broadened magnetisations compare to the theoretical Heisenberg functional form close to T_c.

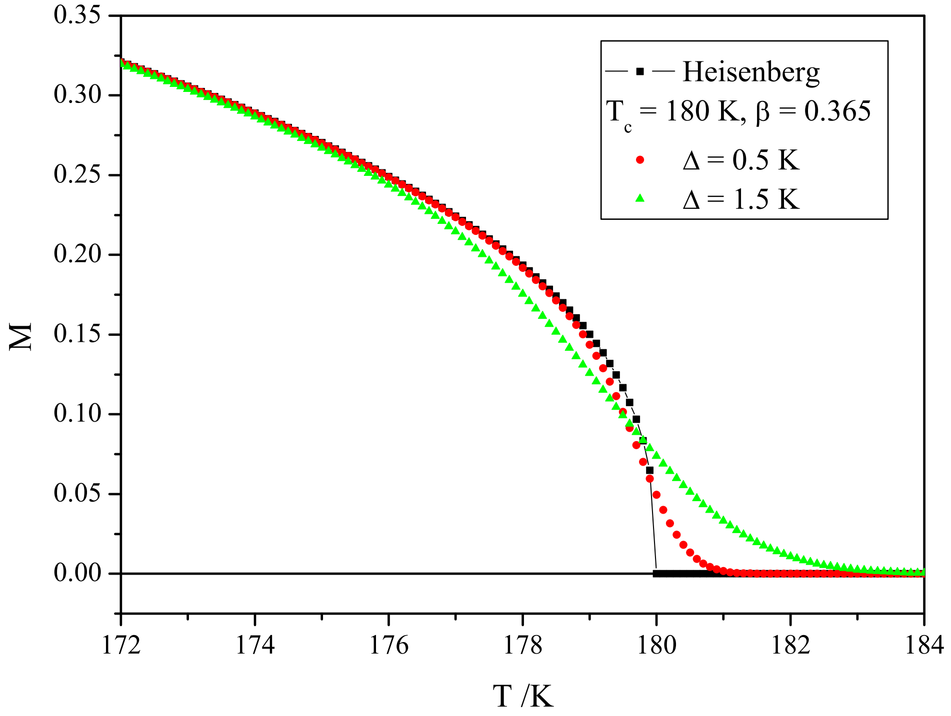

Figure 2.5.12: The standard Heisenberg model magnetisation (black) using a constant of proportionality of $M_0 = 1$, and the Gaussian broadened plots with Δ values of 0.5 K (red) and 1.5 K (green).

Kouvel-Fisher plots of these modelled magnetisation curves show a drop off upon approaching T_{c0} that occurs at ever lower temperatures as the Gaussian width is increased. The 0.125 K and 0.25 K plots showed only a very slight drop off only apparent ~1 K below T_{c0}. However, the 0.5 K and 1.5 K plots demonstrate appreciably different behaviour over the whole fitting range resulting in a change in both calculated β and T_c as shown in figure 2.5.13.

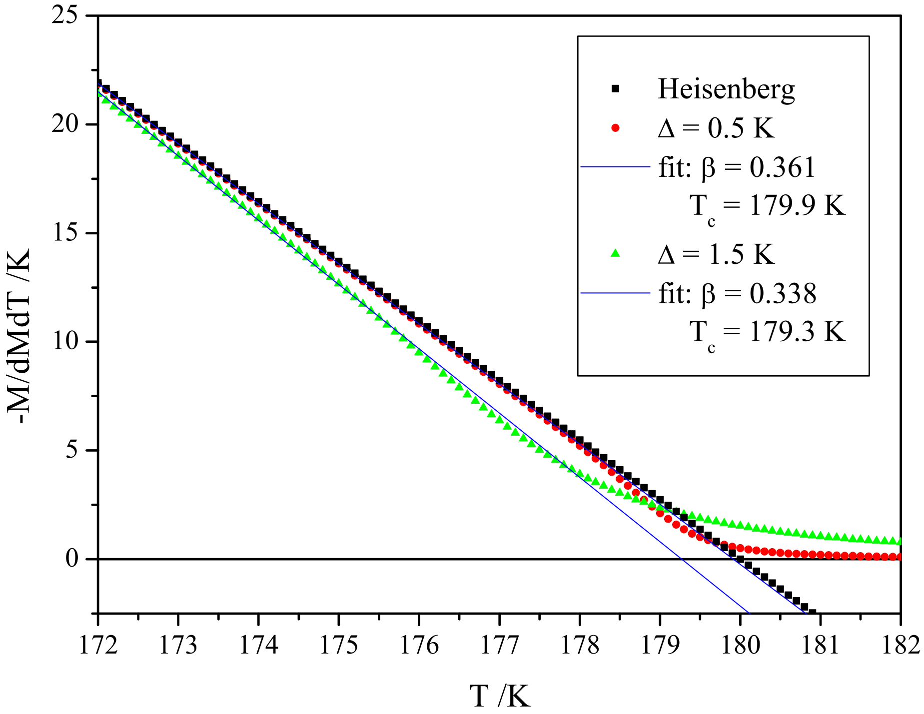

Figure 2.5.13: Kouvel-Fisher plots of the Gaussian broadened magnetisation using a central T_c value of 180 K and Δ values of 0.5 K and 1.5 K.

The 1.5 K plot shows non-linear behaviour up to 5 K below T_{c0}, and a non-Heisenberg gradient down to 160 K. Fitting over the expected critical region below the non-linear range results in a reduced exponent close to that of the 3D-Ising model. Such a dramatic change in the magnetisation close to T_c illustrates the importance of highly homogeneous samples when studying critical phenomena. Samples Mn438_c6 and Mn433_c demonstrate behaviour much closer to that of the 0.5 K plot with a much smaller drop off. However, what is clear from this plot is that a slight broadening can still result in a reduction in the calculated β and T_c values even when avoiding the non-linear range close to T_c.

The calculated drop of 0.1 K goes someway to explaining the difference in calculated T_c between the Kouvel-Fisher plots for Mn438_c6, but not the 1 K difference observed in sample Mn433_c. With this in mind the second stage of the T_c broadening was to model the effect on susceptibility. Unfortunately, in this case the Gaussian broadening method cannot be applied because the susceptibility is theoretically infinite at the Curie temperature.

The method used as an estimate for the susceptibility data was to replace the probability distribution with two single temperature points of equal contribution: $(T_c + \Delta)$ and $(T_c - \Delta)$. Plots of susceptibility were made using a central T_c of 180 K and Δ values the same as that used for the magnetisation. The effects of this broadening were much more pronounced for the susceptibility than that of the magnetisation with a large shift from the expected Heisenberg behaviour just above 180 K resulting in a larger change in the calculated T_c values. Figure 2.5.14 shows both the 0.5 K and 1.5 K broadened susceptibility plots compared to the ideal Heisenberg power law close to T_c.

Kouvel-Fisher plots for both the Δ = 0.5 K and 1.5 K models are shown in figure 2.5.15. The effect of the two point model is a drop off in the Kouvel-Fisher approaching T_c similar to that of the Gaussian broadened magnetisation. However, unlike the magnetisation plots this behaviour is not observed in either of the sample susceptibility datasets. Both γ-Kouvel-Fisher plots shown in figure 2.5.7c resulted in calculated exponents very slightly above the Heisenberg value with no noticeable drop-off in the graphs upon approaching T_c.

One possible reason for this difference could be the numerical differentiation which causes a slight turn up of the plot at each end. Within the β analysis this had very little effect on the final fitting due to the small 0.05 K data step-size and the measured temperature range extending well above the critical region. However, in the case of the susceptibility datasets the step-size is much larger at 0.5 K with the measured range only beginning at T_c. Within both γ-Kouvel-Fisher plots this first data point showed a significant rise away from the more linear behaviour at higher temperatures. These were therefore not shown in figures 2.5.7a and 2.5.7b.

Comparisons of the magnetisation datasets to the Gaussian model, and to Mu

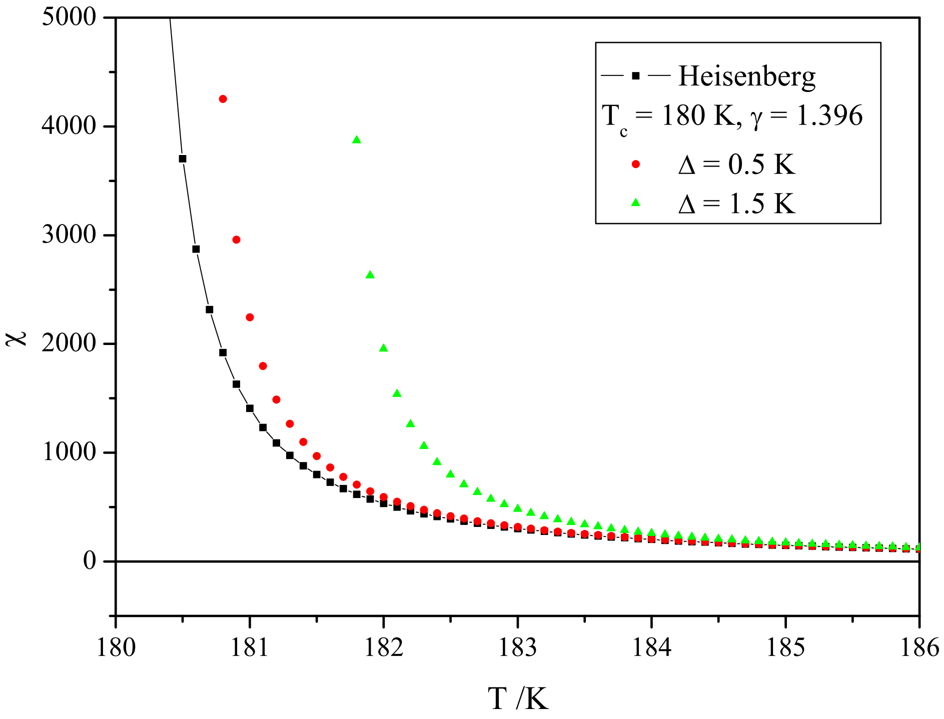

Figure 2.5.14: The standard Heisenberg model susceptibility (black) using a constant of proportionality of $\chi_0 = 1$, and the two-point broadened plots with $\Delta = 0.5\,\mathrm{K}$ (red) and 1.5 K (green).

Wang's past work, suggest a T_c broadening of ~ 1 K across a standard high quality sample. Such broadening could account for most of the disagreements seen between both sets of Kouvel-Fisher analysis and the modified-Arrott plots with shifts in the calculated T_c expected to be roughly 0.2 K in each direction. However, this broadening behaviour does not explain the 1 K inconsistency between the Kouvel-Fisher plots of sample Mn433_c.

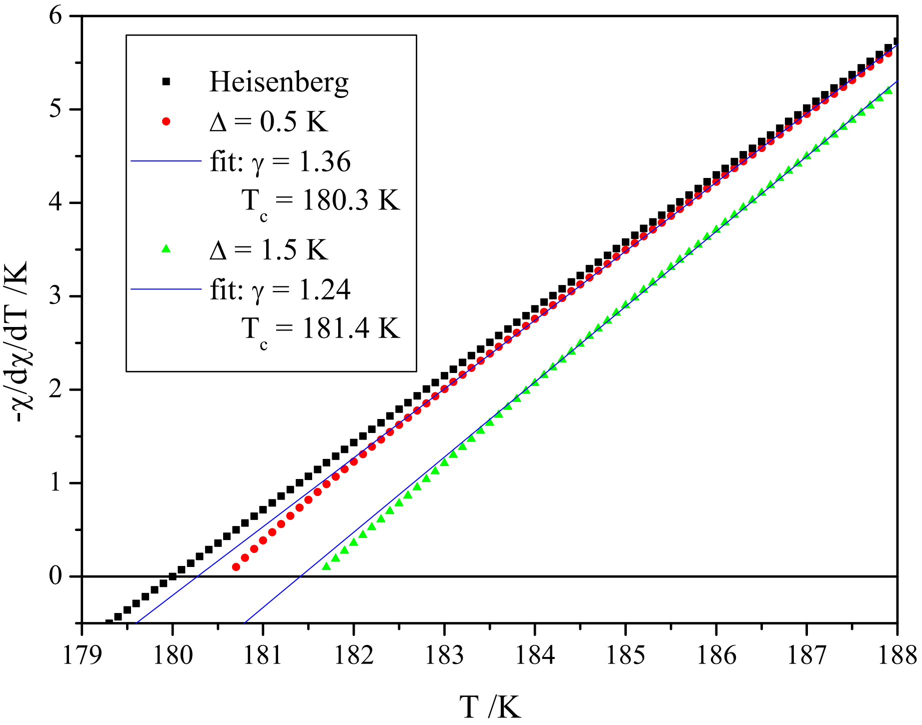

Figure 2.5.15: Kouvel-Fisher plots of the two-point broadened susceptibility using a central T_c value of 180 K.

2.5.6 Past Samples

Having shown that both high T_c samples Mn438_c6 and Mn433_c demonstrate behaviour very similar to that predicted by the Heisenberg model the next step was to confirm this across a much broader spectrum of samples. Kouvel-Fisher analysis was carried out on roughly forty datasets from past remanent magnetisation measurements on annealed samples of various Mn concentration and thickness. All measurements were originally performed as part of sample and wafer characterisation by members of the Nottingham group using 1000 Oe field cools and varying step-sizes much larger than that of the work on Mn438_c6 and Mn433_c. These datasets are therefore not suitable for high quality analysis only as a general confirmation of the Heisenberg behaviour. Figure 2.5.16 shows four examples of the β-Kouvel-Fisher analysis of such samples.

The first, sample Mn439_A, was taken from a (Ga,Mn)As wafer nominally the same as that of Mn438_c6 with a similarly high T_c. The graph for this

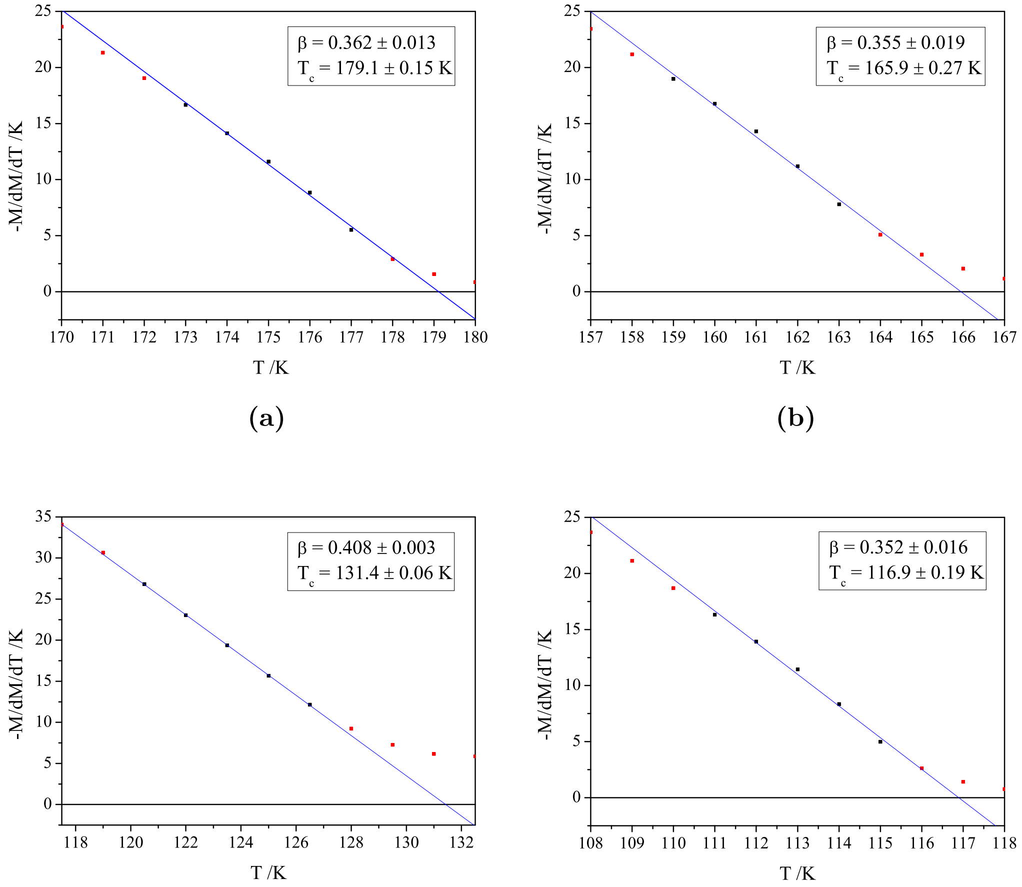

(a) (b)

(c) (d)

Figure 2.5.16: Remanent magnetisation Kouvel-Fisher plots for samples (a) Mn439_A (12%, 25 nm), (b) Mn604 rod (12%, 25 nm), (c) Mn296 (8%, 25 nm) and (d) Mn330 (6%, 25 nm).

sample serves to show the large temperature step sizes used in most of the past measurements, and their effects on the Kouvel-Fisher analysis. A general smoothing of the graph is seen with no oscillatory behaviour; however, because of this the unwanted effects of T_c broadening are much less apparent and thus more difficult to avoid. Despite this problem fitting over a range consistent to that previously used does result in a calculated β very close to that of the Heisenberg model.

Similar behaviour is then also seen in graph (b) for sample Mn604, again a high T_c and Mn concentration sample. However, unlike the other samples shown, measurements on Mn604 were carried out during the testing of GaAs rods.

Rather than being a standard 5 mm x 4 mm chip this was fabricated as part of a 60 mm long GaAs rod; the results suggest that this could be another future possibility for dielectric background removal given further optimisation.

The final two plots (c) and (d) are taken from lower Mn concentration samples. In such cases accurate fitting is more difficult because the critical phenomena temperature range scales with sample T_c. Sample Mn296 is a typical example of this problem in which the 2 K step size results in a range containing only two points, fitting was therefore performed over a larger range yielding a β value of 0.408. This closely matches the behaviour seen in Mn438_c6 and Mn433_c at temperatures below the critical region, and is also seen in most of the other past dataset samples.

Such a value calculated for Mn296 suggests that the transition to the Heisenberg behaviour is too close to the effects of T_c broadening resulting in a merged curve that cannot be fitted to with the larger step size data. Mn330 is a similar sample in which the smaller 1 K step size means that a more reasonable range can be chosen. The result is a slightly low calculated exponent with a relatively large associated error due to broadening drop-off.

Calculated β values for the past datasets were plotted as a histogram as shown in figure 2.5.17. Samples that produced non-linear Kouvel-Fisher plots caused by high field cooling or a large T_c broadening were not included. Such samples generally resulted in a smooth curve over the critical region, or a very noisy plot such as that seen in very early Mn438_c6 test measurements. Samples with a low thickness (<10 nm) and Mn concentration with a T_c below 100 K resulted in non-linear plots that when fitted to over the required temperature range resulted in calculated values of less than 0.3. Fitting to these samples over a larger range below the critical region usually resulted in calculated exponents close to 0.4.

Generally samples with a high Mn concentration and a T_c above 170 K resulted in calculated values close to or just below that predicted by Heisenberg as shown by the first peak in 2.5.17. The average β exponent of 0.357 was calculated by fitting a normal distribution excluding the β counts at the 0.4 peak associated with the problems with large step size fitting as seen in 2.5.16c. Such a slight drop in the average β in comparison to the Heisenberg value closely matches

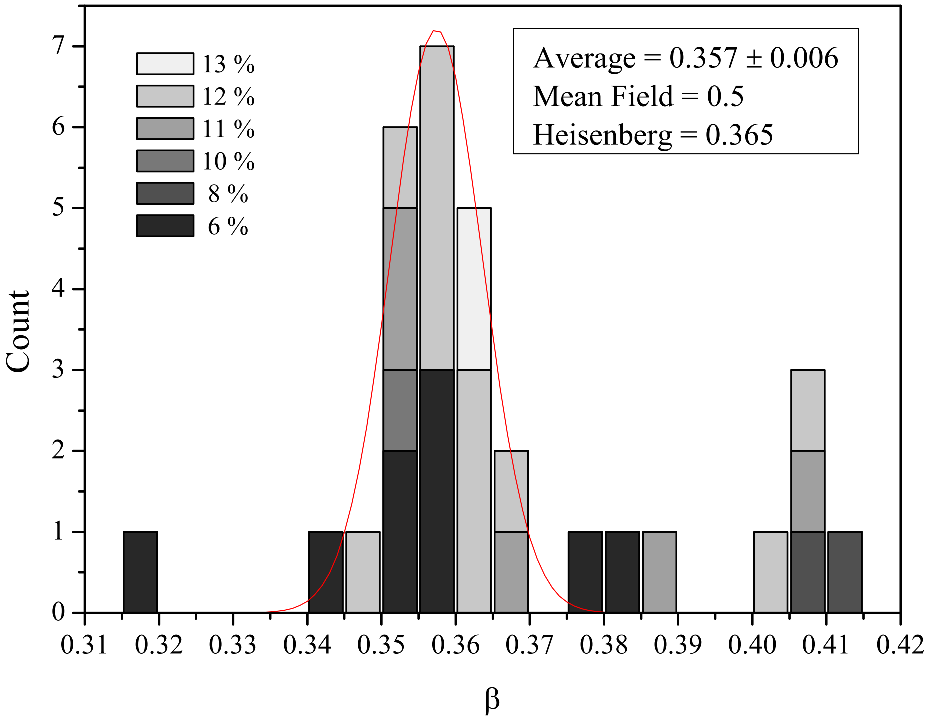

Figure 2.5.17: A histogram of the β values calculated from the past sample measurements. Samples are grouped by manganese concentration as denoted by the left greyscale legend. A wide range of samples with various thicknesses and concentrations show an exponent close to the Heisenberg value, but there are also a several outliers.

that predicted by a T_c broadening of 1 K or less in figure 2.5.13.

2.6 Conclusions

This chapter has detailed an in-depth study of the critical behaviour of (Ga,Mn)As performed on two of the highest Curie temperature samples grown in Nottingham. This work shows that whilst there are a large number of difficulties faced when making such measurements that can easily be overlooked, accurate and reproducible values of the critical exponents can be calculated for both the remanent magnetisation and magnetic susceptibility. Within both samples these were found to exhibit behaviour very close to that of the expected Heisenberg model with a significant number of past datasets demonstrating very similar results. Table 2.2 shows the calculated critical exponents for the magnetometry results compared to those predicted by Ising, Heisenberg and mean-field theory.

Samples	β	γ
Mn433_c	0.368	1.40
Mn438_c6	0.365	1.42
Models	β	γ
Ising 3D	0.326	1.237
Heisenberg	0.365	1.396
Mean-field	0.5	1

Table 2.2: Tabulated results of both the magnetisation (β) and susceptibility (γ) critical exponents compared to that predicted by the Ising, Heisenberg and mean-field models. The calculated values for both samples very closely match that of the Heisenberg model with both exponents appreciably different to the Ising values.

Magnetisation data also showed power-law-like behaviour below the critical region down to temperatures as low as 80 K less than T_c. As with the critical behaviour this was also found in most of the past datasets with calculated exponent values of roughly 0.41. A value appreciably lower than that predicted by mean-field theory, but very close to that observed by Khazen *et al.* (2010). From this it is clear that the choice of fitting range takes an important role when calculating the critical exponents with modelled values close enough together to easily cause confusions about the observed behaviour. However, whilst the same is true of the measurements covered in this chapter, the calculated values shown in table 2.2 and results seen in past samples almost exactly match that expected from Heisenberg theory and are markedly different to that predicted by either the Ising or mean-field models.

Modelling the effects of sample inhomogeneity on magnetometry measurements demonstrated equally compelling results with T_{c} broadening leading to shifts in the Kouvel-Fisher analysis that go a long way to explaining the differences observed between the Curie temperature as calculated from the magnetisation to that by the susceptibility. Whilst there were slight disagreements between these figures for both samples, all but one of the calculated T_{c} values still remained within 0.5 K of that predicted from Arrott plots. Exponent values were also not significantly affected by the broadening due to the appropriate choice of fitting range selected to avoid the drop-off in Kouvel-Fisher plots very close to T_{c}.

References

Arrott, A. and Noakes, J. E. ‘Approximate equation of state for nickel near its critical temperature’. *Physical Review Letters*, **19** (14) 786–789, (1967).

Binney, J. J., Dowrick, N. J., Fisher, A. J., and Newman, M. E. J. *The Theory of Critical Phenomena: An introduction to the renormalization group.* Oxford science publications. Oxford University Press, (1992).

Brey, L. and Gómez-Santos, G. ‘Magnetic properties of GaMnAs from an effective Heisenberg Hamiltonian’. *Physical Review B*, **68** (11) 115206, (2003).

Campostrini, M., Hasenbusch, M., Pelissetto, A., Rossi, P., and Vicari, E. ‘Critical exponents and equation of state of the three-dimensional Heisenberg universality class’. *Physical Review B*, **65** (14) 144520, (2002).

Fan, J., Ling, L., Hong, B., Zhang, L., Pi, L., and Zhang, Y. ‘Critical properties of the perovskite manganite $La_{0.1}Nd_{0.6}Sr_{0.3}MnO_3$’. *Physical Review B*, **81** (14) 144426, (2010).

Ghosh, N., Rößler, S., Rößler, U. K., Nenkov, K., Elizabeth, S., Bhat, H. L., Dörr, K., and Müller, K. H. ‘Heisenberg-like critical properties in ferromagnetic $Nd_{1-x}Pb_xMnO_3$ single crystals’. *Journal of Physics: Condensed Matter*, **18** 557, (2006).

Ising, E. ‘Beitrag zur theorie des ferromagnetismus’. *Zeitschrift für Physik A Hadrons and Nuclei*, **31** (1) 253–258, (1925).

Jiang, W., Wirthmann, A., Gui, Y. S., Zhou, X. Z., Reinwald, M., Wegscheider, W., Hu, C.-M., and Williams, G. ‘Critical behavior from the anomalous Hall effect in (GaMn)As’. *Physical Review B*, **80** (21) 214409, (2009).

Kadanoff, L. P. ‘Scaling laws for Ising models near critical points’. *Physics*, **2** 12, (1966).

Kar, M., Perumal, A., and Ravi, S. ‘Critical behavior studies in $La_{1-x}Ag_xMnO_3$ double-exchange ferromagnet’. *Physica Status Solidi (b)*, **243** (8) 1908–1913, (2006).

Kats, Y., Klein, L., Reiner, J. W., Geballe, T. H., Beasley, M. R., and Kapitulnik, A. ‘Magnetic resistivity in $SrRuO_3$ and the ferromagnetic phase transition’. *Physical Review B*, **63** (5) 54435, (2001).

Khazen, K., von Bardeleben, H. J., Cantin, J. L., Mauger, A., Chen, L., and Zhao, J. H. ‘Intrinsically limited critical temperatures of highly doped $Ga_{1-x}Mn_xAs$ thin films’. *Physical Review B*, **81** (23) 235201, (2010).

Kim, D., Zink, B. L., Hellman, F., McCall, S., Cao, G., and Crow, J. E. ‘Mean-field behavior with Gaussian fluctuations at the ferromagnetic phase transition of $SrRuO_3$’. *Physical Review B*, **67** (10) 100406, (2003).

Kittel, C. *Introduction to Solid State Physics*. Wiley, 7th edition, (2005).

Kouvel, J. S. and Fisher, M. E. ‘Detailed magnetic behavior of nickel near its Curie point’. *Physical Review*, **136** (6 A) 1632, (1964).

Kuivalainen, P. ‘Spin-Dependent Transport in Heavily Mn-Doped GaAs’. *Physica Status Solidi (b)*, **227** (2) 449–463, (2001).

Kuz’Min, M. D. and Tishin, A. M. ‘Experimental critical exponents of ŞpureŤ ferromagnets: The cost of excessive proximity to T_c may be too high’. *Europhysics Letters*, **73** 396–400, (2006).

Lederman, F. L., Salamon, M. B., and Shacklette, L. W. ‘Experimental verification of scaling and test of the universality hypothesis from specific-heat data’. *Physical Review B*, **9** (7) 2981–2988, (1974).

Matsukura, F., Ohno, H., Shen, A., and Sugawara, Y. ‘Transport properties and origin of ferromagnetism in (Ga,Mn)As’. *Physical Review B*, **57** (4) 2037–2040, (1998).

Moca, C. P., Sheu, B. L., Samarth, N., Schiffer, P., Janko, B., and Zarand, G. ‘Scaling Theory of Magnetoresistance and Carrier Localization in $Ga_{1-x}Mn_xAs$’. *Physical Review Letters*, **102** (13) 137203, (2009).

Muller-Krumbhaar, H. ‘Critical properties of Heisenberg ferromagnets with lattice inhomogeneity’. *Journal of Physics C: Solid State Physics*, **9** (2) 345–350, (1976).

Novák, V., Olejník, K., Wunderlich, J., Cukr, M., Výborný, K., Rushforth, A. W., Edmonds, K. W., Campion, R. P., Gallagher, B. L., Sinova, J., and

Jungwirth, T. 'Curie Point Singularity in the Temperature Derivative of Resistivity in (Ga,Mn)As'. *Physical Review Letters*, **101** (7) 077201, (2008).

Onsager, L. 'Crystal statistics. I. A two-dimensional model with an order-disorder transition'. *Physical Review*, **65** (3-4) 117–149, (1944).

Priour, D. J. and Das Sarma, S. 'Critical behavior of diluted magnetic semiconductors: Apparent violation and eventual restoration of the Harris criterion for all regimes of disorder'. *Physical Review B*, **81** (22) 224403, (2010).

van Esch, A., van Bockstal, L., de Boeck, J., Verbanck, G., van Steenbergen, A. S., Wellmann, P. J., Grietens, B., Bogaerts, R., Herlach, F., and Borghs, G. 'Interplay between the magnetic and transport properties in the III-V diluted magnetic semiconductor $\mathrm{Ga}_{1-x}\mathrm{Mn}_x\mathrm{As}$'. *Physical Review B*, **56** (20) 13103–13112, (1997).

Wang, M., Campion, R. P., Rushforth, A. W., Edmonds, K. W., Foxon, C. T., and Gallagher, B. L. 'Achieving high Curie temperature in (Ga,Mn)As'. *Applied Physics Letters*, **93** (13) 132103, (2008).

Wilson, K. G. 'Renormalization Group and Critical Phenomena. I. Renormalization Group and the Kadanoff Scaling Picture'. *Physical Review B*, **4** (9) 3174–3183, (1971).

Yuldashev, S. U., Igamberdiev, K. T., Lee, S., Kwon, Y., Kang, T. W., and Shashkov, A. G. 'Study of $\mathrm{Ga}_{1-x}\mathrm{Mn}_x\mathrm{As}$ Critical Behavior by Using Thermal Diffusivity'. *Journal of the Korean Physical Society*, **59** (2) 431–434, (2011).

Chapter 3

Transport Properties Close to the Curie Temperature

3.1 Introduction

In chapter 2 a comprehensive study of critical behaviour was presented centred on the calculation of critical exponents with the aim of confirming the Heisenberg-like behaviour predicted by Priour and Das Sarma (2010). This chapter revisits critical phenomena in (Ga,Mn)As, but shifts the focus away from the magnetic properties to the study of the resistance behaviour close to T_c. As covered in the introductory chapter the position of the peak in resistance relative to the Curie temperature is widely contested. Whilst early work on (Ga,Mn)As implied that both lie at the same temperature, more recent studies have demonstrated that it is in fact the peak in the differential that is at T_c (Novák *et al.* (2008)).

Such a suggestion is not a new concept with early measurements on transport critical phenomena in metals demonstrating similar cusps in $\frac{\mathrm{d}R}{\mathrm{d}T}$ at the Curie temperature (Craig *et al.* (1967); Shacklette (1974)). This behaviour was in contrast to that predicted by earlier theoretical work (De Gennes and Friedel (1958)), but explained by M. E. Fisher and J. S. Langer by relating $\frac{\mathrm{d}R}{\mathrm{d}T}$ to the expected critical phenomena seen in the specific heat (Fisher and Langer (1968)).

Section 2.2.2 of the previous chapter shows how this is expected to follow a power-law upon approaching T_c similar to both the magnetisation and susceptibility. Accurate measurements of the resistance close to T_c could therefore support the Heisenberg behaviour observed in the magnetic critical behaviour as well as potentially confirming the peak position behaviour. Despite these motivations transport properties close to T_c have not been widely studied in (Ga,Mn)As. Past measurements of both the resistance and specific heat have shown very mixed results with the accurate calculation of the α critical exponent proving difficult (Novák *et al.* (2008); Yuldashev *et al.* (2011)).

Vit Novák's group performed both magnetisation and resistance measurements on a variety of (Ga,Mn)As samples both as-grown and annealed to make comparisons between the peak in $\frac{\mathrm{d}R}{\mathrm{d}T}$ and the Curie temperature. Peaks were found to be very close to T_c for the annealed samples, but appreciably lower than T_c for as-grown or only partially annealed samples. Calculations of the α critical exponent resulted in non-linear log-log plots of $\frac{\mathrm{d}R}{\mathrm{d}T}$ with little sign of the expected power-law behaviour in the critical region even for the annealed samples. The group was therefore unable to draw exact conclusions about the nature of the critical behaviour in (Ga,Mn)As.

This chapter presents a more thorough study of $\frac{\mathrm{d}R}{\mathrm{d}T}$ focused around the critical region with the aim of confirming the peak behaviour observed by Novák *et al.* (2008), and then calculating the α critical exponent. These studies will act as a continuation of the magnetic critical behaviour work with measurements performed on the same high T_c annealed (Ga,Mn)As samples. Having covered the critical phenomena background theory in the previous chapter the next section will move straight to the data analysis methods used to calculate α, and the additional problems associated with resistance measurements over the previous critical phenomena study. The results will then be presented following a similar layout to the previous chapter including the calculation of the critical exponent above and below T_c, the effects of broadening both on the calculated exponent and the position of the peak, and a comparison to past datasets.

3.2 Measuring Critical Exponents

3.2.1 Data Analysis

Within the previous chapter both the β and γ critical exponents were calculated using the Kouvel-Fisher method in order to avoid the need for prior knowledge of the system. Unfortunately, this method is not possible when analysing the specific heat or the behaviour of $\frac{\mathrm{d}R}{\mathrm{d}T}$ close to T_c due to the additional terms shown in section 2.2.2.

When analysing the critical behaviour of the specific heat the standard method used to calculate exponent α is to fit to an equation of the form shown by (3.2.1) containing both singular and non-singular components.

$$C(T) = C_\mathrm{R}(t) + At^{-\alpha}\left(1 + g(t)\right) \tag{3.2.1}$$

The non-singular, or regular, part of the specific heat $C_\mathrm{R}(t)$ is given by a power law series

$$C_\mathrm{R}(t) = C_0 + C_1 t + C_2 t^2 + \cdots \tag{3.2.2}$$

Whilst the singular part of the specific heat takes the form of the leading power term α with correction to scaling terms described by $g(t)$.

$$g(t) = Dt^{\Delta} + \cdots \tag{3.2.3}$$

Within both these singular and non-singular components quantities such as A, C_0 and D may take different values above and below T_c. This is indicated in equations by the use of subscripts + and − respectively. Both α and Δ are expected to take the same values above and below T_c with renormalisation group theory and measurements on the superfluid transition of liquid helium (Greywall and Ahlers (1972)) showing the correction exponent to be 0.5 within short range systems.

Directly fitting this equation to the (Ga,Mn)As $\frac{\mathrm{d}R}{\mathrm{d}T}$ data is not possible due to both the high number of unknown fitting parameters and the addition of unnecessary terms used to remove a linear background from analogous specific heat data. Early studies on the specific heat of iron (Lederman *et al.* (1974)) and nickel (Connelly *et al.* (1971)) made use of a special case of equation (3.2.1) assuming a linear non-singular background without the additional singular correction terms. Simplifying the data analysis in this way allowed fitting to be performed to a shifted power law by first removing the linear background calculated at high t away from T_c. A similar method was also used on the resistivity critical behaviour for these materials (Shacklette (1974); Zumsteg and Parks (1970); Craig *et al.* (1967)).

Fitting to the (Ga,Mn)As $\frac{\mathrm{d}R}{\mathrm{d}T}$ data was therefore performed using the same method using equations (3.2.4) and (3.2.5) for above and below T_c respectively.

$$\frac{\mathrm{d}R}{\mathrm{d}T}_{+} = a_{+}\frac{\left(t^{-\alpha} - 1\right)}{\alpha} + b_{+} \tag{3.2.4}$$

$$\frac{\mathrm{d}R}{\mathrm{d}T}_{-} = a_{-}\frac{\left(t^{-\alpha'} - 1\right)}{\alpha'} + b_{-} \tag{3.2.5}$$

3.2.2 Probe Design

One of the main aims of this chapter is to accurately compare the peak position in $\frac{\mathrm{d}R}{\mathrm{d}T}$ with the Curie temperature. A consistent method was therefore required to measure both T_c and the resistance profile. The most practical way of retaining this consistency is by using a single system for both sets of measurements effectively using the same thermometer setup. All measurements were performed within the SQUID system used in chapter 2. This allowed magnetometry measurements to be performed to accurately calculate T_c. However, in order to perform measurements of sample resistances within this system, wires first had to be introduced running the length of the probe without significantly affecting the magnetometry or operation.

Following similar principles to that of the diamagnetic background removal within the magnetometry measurements, electrical contact to samples from the probe were made via the use of gold track covered silicon rods 175 mm in length. The uniformity of these and the gold running the length therefore minimised their potential background contribution to the magnetisation. These rods were fabricated via photolithography from 8 inch wafers by the Southampton

Nanofabrication Centre each containing four 850 μm width gold tracks separated by 150 μm. A simple four-contact pattern design was then used to fabricate contact pads onto the samples via a standard photolithography and evaporation process with a 20 nm layer of titanium and 100 nm layer of gold. This allowed direct bonding to the silicon rod gold tracks.

These silicon rod holders were fitted onto the probe via a redesigned header attachment consisting of a non-magnetic clamp structure containing four exposed wire contacts. Silicon rods were held in place using both a straw outer-sleeve and a nylon screw to tighten the clamp after gold track and wire contact alignment. These wires were ran the length of the probe to a sealed 12 pin connector at the top of the SQUID with a spring-like arrangement at the end to allow movement of the probe when taking magnetometry measurements. Figure 3.2.1 shows a diagram of the SQUID probe design used for electrical measurements including the silicon rod and clamp holder.

3.2.3 Experimental Methods

Transport and magnetometry measurements were performed within the same superconducting quantum interference device (SQUID) system as that used in chapter 2. Initial testing on both samples showed unusually high resistances for two Mn433_c contacts. These damaged contact pads lead to anomalous behaviour at low temperatures limiting measurements on this sample to a two-terminal probe setup between an adjacent current-voltage contact pair separated by 0.5 mm. Both four- and two-terminal measurements were performed on sample Mn438_c6 to observe the potential effects of contact resistance on the critical behaviour. All resistance measurements were performed using a Keithley K2400 source-meter with an applied constant current of 10 μA.

Magnetometry measurements were performed on both samples following the same procedure as that developed for the high-resolution work covered in the previous chapter. Samples were first field-cooled at 300 Oe down to roughly 30 K below the expected Curie temperature, and then remanent magnetisation measurements performed at zero field using a sweep rate of 0.1 Kmin^{-1} up to 20 K above T_c. This larger temperature sweep range was used in order to allow simultaneous resistance measurements recorded at five second intervals.

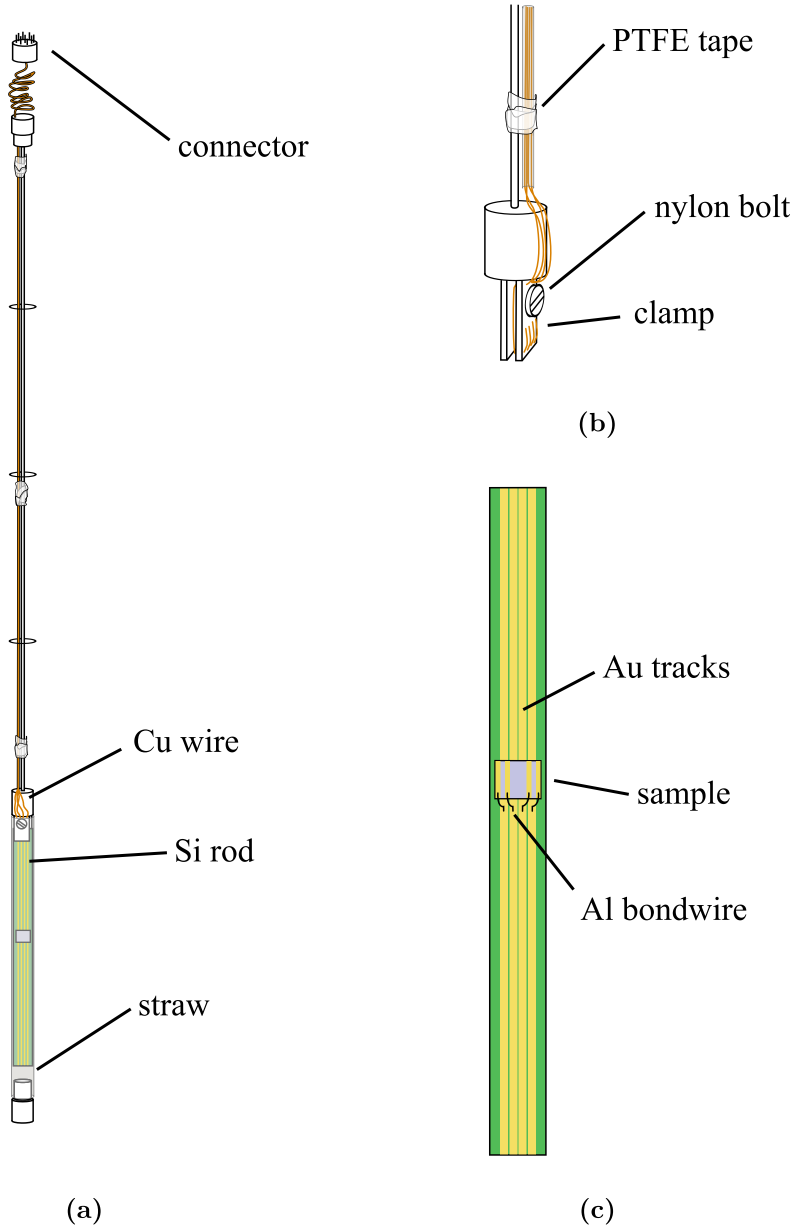

Figure 3.2.1: (a) A diagram of the SQUID probe used to perform electrical measurements with copper wires running from the clamp holder to an external connector at the top. (b) The clamp design with a nylon bolt to hold the silicon rod in place and PTFE tape to secure the copper wires to the probe. (c) The four-contact sample design with 0.5 mm x 4 mm bond pads and a distance between the central contacts of 2 mm.

Resistance and magnetometry measurements were also performed independently to test for any unwanted additions to the magnetisation due to an applied current. In both samples only a very slight difference was observed over the critical region with no significant effects on the data analysis or calculated exponent value. Measurements were repeated for the purpose of averaging to reduce noise within the resistance and subsequent $\frac{dR}{dT}$ data. Additional measurements of the resistance were also performed whilst sweeping down in temperature leading to a slight shift in the observed peak of less than 1 K relative to the measurements performed during remanent magnetisation warm-up. Such a small shift demonstrates that the measured thermometer temperature is very close to the actual sample temperature. A larger shift was observed when monitoring the resistance during field-cooling due to the much higher sweep rate of 10 Kmin^{-1}.

3.3 Results

3.3.1 Resistance

Figure 3.3.1 shows averaged resistance against temperature data for samples Mn438_c6 and Mn433_c taken within the SQUID system at the same time as further remanent magnetisation measurements. The two-terminal measurements on sample Mn433_c shown in 3.3.1b were carried out between adjacent current and voltage probe contacts 0.5 mm apart as shown in figure 3.2.1c.

The similar measured resistance magnitudes in both (a) and (b) demonstrate a high contact resistance for sample Mn433_c. Two-terminal testing conducted at room temperature on this sample showed a completely non-symmetric structure with one pair of current-voltage contacts showing a resistance more than twice that of the other pair. Resistance versus temperature measurements for the higher resistance pair showed a significant increase at temperatures less than 100 K unlike that expected for a standard (Ga,Mn)As sample. The measurements shown in 3.3.1b are therefore that of the lower resistance contacts.

Room temperature test measurements on Mn438_c6 revealed much lower resistances with both pairs of current-voltage probe contacts within 0.5 Ω of each other and less than a quarter of that shown for Mn433_c. Resistance

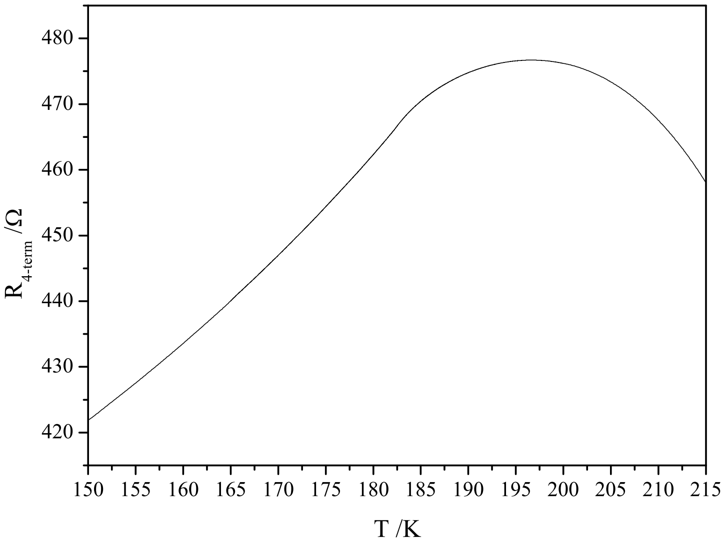

(a)

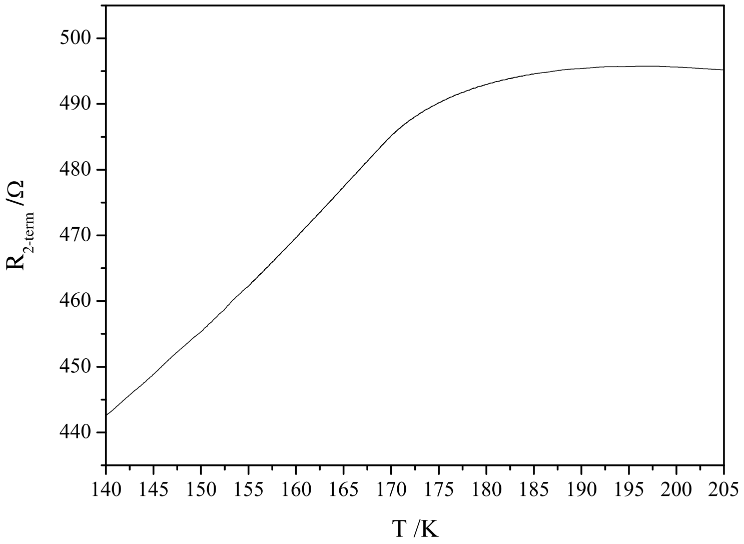

(b)

Figure 3.3.1: Resistance against temperature measurements of samples Mn438_c6 (a) and Mn433_c (b) performed within the SQUID system.

versus temperature measurements for all sets of contacts also resulted in similar behaviour to that of the four-terminal with no increase at lower temperatures. However, whilst the two-terminal measurements for Mn438_c6 were much closer in magnitude to that expected, the behaviour above T_c is slightly different to that observed in other annealed samples.

Figure 3.3.1 shows how the resistance of Mn438_c6 drops away much more rapidly than the more standard behaviour seen in the Mn433_c data. This steep drop in resistance is also seen in the field-cool data with non-linear behaviour down to a room temperature resistance of 322 Ω. Such behaviour with a narrow peak and non-linear drop-off is usually observed within as-grown samples with much lower T_c values. The standard behaviour for high T_c annealed samples is a more gradual linear drop approaching room temperature.

Past Hall bar measurements performed on another Mn438 sample showed similar uncharacteristic behaviour at higher temperatures dependent on the applied current. A stronger drop-off was observed when applying lower currents. Figure 3.3.2 shows both a scaled comparison between the SQUID and Hall bar datasets (a), and the effects of varying the applied current (b). All past Mn438 Hall bar measurements were performed by Dr. Andrew Rushforth.

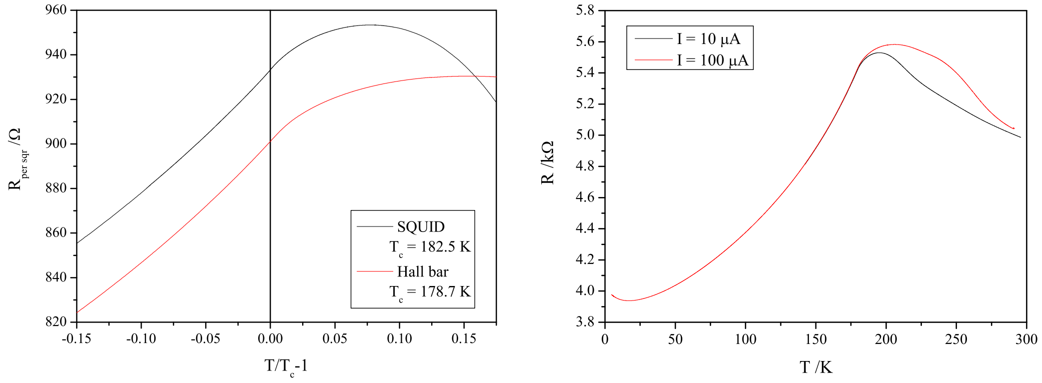

(a) (b)

Figure 3.3.2: (a) A rescaled plot of the resistance of Mn438_c6 (black) compared to the past dataset performed on a Hall bar structure (red) with an applied current of 100 μA. Both T_c values were taken as the peak in their respective derivatives. (b) A comparison between the past Hall bar data applying constant currents of 10 μA (black) and 100 μA (red).

One possible explanation for this non-linear I-V behaviour could be that wafer Mn438 consists of a bilayer of (Ga,Mn)As unintentionally caused by the MBE growth conditions required to produce such a high T_c sample. Partial shorting could therefore be occurring through a thin top film at higher temperatures with the bulk then dominating below the peak. This could result in a distortion of the $\frac{\mathrm{d}R}{\mathrm{d}T}$ critical behaviour above T_c.

Both resistance datasets in figure 3.3.1 were used to calculate the temperature derivative for each sample by first interpolating the data, and then smoothing using a 20 point adjacent average before numerical differentiation. The resulting plots were then compared to the remanent magnetisation data as shown in figures 3.3.3 and 3.3.4 with the peak in the derivative expected to be at T_c.

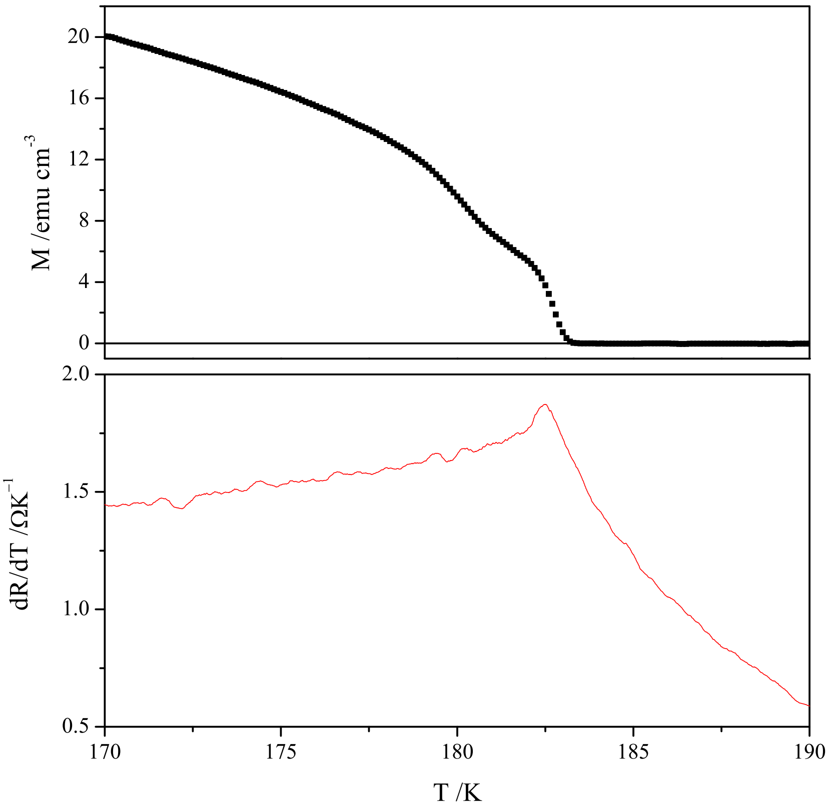

Figure 3.3.3: The average of the measured remanent magnetisations conducted with the resistance measurements (top), and the calculated temperature derivative of the resistance (bottom) for sample Mn438_c6.

Sample Mn438_c6 shows a sharp peak in $\frac{\mathrm{d}R}{\mathrm{d}T}$ at 182.5 K suggesting a drop in T_c of more than 1 K compared to that calculated from the magnetometry performed prior to contact fabrication for the previous chapter. The most probable reason for this is the large period of time between measurements due to difficulties with the probe header design. Reductions in T_c over time are not uncommon within annealed (Ga,Mn)As with similar drops observed in most past samples.

A similar drop in T_{c} is also apparent within the latest magnetisation data with a good agreement between this and the $\frac{\mathrm{d}R}{\mathrm{d}T}$ peak. However, unlike the previous magnetometry the exact value of T_{c} cannot be calculated via Kouvel-Fisher analysis due to the unusual behaviour seen in the critical region. Possible explanations for this could be the presence of a slight magnetic field due to trapped flux or a non-uniaxial sample in some way caused by the contact fabrication process.

A non-uniaxial sample may also explain the noticeable drop in magnetisation seen after contact fabrication compared to that shown in figure 2.5.1. However, whilst previous non-uniaxial samples have shown a hump just below T_{c} when measuring in the [110] direction, such a pronounced dip in the $[1\bar{1}0]$ direction has not been observed before.

In contrast the magnetisation data for Mn433_c shown in figure 3.3.4 is much closer to the expected profile with no visible anomalies except a slight tail above T_{c} most likely caused by broadening. Compared to the measurements performed prior to contact fabrication there is a significant reduction in the overall magnetisation similar to that seen in Mn438_c6. However, Kouvel-Fisher analysis on this data still results in calculated T_{c} and β-exponent values close to that of the previous measurements as shown in figure 3.3.5.

Figure 3.3.4 also shows the $\frac{\mathrm{d}R}{\mathrm{d}T}$ data for Mn433_c. Unlike the Mn438_c6 data shown in 3.3.3 this two-terminal data does not show a sharp well defined peak and has a much larger associated noise. However, data above T_{c} does suggest a peak close to the 168.5 K calculated via Kouvel-Fisher on the remanent magnetisation. The increase in noise results from the two-terminal nature of the measurements with T_{c} broadening likely contributing to the flattening of the peak.

Two-terminal data on sample Mn438_c6 showed a similar increase in noise with a much less well defined peak to that seen in 3.3.3. The comparison between both datasets in figure 3.3.6 also shows a vertical shift suggesting a temperature dependent contribution to the resistance from the contacts that must be considered when analysing the Mn433_c data. Within sample

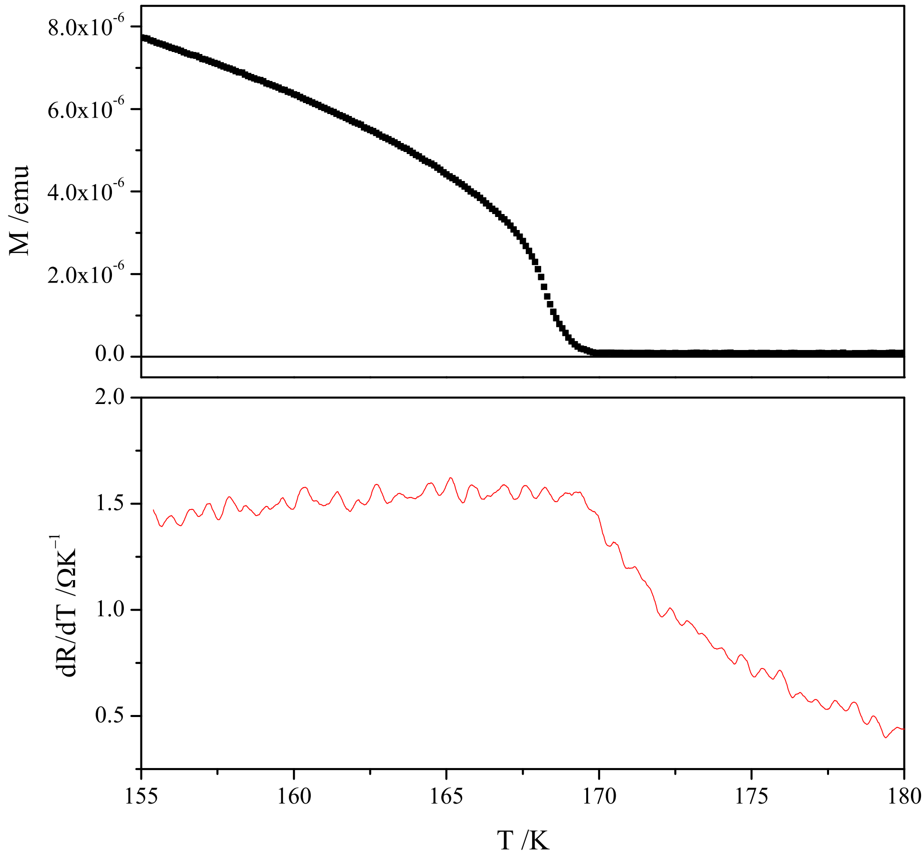

Figure 3.3.4: The average of the measured remanent magnetisations conducted with the resistance measurements (top), and the calculated temperature derivative of the resistance (bottom) for sample Mn433_c.

Mn438_c6 this shift appears to be roughly constant below T_c indicating a linear contribution to the resistance that is included within the fitting equation (3.2.5). Both plots then show different profiles at increasing temperatures above T_c with the two-terminal data showing a steeper drop-off. However, these additional terms are most likely related to the unusual behaviour of the resistance at higher temperatures, and are therefore not expected within Mn433_c.

Both samples clearly show a peak in $\frac{dR}{dT}$ that is much closer to the Curie temperature than that of the peak in resistance. However, unlike the magnetometry data in section 2.5 the exact value of the relevant critical exponent α cannot easily be calculated from the data. The two most important reasons for this are the expected low magnitude of α and the shift applied to the power law preventing the direct use of either Kouvel-Fisher analysis or log-log plots. Curie

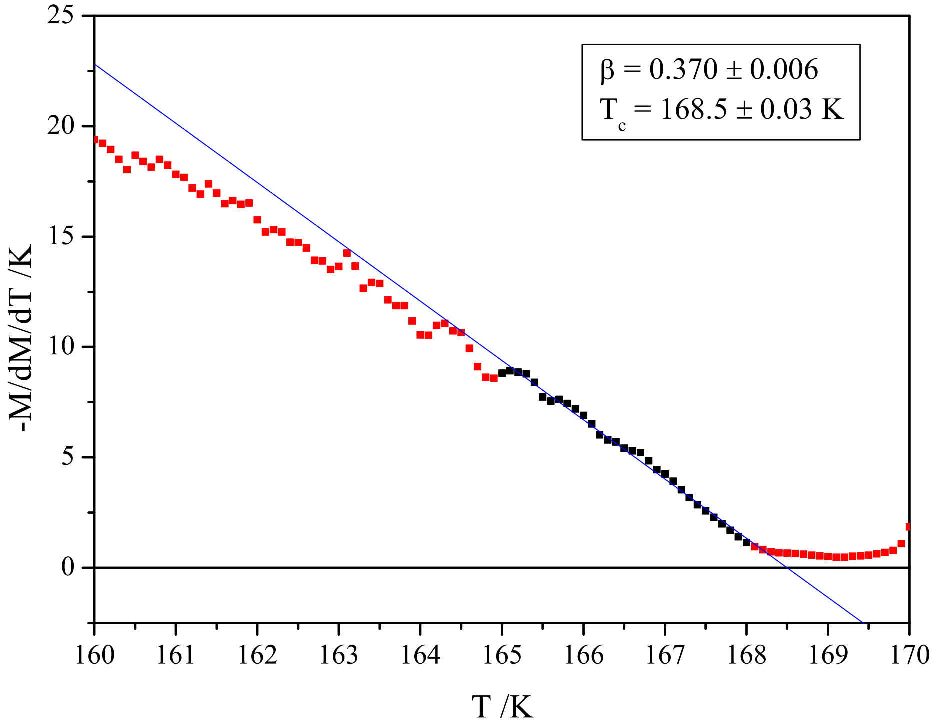

Figure 3.3.5: A Kouvel-Fisher plot of the remanent magnetisation for sample Mn433_c after contact fabrication as shown in figure 3.3.4.

temperature broadening, as seen in both the magnetisation and susceptibility data, is also expected to further distort the critical behaviour as discussed in the next section.

Given these difficulties data was fitted to equations (3.2.4) and (3.2.5) using fixed values for both T_c and α as a comparison to the expected Heisenberg behaviour. Figure 3.3.7 shows the $\frac{dR}{dT}$ data of Mn438_c6 plotted against the reduced temperature taking the peak as T_c and $\alpha = -0.13$.

Fixing both these values for sample Mn438_c6 suggests that $\frac{dR}{dT}$ below the Curie temperature could follow behaviour close to that of the Heisenberg model. At reduced temperatures higher than 0.05 the data begins to drop away faster than the given fit. However, further fitting over larger ranges showed that this could be accounted for by adjusting parameters a_- and b_- without significantly changing the fit over the expected critical region.

Including the exponent as an open fitting parameter resulted in a calculated

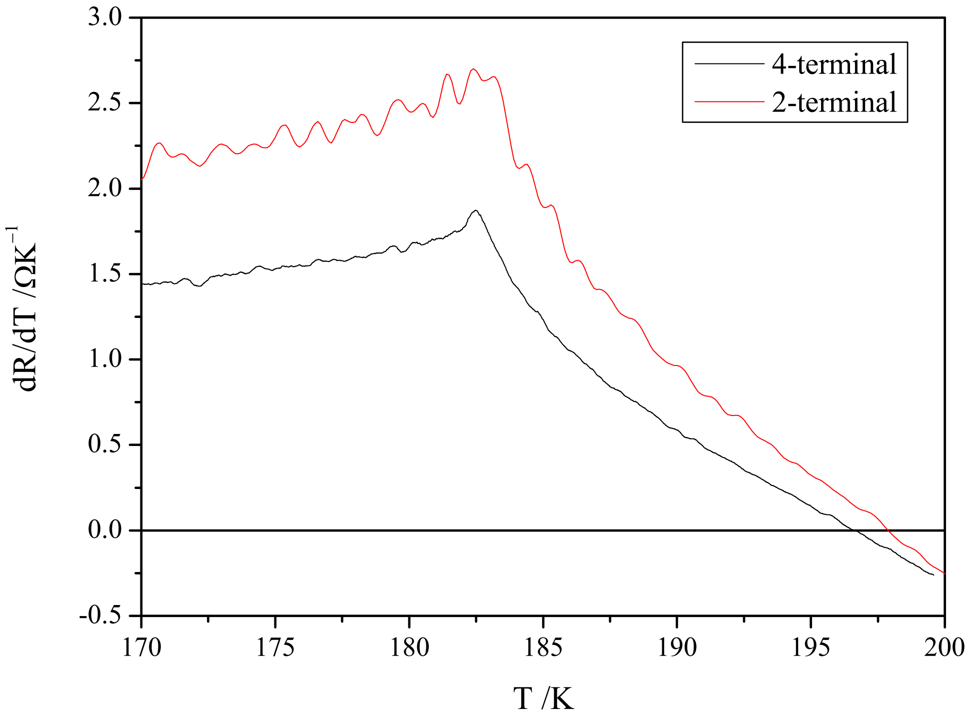

Figure 3.3.6: The temperature derivative of both the two-terminal (red) and four-terminal (black) resistances taken on sample Mn438_c6. Both sets of data were taken simultaneously using the Keithley source to make the two-terminal measurement across the whole sample from one current contact to the other.

α value of -0.369 a long way from any of the expected theoretical models clearly demonstrating the difficulties associated with the fitting. The addition of further terms and fitting parameters, as seen by equation (3.2.1), lead to very high dependencies between parameters allowing a wide range of calculated exponent values.

Above T_c the comparison shows a clearer disparity between the data and the expected Heisenberg behaviour with a much stronger drop-off in the power law to that of the experimental results. Unlocking the exponent whilst retaining a fixed Curie temperature of 182.5 K resulted in a calculated α values of -0.476, again much higher in magnitude than any of the theoretical values. This difference is most likely linked to the non-linear current response observed in the Mn438 Hall bar sample, and therefore the unusual behaviour observed at higher temperatures.

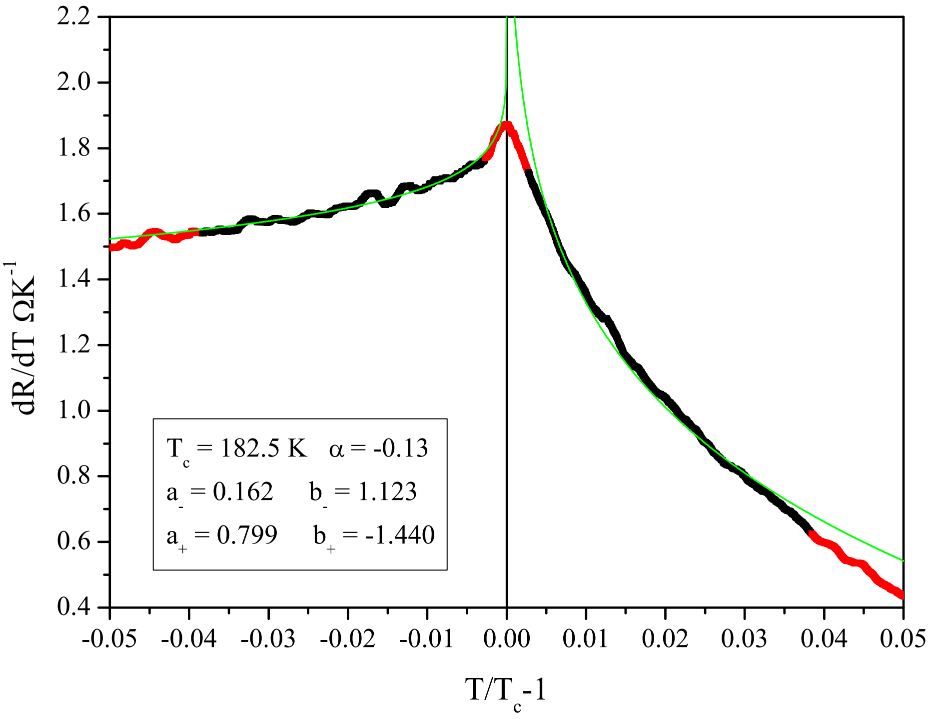

Figure 3.3.7: The four-terminal $\frac{\mathrm{d}R}{\mathrm{d}T}$ data of sample Mn438_c6 compared to a shifted Heisenberg fit from equations (3.2.4) and (3.2.5). Fitting ranges were chosen based on the previous work on sample magnetometry.

Within most annealed samples the addition of non-magnetic contributions to the resistance can be approximated via a linear extrapolation at high temperatures (Novák *et al.* (2008)). This is taken into account within the fitting equations by the constant b. As seen previously, this is not the case in Mn438_c6 potentially due to this sample consisting of two layers of (Ga,Mn)As. Given the change in behaviour seen between the four- and two-terminal data for this sample it is unlikely that this can be removed or reliably be taken into account when fitting.

Figure 3.3.8 shows the $\frac{\mathrm{d}R}{\mathrm{d}T}$ data for sample Mn433_c with fixed α fitting above T_c. A strong agreement is seen between this data and that predicted by the Heisenberg model giving further evidence towards the suggestion that the high temperature data of Mn438_c6 includes additional unwanted terms. This agreement is even seen to continue beyond the expected critical region all the way up to 185 K at a reduced temperature close to 0.1. Opening the exponent

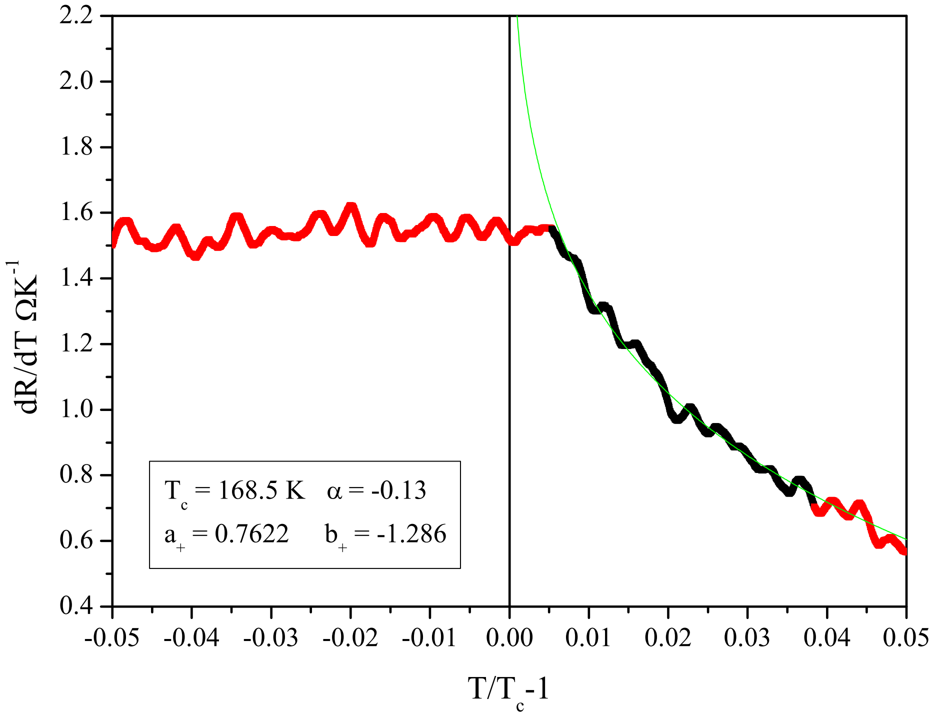

Figure 3.3.8: The $\frac{dR}{dT}$ data of sample Mn433_c compared above T_c to the Heisenberg fit from equation (3.2.4). Fitting was only performed above T_c due to the flattened peak and high associated noise from the two-terminal data. The Curie temperature was taken from that calculated from the magnetisation data via Kouvel-Fisher.

as a fitting parameter results in a calculated α value of -0.144 very close to the Heisenberg model. Fitting was not performed on the data below T_c due to the flattening of the peak.

3.3.2 Curie Temperature Broadening

Both datasets shown in figures 3.3.3 and 3.3.4 show a general agreement between the remanence and $\frac{dR}{dT}$ for samples Mn438_c6 and Mn433_c respectively. However, even for sample Mn438_c6 with the sharper peak in the derivative, the predicted T_c value appears slightly lower than that of the remanence data. As has been discussed previously for the magnetometry work in section 2.5.5 one possible reason for this slight drop and broadening of the peak is sample inhomogeneity.

Curie temperature broadening of $\frac{\mathrm{d}R}{\mathrm{d}T}$ was modelled in the same way as that of the remanent magnetisation via a Gaussian distribution of T_c as shown by equation (3.3.1).

$$\frac{\mathrm{d}R}{\mathrm{d}T} = \frac{1}{\sqrt{2\pi}\Delta}\int\left(a\frac{(t^{-\alpha}-1)}{\alpha}+b\right)\exp\left(-\frac{(T_\mathrm{c}-T_\mathrm{c0})^2}{2\Delta^2}\right)\mathrm{d}T_\mathrm{c} \tag{3.3.1}$$

Figure 3.3.9 shows the modelled T_c broadening assuming Heisenberg behaviour both above and below T_c. Parameters a and b were selected to take into account the anti-symmetric behaviour seen in samples Mn438_c6 and Mn433_c, and the past samples covered in section 3.3.3.

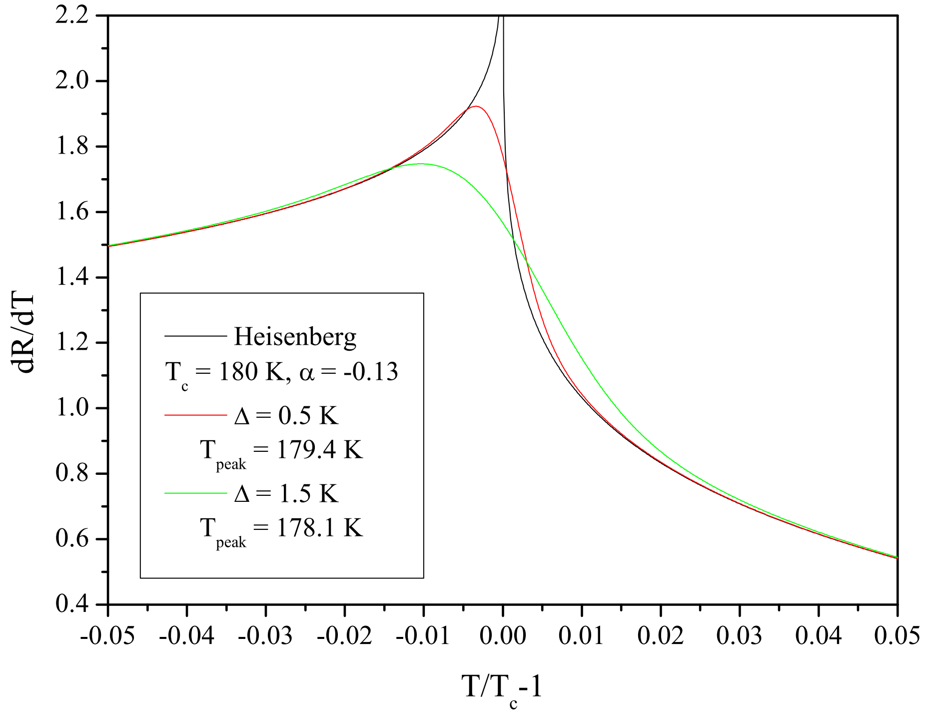

Figure 3.3.9: The standard Heisenberg modelled $\frac{\mathrm{d}R}{\mathrm{d}T}$ (black) using constants $a_- = 0.3$, $b_- = 0.75$, $a_+ = 0.5$, and $b_+ = -0.7$, and the Gaussian broadened plots with Δ values of 0.5 K (red) and 1.5 K (green).

Assuming both sides of the peak follow the Heisenberg behaviour with the same critical exponent $\alpha = -0.13$, a shift in the peak, and therefore observed T_c, only occurs when constants a and b are different above and below. The effects of Gaussian broadening alone only act to flatten and widen the peak. Both samples measured in this chapter and all past samples show the behaviour above T_c to drop away much more than that below resulting in a decrease in the observed peak position.

Magnetometry results in section 2.5 demonstrated a T_c broadening across samples of between 0.5 K and 1 K; this is shown in figure 3.3.9 as the red plot. The drop from T_c = 180 K to T_peak = 179.4 K is comparable to, but slightly larger than, the difference seen between the remanent magnetisation and the $\frac{\mathrm{d}R}{\mathrm{d}T}$ peak in Mn438_c6. However, whilst this shift is close to that expected, making the appropriate adjustments to the Mn438_c6 data analysis is still not enough to explain the behaviour above T_c.

Figure 3.3.10 shows fits to the 0.5 K and 1.5 K Gaussian broadened $\frac{\mathrm{d}R}{\mathrm{d}T}$ plots both above and below T_c. The Curie temperature was taken both as the modelled value of 180 K and the observed peak in the respective plots to demonstrate the effects of selecting an incorrect value of T_c on the calculated exponent value. Fitting ranges were chosen based on the expected critical range from samples Mn438_c6 and Mn433_c, and the position and profile of the peak.

Fitting below the Curie temperature on the T_c = 180 K plots resulted in calculated exponents approaching that of the original Heisenberg value whilst fitting above resulted in positive values closer to that of the 3D Ising model. This split between the behaviour above and below T_c is then seen to further increase when fitting to the data using an incorrect value for the Curie temperature. Fits to both $\frac{\mathrm{d}R}{\mathrm{d}T}$ broadened plots taking T_c as the peak resulted in exponent values much higher in magnitude than any of the ferromagnetic models shown in section 2.2.3.

Sample inhomogeneity could therefore explain the large disparity seen between the Mn438_c6 data and that predicted by the Heisenberg model. Fitting to the Mn438_c6 dataset was performed taking T_c as the peak in $\frac{\mathrm{d}R}{\mathrm{d}T}$ due to anomalies in the magnetisation. This lead to calculated exponent values comparable to that seen in figure 3.3.10c. The Mn433_c data, however, was fitted to using the Kouvel-Fisher calculated T_c resulting in a much better agreement even with the addition of the two-terminal noise.

Graphs 3.3.10a and 3.3.10b also demonstrate the potential importance of the chosen fitting range with the 1.5 K broadened plot resulting in a calculated α

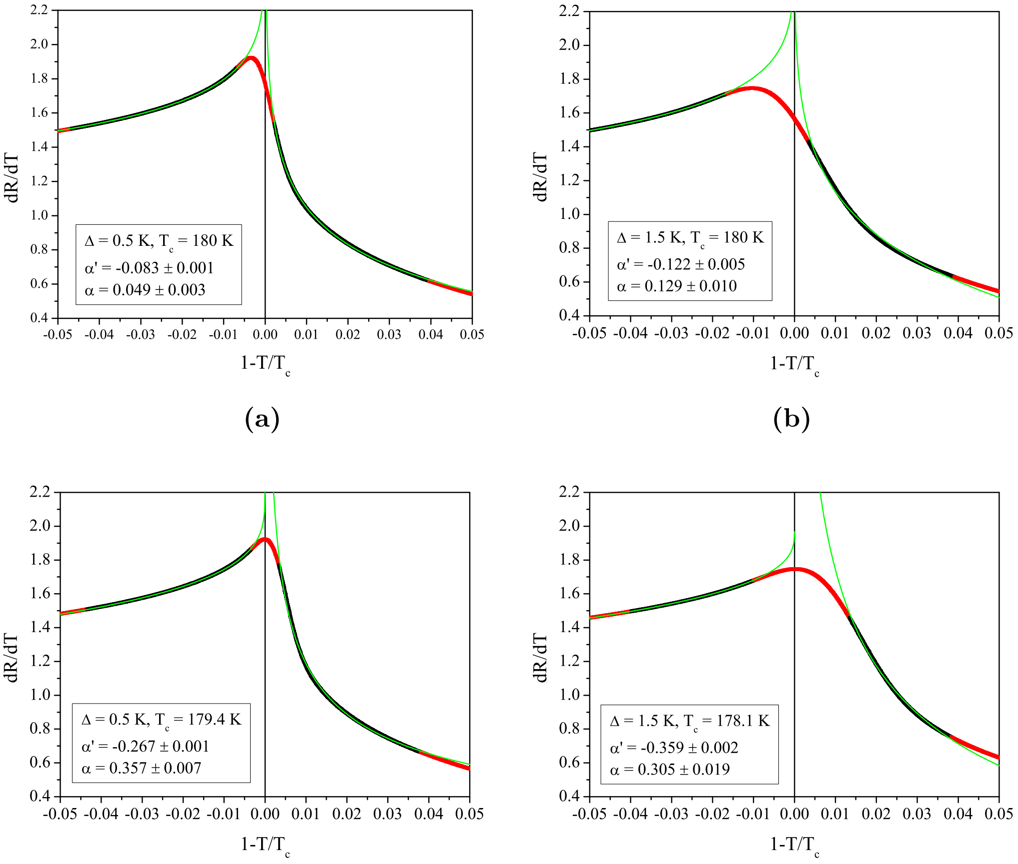

(a) **(b)**

(c) **(d)**

Figure 3.3.10: Fits to both the Δ = 0.5 and Δ = 1.5 Gaussian broadened plots shown in figure 3.3.9 using equations (3.2.4) and (3.2.5) above and below T_c respectively. Graphs (a) and (b) show the fitting performed by fixing T_c to be the actual Curie temperature 180 K, and graphs (c) and (d) the fitting performed by taking T_c to be the peak in $\frac{dR}{dT}$.

value closer to the modelled -0.13 value than that of the 0.5 K plot. It is clear from these results that directly fitting to real data is unlikely to yield accurate calculations of α even for high quality (Ga,Mn)As samples such as Mn438_c6 and Mn433_c. Fitting to datasets taking a T_c value only 0.5 K away from the actual sample Curie temperature or fitting too close to the peak can result in considerably different calculated exponents.

3.3.3 Past Samples

Past resistance measurements on (Ga,Mn)As samples were all performed on Hall bar structures within a standard cryostat system. For this reason corresponding magnetisation measurements were performed on different chips taken from the same wafer. Curie temperatures were therefore not accurately calculated for each sample due a disparity between the magnetometry and resistance caused by the effects of wafer inhomogeneity and the position of thermometers within each system. When these measurements were performed the thermometer positions within the cryostat were not sufficiently close to the sample for the Curie temperature accuracy required to calculate α resulting in a difference between the measured temperature and the actual sample temperature. It was for these reasons that the resistance measurements covered in this chapter were performed within the same system as the magnetometry.

Given the $\frac{\mathrm{d}R}{\mathrm{d}T}$ broadening results it is not possible to accurately calculate an averaged α from these samples in the same way as that of the magnetometry. Differentiation of most of the past resistance datasets resulted in broad or slightly noisy curves with higher T_c samples generally leading to more well-defined peaks comparable to that seen in Mn438_c6 and Mn433_c. Without accurate Curie temperatures fitting to such peaks could only be performed by assuming a value for T_c to give a rough comparative calculation of α.

Figure 3.3.11 shows four examples of fits to past sample datasets. The temperature derivatives were calculated using a similar method to that used for samples Mn438_c6 and Mn433_c via interpolation, adjacent averaging, and numerical differentiation. Fitting was then performed based on the 1 K Gaussian broadened plot and the previous measurements taking T_c as a point above the peak in $\frac{\mathrm{d}R}{\mathrm{d}T}$ relative to the 0.7 K difference seen in figure 3.3.10a. Reduced temperature fitting ranges were chosen based on this T_c value and the range used for Mn438_c6 and Mn433_c.

All four samples shown in 3.3.11 demonstrate behaviour above the peak very close to that of the expected Heisenberg model. Fits taking a fixed value of $\alpha = -0.13$ resulted in strong agreements up to roughly $t = 0.1$ similar to that seen in Mn433_c. However, calculated exponents varied significantly when changing either the fixed T_c value or the fitting range. In some cases

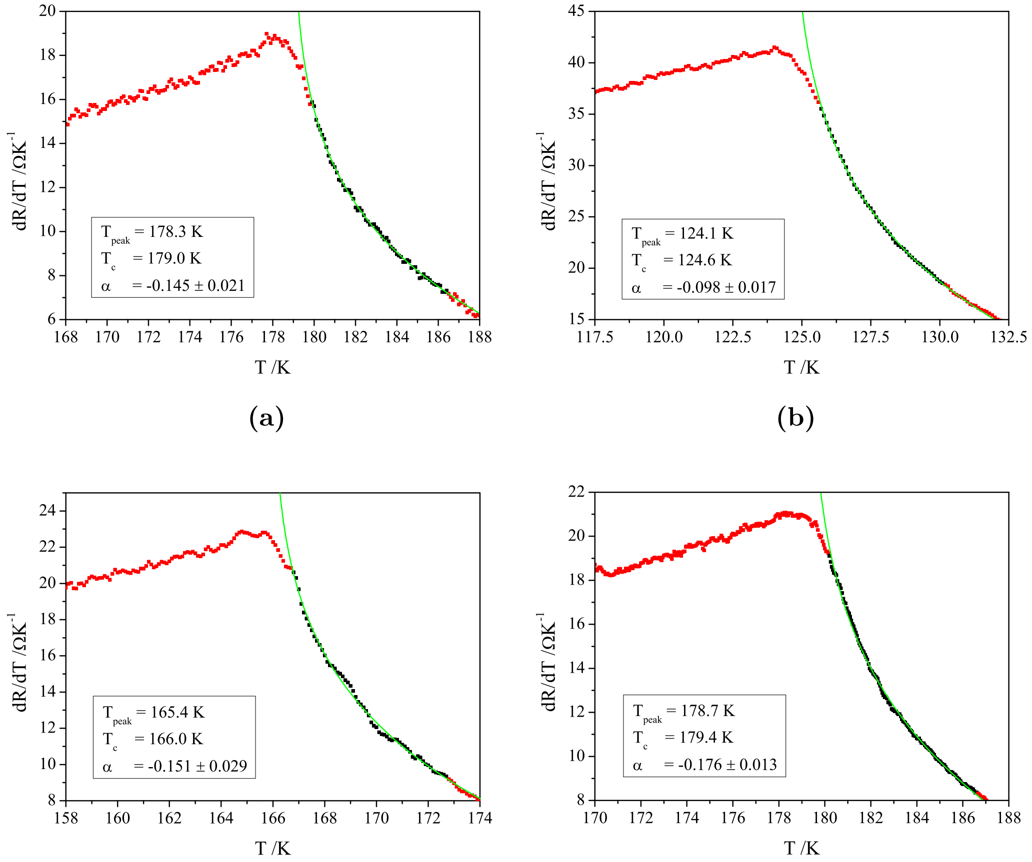

(a) **(b)**

(c) **(d)**

Figure 3.3.11: $\frac{\mathrm{d}R}{\mathrm{d}T}$ plots for samples (a) Mn160 (8%, 25 nm), (b) Mn330 (6%, 25 nm), (c) Mn437 (12%, 25 nm) and (d) the past Mn438 data (12%, 25 nm). Fitting was performed above the peak using equation (3.2.4).

increasing or reducing the Curie temperature by as little as 0.2 K resulted in α values approaching -0.3 similar to that seen within the Gaussian broadened plots in section 3.3.2. Opening T_c as a fitting parameter resulted in very high dependencies between parameters again similar to that seen in the previous samples.

Fitting is only shown for the region above T_c due to difficulties below caused by a flattening of the peak similar to that seen in Mn433_c. Fitting performed below T_c resulted in very strong dependencies between fitting parameters even with a fixed T_c due to the more linear nature of the curve and the larger relative noise. Resulting α values tended to be larger in magnitude than that expected with much higher associated errors. As with the fitting above the peak calculated exponent values varied significantly based on the fitting range and the parameter start conditions. Fixing the critical exponent to -0.13 lead to results similar to that seen for sample Mn438_c6 with the equation open enough to accommodate the change in α.

Such fits both above and below T_c clearly suggest the possibility of Heisenberg behaviour within (Ga,Mn)As, but in no way prove or disprove a particular model given the sensitivity to chosen parameters and fitting range. However, these fits do show that the $\frac{\mathrm{d}R}{\mathrm{d}T}$ critical behaviour is very similar across a range of annealed (Ga,Mn)As samples with a much more well defined peak than that of the resistance. Unfortunately, for these past samples the position of the peak cannot be compared to the actual Curie temperature due to system used, and the lack of Arrott plots.

3.4 Conclusions

This chapter has detailed a more thorough study of the transport behaviour close to T_c in (Ga,Mn)As performed on the same high Curie temperature samples measured in the critical phenomena work presented in chapter 2. Transport and magnetometry measurements performed within the same system confirmed the behaviour seen by Novák *et al.* (2008) with peaks in resistance predicting Curie temperature values more than 10 K higher than that measured via remanent magnetisation. In contrast the derivative $\frac{\mathrm{d}R}{\mathrm{d}T}$ displayed a sharp peak in both samples much closer to T_c. Figure 3.4.1 shows the magnetisation, resistance and $\frac{\mathrm{d}R}{\mathrm{d}T}$ datasets for sample Mn438_c6 and demonstrates the mismatch between the resistance peak and the magnetisation calculated Curie temperature.

Unfortunately, the critical behaviour of $\frac{\mathrm{d}R}{\mathrm{d}T}$ was found to be much more difficult to analyse than that of the magnetometry with calculated exponent values wildly different to any of the models covered in section 2.2.3. Calculated values were also very inconsistent between samples with no universal behaviour seen in past datasets.

One of the most likely causes of these disparities was the need to perform full function dataset fitting rather than the Kouvel-Fisher analysis used to

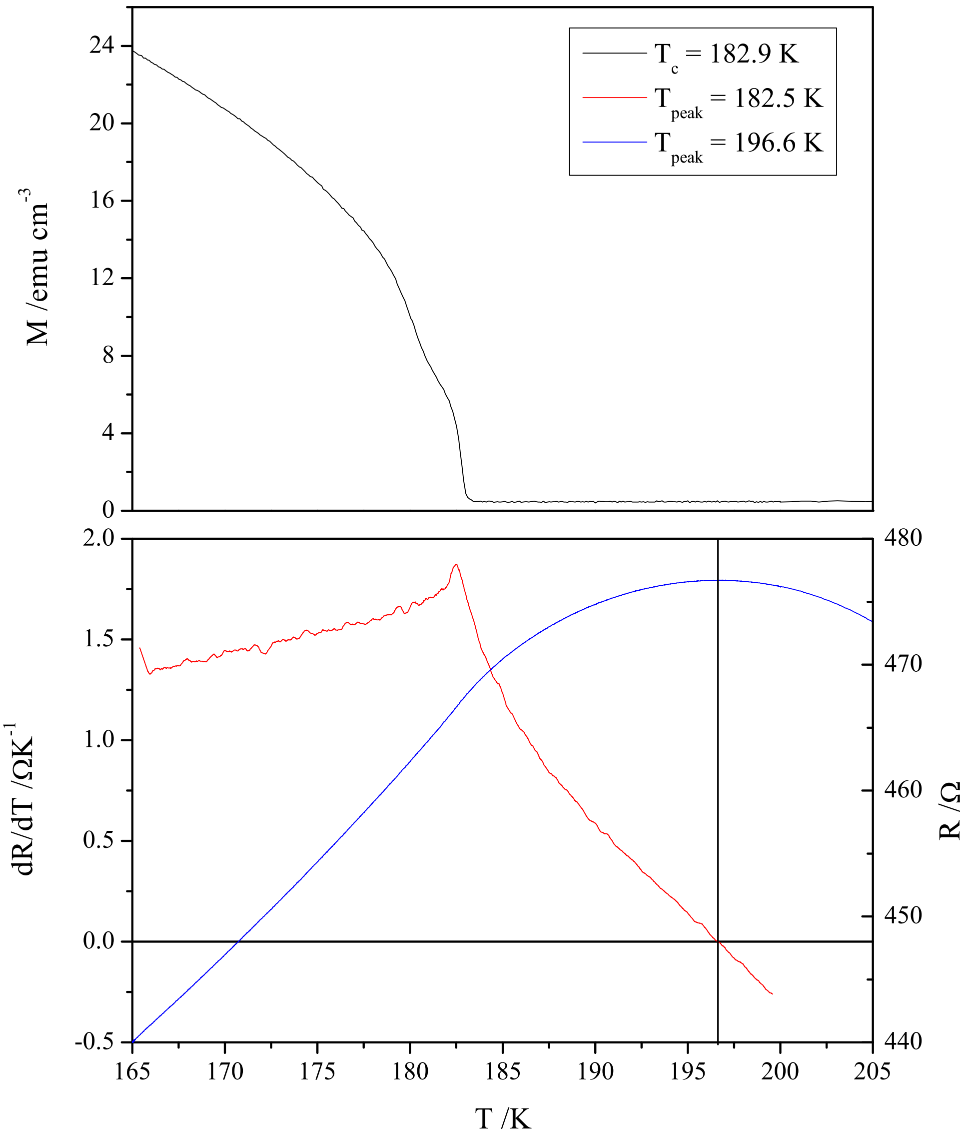

Figure 3.4.1: A comparison between the positions of the resistance (blue) and $\frac{\mathrm{d}R}{\mathrm{d}T}$ (red) peaks relative to the remanent magnetisation for sample Mn438_c6.

calculate β and γ. This method was not viable on $\frac{\mathrm{d}R}{\mathrm{d}T}$ both due to the double numerical differential required for analysis and the expected shifted-power-law behaviour of the specific heat 2.2.12. This resulted in unidentified T_c values and fitting with at least three open variables. Unknown T_c values lead to undefined fitting ranges with only slight changes in these resulting in very different calculated α exponents. These problems were further exaggerated by the very small differences between the Ising and Heisenberg theoretical curves, and the presence of peak broadening due to inhomogeneity.

Even with the open fitting of a four variable function, data appeared to show behaviour that was not power law-like, most notably above the peak in sample Mn438_c6. The main reason for this could be the unusual behaviour demonstrated by this sample's resistance at higher temperatures with a peak closer to that of an as-grown sample than an annealed one. A lot of these problems stem from the difficulties associated with performing the transport measurements within the SQUID system. Further work on this should therefore be focused on the re-measurement of the resistance using a more easily fabricated contact pattern structure, and a redesigned probe header to avoid problems with contact breakage.

References

Connelly, D. L., Loomis, J. S., and Mapother, D. E. 'Specific Heat of Nickel near the Curie Temperature'. *Physical Review B*, **3** (3) 924–934, (1971).

Craig, P. P., Goldburg, W. I., Kitchens, T. A., and Budnick, J. I. 'Transport properties at critical points: The resistivity of nickel'. *Physical Review Letters*, **19** (23) 1334–1337, (1967).

De Gennes, P. G. and Friedel, J. 'Anomalies de résistivité dans certains métaux magníques'. *Journal of Physics and Chemistry of Solids*, **4** 71–77, (1958).

Fisher, M. E. and Langer, J. S. 'Resistive Anomalies at Magnetic Critical Points'. *Physical Review Letters*, **20** (13) 665–668, (1968).

Greywall, D. S. and Ahlers, G. 'Second-Sound Velocity, Scaling, and Universality in He II under Pressure near the Superfluid Transition'. *Physical Review Letters*, **28** (19) 1251–1254, (1972).

Lederman, F. L., Salamon, M. B., and Shacklette, L. W. 'Experimental verification of scaling and test of the universality hypothesis from specific-heat data'. *Physical Review B*, **9** (7) 2981–2988, (1974).

Novák, V., Olejník, K., Wunderlich, J., Cukr, M., Výborný, K., Rushforth, A. W., Edmonds, K. W., Campion, R. P., Gallagher, B. L., Sinova, J., and Jungwirth, T. 'Curie Point Singularity in the Temperature Derivative of Resistivity in (Ga,Mn)As'. *Physical Review Letters*, **101** (7) 077201, (2008).

Priour, D. J. and Das Sarma, S. 'Critical behavior of diluted magnetic semiconductors: Apparent violation and eventual restoration of the Harris criterion for all regimes of disorder'. *Physical Review B*, **81** (22) 224403, (2010).

Shacklette, L. W. 'Specific heat and resistivity of iron near its Curie point'. *Physical Review B*, **9** 3789–3792, (1974).

Yuldashev, S. U., Igamberdiev, K. T., Lee, S., Kwon, Y., Kang, T. W., and Shashkov, A. G. 'Study of $Ga_{1-x}Mn_xAs$ Critical Behavior by Using Thermal Diffusivity'. *Journal of the Korean Physical Society*, **59** (2) 431–434, (2011).

Zumsteg, F. C. and Parks, R. D. 'Electrical Resistivity of Nickel Near the Curie Point'. *Physical Review Letters*, **24** (10) 520–524, (1970).

Chapter 4

Aharonov-Bohm Nanorings

4.1 Introduction

Chapter 1 has already discussed the potential future prospects of quantum-based devices as a motivation for spintronics research. Whilst this has yet to take off in everyday technology the concept of harnessing or observing quantum mechanical phenomena within real devices or structures is not a new one. As early as 1931 Paul Dirac (Dirac (1931)) proved that an electron wavefunction should acquire a phase shift when passing through a region of zero magnetic field, but non-zero magnetic vector potential. This was originally thought to have no effect on the electrons' behaviour. However, in 1959 Y. Aharonov and D. Bohm (Aharonov and Bohm (1959)) suggested a number of experiments involving the interference of such electrons based on the theoretical work of W. Ehrenberg and R. E. Siday (Ehrenberg and Siday (1949)).

Figure 4.1.1 shows one of their proposed set-ups in which a long solenoid is added to the standard double-slit experiment in the region between the slits out of the paths of the electrons. The predicted result was a shift in the expected interference pattern when the coil is turned on derived from the different phases acquired along each of the two paths. This was a surprising result: the magnetic field outside the solenoid should be zero, and yet passing electrons remain affected. This clearly demonstrates the importance of potentials within quantum mechanics as something more than simply a mathematical aid. The

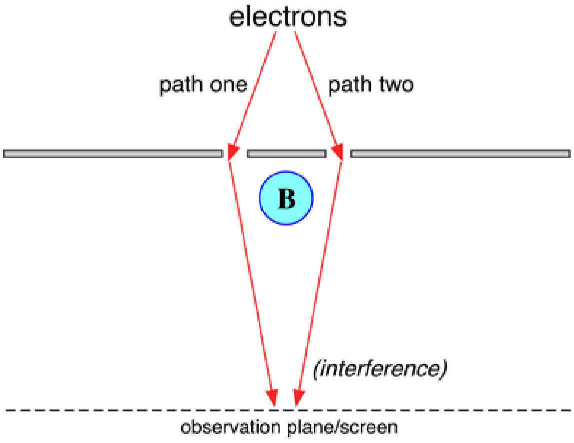

Figure 4.1.1: A solenoid is added between the two electron paths in the standard Young's double-slit set-up, and an interference pattern shown on the observation screen.

Aharonov-Bohm effect is essentially a quantum mechanical case of the Berry phase; related phenomena can also be seen in a number of areas in physics including that of superconductivity and optics.

These ideas were taken further by both Umbach *et al.* (1984) and Webb *et al.* (1985), who fabricated sub-micron diameter metallic rings to try to observe periodic $\frac{h}{e}$ oscillations in the magnetoresistance as predicted by the Aharonov-Bohm theory. The effect was then verified separately using a different approach involving superconductors by Osakabe *et al.* (1986). Similar results can also be seen involving the electric scalar potential (van Oudenaarden *et al.* (1998)) as well as an additional oscillation with period $\frac{h}{2e}$ as predicted by Al'tshuler *et al.* (1981).

The study of these magnetoresistance oscillations offers an insight into the quantum mechanical interference phenomena in a material with the magnitude related to the electron phase coherence length. This plays a crucial role in the understanding of quantum mechanical transport, and corrections to resistivity in different materials. Previous work on phase coherence in (Ga,Mn)As has been very limited despite it being an excellent system to study quantum corrections such as universal conductance fluctuations (UCF), weak localisation, and spin-orbit coupling.

Whilst both spin-disorder and spin-orbit scattering are expected to suppress these quantum corrections at temperatures approaching T_c it has been argued

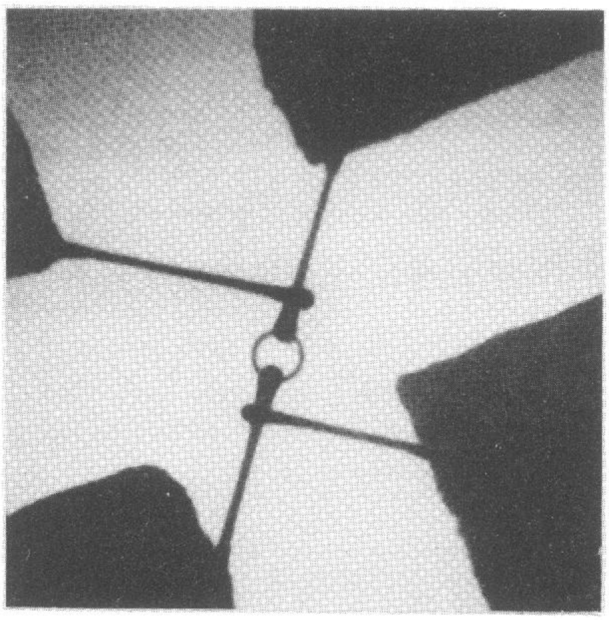

Figure 4.1.2: A transmission electron microscope image of a gold ring structure measured by Umbach *et al.* (1984) with an inside diameter of 280 nm and width 45 nm.

that in high quality metallic (Ga,Mn)As the phase coherence length could be relatively large at low temperatures Matsukura *et al.* (2004). This is because virtually all spins contribute to the ferromagnetic ordering thus reducing spin-scattering, giant splitting of the valence band makes both spin-disorder and spin-orbit scattering relatively inefficient, and strong magneto-crystalline anisotropies suppress magnon scattering. The few studies already performed on quantum interference effects within (Ga,Mn)As support this hypothesis with observations of UCF (Vila *et al.* (2007)) and evidence for Aharonov-Bohm oscillations (Wagner *et al.* (2006)) at millikelvin temperatures. Measurements performed in Regensburg (Wagner *et al.* (2006); Neumaier *et al.* (2008)) studied dephasing within (Ga,Mn)As nanowires and nanorings, and found the phase coherence length to be of the order 100 nm at millikelvin temperatures.

This chapter focuses on the fabrication of nanoring structures on highly optimised (Ga,Mn)As samples grown in Nottingham, and early test measurements on these devices with the future aim of conducting a full phase-coherence study. Low-temperature measurements were also performed within a dilution refrigerator on the first batch of structures fabricated in Nottingham. These demonstrated encouraging behaviour at higher cryostat temperatures, but had technical problems over the millikelvin range leading to results that were difficult to interpret. These results are therefore not presented within this chapter, but a brief summary is given within section 4.5 on the difficulties linked to these measurements, and the equipment optimisation performed in preparation for future work. A second fabrication method was developed in collaboration with the University of Glasgow guided by the processes developed in Nottingham in an effort to solve these problems. Unfortunately, the final study on these Glasgow-fabricated nanorings has not yet been performed due to time constraints.

The next two sections of this chapter cover the basic theory of both the Aharonov-Bohm effect and UCF as well as how the observation of the resulting oscillations in the magnetoresistance can be used to calculate a sample's phase coherence length. This is then followed by a more detailed look at the previous work on (Ga,Mn)As performed in Regensburg. The chapter then moves on to the process of Aharonov-Bohm ring fabrication in (Ga,Mn)As describing the difficulties involved when fabricating nanoscale rings, the testing performed to achieve high quality, reproducible structures, and the final adopted recipe. Most of the basic terminology, principles and methods discussed within this section are detailed in 1.4 as part of the introductory chapter. The remaining sections present basic preliminary measurements on the fabricated devices accompanied by details about future work on low-temperature phase-coherence studies.

4.2 Background Theory

4.2.1 Aharonov-Bohm Effect

The Aharonov-Bohm effect is one of the primary examples demonstrating the importance of the potentials in quantum mechanics. Within classical electrodynamics it is the fields that have physical significance with gauge transformations on potentials leaving the fields, and therefore the equations of motion, unchanged.

$$\boldsymbol{A} \longrightarrow \boldsymbol{A} + \nabla\chi(r,t) \tag{4.2.1}$$

Equation (4.2.1) shows a gauge transformation in which $\chi(r,t)$ is an arbitrary scalar function. By applying this transformation to the relation between the magnetic field $\boldsymbol{B}$ and the magnetic vector potential $\boldsymbol{A}$ it can be shown that if $\boldsymbol{B}$ is zero then $\boldsymbol{A}$ does not necessarily also have to be zero. This is simply based on the vector calculus identity that the curl of the gradient is always zero, and thus $\boldsymbol{A}$ can have a value of $\nabla\chi$(r,t) whilst still retaining $\boldsymbol{B} = 0$.

In quantum mechanics, particles exhibit wave-like properties governed by the Schrödinger equation.

$$i\hbar\frac{\mathrm{d}}{\mathrm{d}t}\Psi(r,t) = \left[\frac{1}{2m}\left(-i\hbar\nabla + e\boldsymbol{A}\right)^2 - e\Phi\right]\Psi(r,t) \qquad (4.2.2)$$

Equation (4.2.2) is the time-dependent Scrödinger equation for an electron in an external electromagnetic field. Based on this equation, in order to leave the theory invariant under the given gauge transformation an additional phase δ must be introduced to the wavefunction Ψ as shown below.

$$\Psi' = \Psi\exp\left(i\delta\right) \qquad \delta = -\frac{e}{\hbar}\chi(r,t) = -\frac{e}{\hbar}\int_l \boldsymbol{A}\bullet\mathrm{d}\boldsymbol{l} \qquad (4.2.3)$$

In most circumstances this additional phase is unnoticed, but in 1959 Aharonov and Bohm proposed a number of situations in which the effects could become significant. A solenoid is added to the well-known double-slit set-up, as shown in figure 4.1.1; the magnetic field within is non-zero, but zero everywhere else. From equation (4.2.3), each path taken by the electrons must gain a different change in phase when the solenoid is turned on, and therefore when both wavefunctions are recombined at the observation screen the result has a combination of the two phases.

$$\delta_2 - \delta_1 = \frac{e}{\hbar}\int_1 \boldsymbol{A}\bullet\mathrm{d}\boldsymbol{l} - \frac{e}{\hbar}\int_2 \boldsymbol{A}\bullet\mathrm{d}\boldsymbol{l} = \frac{e}{\hbar}\oint \boldsymbol{A}\bullet\mathrm{d}\boldsymbol{l} \qquad (4.2.4)$$

Stokes' theorem can then be applied to show that this difference in phase is proportional to the magnetic flux Φ_{m} within the solenoid.

$$\oint \boldsymbol{A}\bullet d\boldsymbol{l} = \int_S \nabla\times\boldsymbol{A}\bullet d\boldsymbol{S} = \int_S \boldsymbol{B}\bullet\mathrm{d}\boldsymbol{S} = \Phi_{\mathrm{m}} \qquad (4.2.5)$$

S = area enclosed by loop

The final result predicted is that the expected interference pattern should move periodically based on Φ_{m} within the solenoid with a period of the magnetic flux quantum $\Phi_0 = h/e$.

$$\Phi_m = \frac{h}{e}n \tag{4.2.6a}$$

$$\delta_2 - \delta_1 = \frac{e}{\hbar}\Phi_{\mathrm{m}} = 2\pi n \tag{4.2.6b}$$

(constructive interference occurs when $n = 0, \pm 1, \pm 2 \ldots$)

This effect was verified a year later for electrons propagating in free space (Chambers (1960)), but it was originally thought that it would not be observed in material ring structures. It was not known if there would be phase coherence of an electron during its diffusive motion within a metallic or semiconducting sample. When passing through a material electrons follow a diffusive path dictated by interactions with other electrons, impurities or phonons. Both electron and non-magnetic impurity scattering are elastic processes that result in no change in phase. However, phase coherence can be broken by inelastic phonon scattering with magnetic impurities such as spin-flip or spin-orbit interactions that result in a change in spin.

The average distance travelled by an electron before it suffers a phase changing interaction is called the phase coherence length L_ϕ. This is related to both the elastic L_{el} and inelastic L_{in} mean free paths where typically $L_{\mathrm{el}} < L_\phi < L_{\mathrm{in}}$.

$$L_\phi = \sqrt{L_{\mathrm{el}} L_{\mathrm{in}}} \tag{4.2.7}$$

Oscillatory behaviour can therefore be observed in the conductance of mesoscopic rings with diameters approaching the sample coherence length with a period ΔB.

$$\Delta B = \frac{\Phi_0}{\pi r^2} \tag{4.2.8}$$

r = ring radius

From equation 4.2.7 it can be seen that higher temperatures lead to a reduction in the phase coherence length due to an increase in phonon scattering and spin-flip interactions. An increase in temperature can also destroy phase coherence via thermal broadening around the Fermi surface leading to a spectrum of electron energies $E_{\mathrm{F}} \pm k_{\mathrm{B}}T$. This results in electrons moving out-of-phase on average after a diffusion length L_{T} referred to as the thermal length.

$$L_{\mathrm{T}} = \sqrt{\hbar D / k_{\mathrm{B}}T} \tag{4.2.9}$$

Oscillations are therefore damped both in larger rings and at higher temperatures due to an exponential reduction in the number of coherent electrons passing across the ring. This leads to a drop-off in the amplitude ΔG related to the phase coherence length (Washburn and Webb (1986)) as shown by equation (4.2.10).

$$\Delta G = \frac{e^2}{h}\frac{L_{\mathrm{T}}}{L_{\phi}}\exp(-\pi r / L_{\phi}) \tag{4.2.10}$$

This allows L_{ϕ} to be calculated from low-temperature conductance measurements for samples of known thermal diffusion length.

For the (Ga,Mn)As grown in Nottingham the thermal diffusion length is expected to be comparable to the phase coherence length at 50 mK. Based on the previous work by Neumaier *et al.* (2008) detailed in section 4.3 the phase coherence length at this temperature should be of-the-order 150 nm. Aharonov-Bohm oscillations are therefore expected to be observed in (Ga,Mn)As rings of diameter less than 200 nm with an amplitude damping given by equation (4.2.10).

The nanoring structures fabricated for this chapter had outer diameters ranging from 130 nm to 300 nm with track widths of roughly 20 nm. As a result of this finite width a range of oscillation periods are expected due to a smearing of the interference pattern. Table 4.1 shows the expected oscillation periods ΔB and amplitude damping factors ΔG for 130 nm, 150 nm and 200 nm nanorings calculated from equations (4.2.8) and (4.2.10) respectively. Each are given as a range between the inner and outer diameters using a phase coherence length of 150 nm and a thermal diffusion length of 200 nm. It should be noted that it is the inner diameter that results in the larger oscillations, and that the conductances amplitudes are given as unitless quantities with the absolute values calculated by multiplying by $\frac{e^2}{h} = 41.56\,\mu\mathrm{S}$.

Outer diameter /nm	ΔB /T	ΔG
130	$0.31 \rightarrow 0.65$	$0.34 \rightarrow 0.52$
150	$0.23 \rightarrow 0.44$	$0.28 \rightarrow 0.42$
200	$0.13 \rightarrow 0.21$	$0.16 \rightarrow 0.25$

Table 4.1: Aharonov-Bohm oscillation periods ΔB and amplitudes ΔG calculated from equations (4.2.8) and (4.2.10) respectively for 130 nm, 150 nm and 200 nm (Ga,Mn)As nanorings with $L_\phi = 150$ nm and $L_\mathrm{T} = 200$ nm.

4.2.2 Universal Conductance Fluctuations

Another observable effect of the quantum coherence of electrons that cannot be neglected in the (Ga,Mn)As nanoring structures are universal conductance fluctuations. These are sample-specific aperiodic fluctuations that are a random function of the applied magnetic field, carrier concentration and impurity configuration. However, unlike noise, they are not random in time, but reproducible upon performing the same magnetic field or gate voltage sweep at a given temperature. When viewed from a purely semiclassical theory of transport these fluctuations are anomalously large. For mesoscopic structures with $L \leq L_\phi$ the conductance varies from sample to sample, but the root-mean-square fluctuation

$$\Delta G \equiv \sqrt{\left\langle (G - \langle G \rangle)^2 \right\rangle} \tag{4.2.11}$$

takes a universal value of $\frac{e^2}{h}$ at sufficiently low temperatures independant of sample size and impurity configuration. This universal behaviour is a result of interference between the various paths that an electron can take when traversing a sample. A theoretical treatment of this was first established using pertubation theory by Al'tshuler (1985) and independently by Lee and Stone (1985).

Within a sample the conductance is related to the probability of an electron travelling from one contact to the other per unit time. The probability of transmission in a time t is found by summing over all possible paths connecting the two contacts.

$$P(r_1, r_2, t) = \left| \sum_i A_i \right|^2 = \sum_i |A_i|^2 + \sum_{i \neq j} A_i A_j^* \tag{4.2.12}$$

Equation 4.2.12 shows this summation split into two seperate terms where A_i is the probability amplitude of the ith path connecting points r_1 and r_2 within a time t. The first term corresponds to the classical picture of electron diffusion between the contacts in which the average conductance attributable to disorder scattering is given reasonably accurately by Boltzmann theory. The second term then considers the quantum interference between the different trajectories. One might expect this term to self-average to zero when summing over a very large number of paths as a result of the random nature of the phase relationship between A_i and A_j. However, this is not the case in small systems, comparable in size to L_ϕ.

It is this quantum mechanical term that gives rise to a reproducible dependence of the conductance on applied magnetic field or gate voltage. Both result in a change in the phase difference between paths and therefore the interference, the first by inducing a phase shift in the electron wavefunctions as shown in the previous section, and the second by changing the effective impurity configuration and therefore the paths taken by the electrons. As the magnetic field or gate voltage is swept the quantum mechincal term fluctuates thus resulting in fluctuations in G.

At absolute zero within systems in which $L \leq L_\phi$ the amplitude of these fluctuations takes a universal value. However, as is the case with Aharonov-Bohm oscillations, at finite temperatures the combined effects of thermal broadening and phonon scattering lead to decoherence once the system size L exceeds the dephasing length L_{min}. This results in a damping of UCF dependent on the relative sizes of L_ϕ, L_{T} and L that takes the form of a power-law attenuation derived from two factors: L_ϕ/L and L_{T}/L_ϕ.

In two- and three-dimensions, systems behave as a classical network of resistors consisting of coherent regions L_{min}^d in size where d is the dimensionality of the system. Both factors therefore take an exponent value of $\frac{4-d}{2}$ resulting in a root-mean-square fluctuation summarised by (4.2.13) where L_{min} is the shorter of L_ϕ, L_{T}.

$$\Delta G \propto \left(\frac{L_{\mathrm{min}}}{L}\right)^{\frac{4-d}{2}} \tag{4.2.13}$$

Within one-dimensional systems, such as the (Ga,Mn)As nanoring structures, the behaviour is more complex with the factor due to thermal broadening scaling with an exponent of 1 rather than 3/2 (Lee *et al.* (1987)). The attenuation in one-dimensional systems for different temperature regimes are shown by (4.2.14).

$$\Delta G \propto \left(\frac{L_\phi}{L}\right)^{\frac{3}{2}} \qquad \text{for } L_\phi < L_T, L \tag{4.2.14a}$$

$$\Delta G \propto \left(\frac{L_\phi}{L}\right)^{\frac{3}{2}} \left(\frac{L_\mathrm{T}}{L_\phi}\right) = \left(\frac{L_\mathrm{T}}{L}\right)\left(\frac{L_\phi}{L}\right)^{\frac{1}{2}} \qquad \text{for } L_\mathrm{T} < L_\phi < L \tag{4.2.14b}$$

$$\Delta G \propto \left(\frac{L_\mathrm{T}}{L}\right) \qquad \text{for } L_\mathrm{T} < L < L_\phi \tag{4.2.14c}$$

Within nanoring structures UCF are expected to be superimposed on top of the Aharonov-Bohm oscillations potentially making analysis more difficult. The effects of UCF are therefore undesirable in the context of the (Ga,Mn)As nanoring studies presented within this chapter. Given the expected phase coherence and thermal diffusion lengths, fluctuations should have a root-mean-square amplitude of

$$\Delta G = C\frac{e^2}{h}\left(\frac{L_\phi}{L}\right)^{\frac{3}{2}} \tag{4.2.15}$$

derived from equation (4.2.14a) where $L_\phi < L_T$. An additional constant of proportionality C has been introduced that is close to unity, and depends on the spin-orbit interaction strength and the applied magnetic field with larger fields resulting in smaller fluctuations.

Theory also predicts the maximum scale of these fluctuations at finite temperatures within one-, two- and three-dimensional systems (Lee *et al.* (1987)). In the case of a one-dimensional system this magnetic field correlation length B_c is dependent solely on the width W of the system and the dephasing length L_min.

$$B_\mathrm{c}(T) = \frac{\Phi_0}{L_\mathrm{min}W} \tag{4.2.16}$$

The correlation field is therefore expected to be the same for all nanoring diameters with equation (4.2.16) predicting a value of 1.38 T for structures with a width of 20 nm.

Outer diameter /nm	ΔG
130	$0.63 \rightarrow 1$
150	$0.51 \rightarrow 0.81$
200	$0.33 \rightarrow 0.46$

Table 4.2: UCF amplitudes ΔG for 130 nm, 150 nm and 200 nm (Ga,Mn)As nanorings with $L_\phi = 150\,\text{nm}$ and $L_\text{T} = 200\,\text{nm}$.

Table 4.2 shows the expected root-mean-square amplitude of UCF within the 130 nm, 150 nm and 200 nm (Ga,Mn)As nanorings based on equation (4.2.15) assuming $C = 1$. These are given as unitless quantities with the absolute values calculated by multiplying by $\frac{e^2}{h} = 41.56\,\mu\text{S}$.

4.3 Previous Work

Whilst phase coherence phenomena such as UCFs and weak localisation have been observed within (Ga,Mn)As in the past the Aharonov-Bohm effect remains largely unexplored with only a single group based in Regensburg (Wagner *et al.* (2006); Neumaier *et al.* (2008)) having performed focused studies. The group presented measurements on both nanoring and nanowire structures with evidence for both large UCFs and Aharonov-Bohm oscillations. This data was used to calculate the phase coherence length and temperature dependence of dephasing.

Within the original paper conductance measurements were only performed on nanostructures fabricated on low T_c as-grown samples with manganese concentrations of only 2% Mn. A study of the observed UCFs within nanowires estimated the phase coherence length to be roughly 100 nm; however, measurements on a 100 nm diameter nanoring did not display clear periodic oscillations. Fourier transforms of the behaviour showed a broad spectrum of magnetic field frequencies with only a very poorly defined peak over the expected $\frac{h}{e}$ range.

The second paper included additional data taken from much higher 6% annealed samples with Curie temperatures of around 100 K. Nanorings of average diameters 150 nm and 190 nm displayed more periodic oscillations than that of the as-grown samples with relatively broad Fourier peaks within the expected $\frac{h}{e}$ ranges. Both UCF and Aharonov-Bohm measurements again demonstrated phase coherence lengths of between 100 nm and 200 nm at millikelvin temperatures. However, these figures were only approximately calculated with the UCF value partially based on fitting to weak localisation behaviour and the thermal diffusion length taken as an approximate value between 120 nm and 200 nm.

The group concluded that the initial difficulties with Aharonov-Bohm observations resulted from both the superposition of aperiodic UCFs with similar magnetic field scales, and the finite width of the ring which causes an uncertainty in the expected oscillations. Despite these problems the phase coherence length was calculated and shown to follow a $T^{-1/2}$ temperature dependence. Based on this weak temperature dependence the group suggested that the primary source of phase breaking comes from hole-hole scattering following on from the work of Lee and Ramakrishnan (1985) within disordered conductors. Manganese interstitials were found not to cause dephasing with the increase of L_ϕ after low-temperature annealing put down to an increase in the diffusion constant with the corresponding dephasing time remaining unchanged.

Whilst this work has shown that (Ga,Mn)As can have relatively large phase coherence lengths at low temperatures many questions still remain regarding quantum corrections, and their significance in (Ga,Mn)As. Both the calculated phase coherence length, and dephasing temperature dependence should be treated with some caution based on the approximate methods of calculation and the marginal dimensionality of the studied structures relative to the estimated thermal diffusion lengths. Work on Nottingham grown samples could expand on these studies offering further insight into phase related phenomena due to the potential for longer phase coherence lengths and much thinner high quality samples. Annealed samples studied in Regensburg demonstrated clearer periodic oscillations than their as-grown counterparts, but still displayed conductances appreciably lower than equivalent Nottingham-grown samples

Although this work does not offer a complete picture it does expose a number of problems that need to be considered in future studies. The most prominent of these are the effects of a finite track width and the addition of aperiodic UCFs at low temperatures. The first of these in particular is not resolved by sample quality, and is effectively unavoidable in nanoring structures due to the resolution limits of current fabrication processing techniques. One should therefore always expect to observe a broadening of the possible oscillation periods due to a variation in potential path lengths around the loop.

4.4 Nanoring Fabrication

In order to perform phase-coherence studies, structures first needed to be fabricated in (Ga,Mn)As substrates. The main aim of this section is therefore to give a summary of some of the difficulties posed during processing, and the testing and optimisation required to overcome these problems. Prior to this work some progress had already been made in this field in Nottingham by Dr. Ehsan Ahmad. The work detailed within this section is therefore loosely based on Ehsan's early testing; however, a great deal of further development was still required for high quality, reproducible contacted nanoring fabrication.

It must also be noted that whilst this work was primarily based on that carried out by Ehsan other people were also involved in various stages of fabrication. The (Ga,Mn)As wafers were all grown via MBE by Dr. Richard Campion, the contact deposition and bonding carried out by Dave Taylor, and the reactive ion etching performed with the assistance of Dr. Chris Mellor, all of the University of Nottingham. The observation of Aharonov-Bohm oscillations in (Ga,Mn)As requires nanorings with an outer diameter of less than 150 nm, and a width approaching 20 nm to 30 nm. Whilst a standard EBL system is more than capable of providing such a high resolution the fact that the exposed resist was to be used for etching severely limited the resist options. This choice was further restricted by the need for a negative tone resist in order to create a high quality mask without the need to expose everything other than the ring structure itself. The required ring width also restricted etching to that of dry only due to the need for very high anisotropy to avoid undercut structure collapse.

The most convenient resist choice, and therefore that used in the nanoring fabrication, was the cross-link approach of PMMA. Unfortunately, this overexposure method of PMMA is not widely used in nanofabrication partly due to a poor etch resistance, but mostly because the resulting mask is hard to remove without damaging the underlying material. Both these problems therefore needed to be solved and a lot of optimisation carried out before the final fabrication.

Rigorous dose and etch testing was performed along with many revisions of the pattern design in an effort to achieve high quality, reproducible ring structures. The next subsection describes some of the more significant testing carried out along with brief comments on some of the lesser problems also encountered. The final subsection then brings this all back together again by detailing the final adopted fabrication procedure.

4.4.1 Preliminary Testing

Initial work on the nanoring fabrication was performed by Ehsan Ahmad, and it is his work that is the basis for the testing detailed in this section. His original designs were written on 30 nm thick A2 950 PMMA in five separate 5 μm writefields: four containing the outer contacts, and one containing the inner contacts and the ring itself. Unfortunately, this design resulted in difficulties in writefield stitching leading to unwanted gaps between the ring and contacts. RIE testing of this exposure set-up on 25 nm (Ga,Mn)As chips also demonstrated that it was not possible to define the ring with such a thin layer of resist.

Exposure Testing

With both of these problems in mind a new design was created in a single larger writefield of 50 μm consisting of a 150 nm diameter ring and four contacts each split into inner and outer sections. The outer contacts with a constant width of 1.7 μm, and the inner contacts with a gradually reducing width down to 20 nm at the ring. This tapering contact design was used to avoid ring distortion and breaks at the ring caused by excessive charge build-up. The whole design was written in the pattern file line by line with 10 nm spacing affording greater control over the exact movements of the beam and the exposure order.

Optimisation of this original design was carried out by repeated array exposures varying the dose of each area, the exposure order and beam path. Exposure

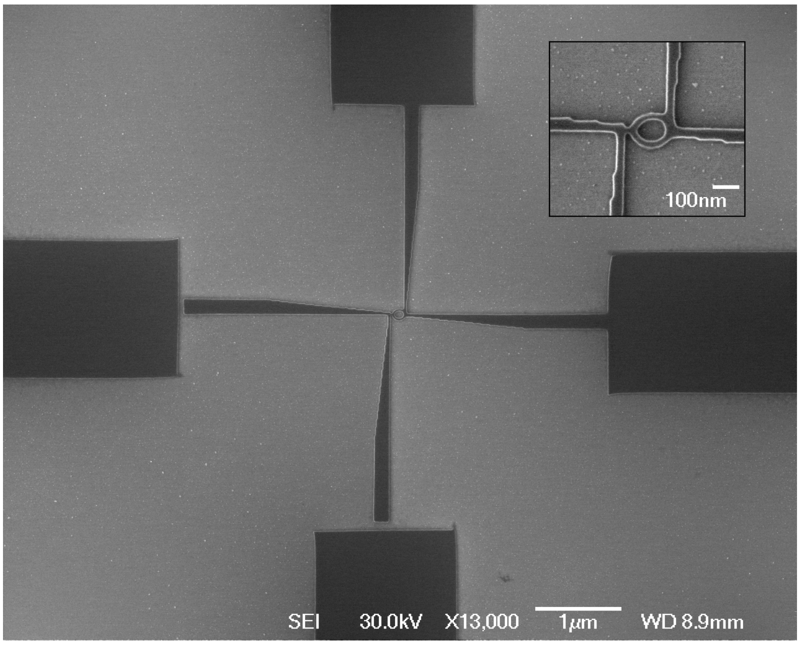

Figure 4.4.1: An SEM image taken of sample Mn245_01 demonstrating the importance of both pattern design and exposure order. The top right inset of the ring at the centre also shows slight signs of contact misalignment, something again solved by exposure re-ordering and changing the beam path.

doses were varied from 15 nCcm^{-1} to 35 nCcm^{-1} equivalent to between 50 and 100 times that of a standard PMMA exposure. Early exposures still resulted in gaps in the contacts as seen in the previous work with separate writefields; an example of this is shown in figure 4.4.1.

In this example the outer contacts were written in an anticlockwise order from the right. The increasing gap size as the exposure progresses suggests that they could be caused by charge build up on the resist surface due to the high exposure doses. This effect was removed from the final design by adjusting the exposure order and beam path, and adding a slight overlap. Writing each contact as a whole rather than two inner and outer sections resulted in breaks at the ring and deformation of its shape.

After further dose optimisation, exposures were also made of both 100 nm and 130 nm diameter rings using the same basic contact design and dose assignment. From these exposures it was possible to see that whilst 100 nm might be possible a 130 nm design would offer significantly greater fabrication success rate and

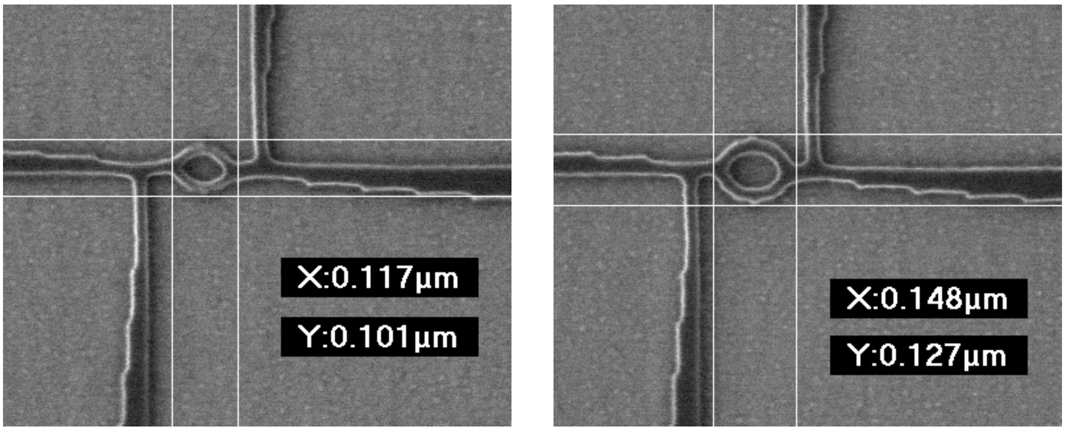

Figure 4.4.2: SEM images of both 100 nm and 130 nm diameter ring exposures with both the height and width shown. In both cases the rings appear slightly elongated.

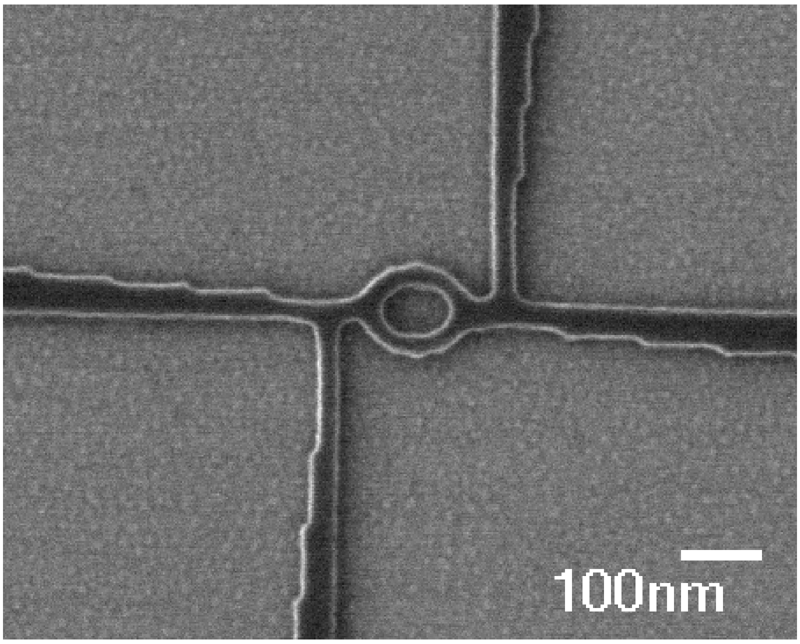

Figure 4.4.3: An SEM image of the inner contacts and ring of a fully optimised 130 nm diameter exposure. The nanoring itself was exposed first with areas close to the contacts at 30 nCcm^{-1} and areas on top and bottom at 35 nCcm^{-1}. This was followed by the inner then outer contacts at 25 and 15 nCcm^{-1} respectively.

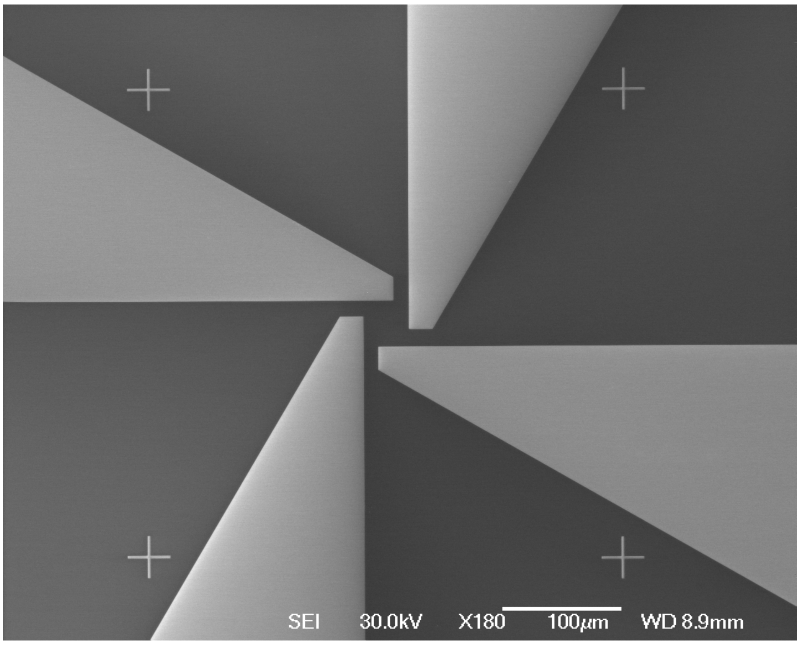

Figure 4.4.4: An SEM image of an EBL gold contacts exposure.

more sharply defined inner ring edges. Figures 4.4.2 and 4.4.3 show examples of varying ring diameter and a fully optimised exposure respectively.

With the central ring exposure finalised the next stage was to modify the gold contacts pattern for this new design and try to improve the possible margins for error when aligning to the ring contacts. During his original testing, EBL was used with a bilayer resist of A5 495 and A2 950 PMMA spun separately; a process that took well over five hours and involved the use of very large writefields up to 1000 μm. Given the difficulties this imposed on the fabrication the new pattern design was created first as an EBL pattern file for testing, and then the finalised layout drawn and ordered as a photolithography mask.

Figure 4.4.4 shows an EBL exposure of the new gold contacts design performed using bilayer PMMA with an exposure dose of 250 μCcm^{-2}. Each of the contacts are arranged such that the overlap to the central ring contacts is perpendicular rather than parallel, and the square at the centre reduced to 36 μm in comparison to the 50 μm of the ring exposure. Such a design allows for a greater spatial or rotational misalignment of the layers without losing overlap.

Etch Testing

Having optimised both exposure processes the next test required for the fabrication was that of etching. As with the previous optimisation these tests were based on Ehsan's original work in which he reactive ion etched (Ga,Mn)As using a combination of $SiCl_4$ and SF_6, and then measured the etch depths using an atomic force microscope (AFM). These original tests showed that 25 nm thick nanorings could not be fabricated due to the poor RIE resistance of the PMMA even after overexposure. Etch rates of the resist were similar to that of the (Ga,Mn)As, and thus difficulties were found with the 30 nm thick resist.

Unfortunately, simply increasing the resist thickness was not a possibility due to the associated decrease in exposure resolution. With this in mind thinner (Ga,Mn)As layers were specified to Richard Campion with a thickness of 10 nm: the minimum thickness possible without a large increase in sample resistivity at low temperatures and a general decrease in overall sample quality.

Exposures of the finalised nanoring design were made on 5 mm x 5 mm 6% (Ga,Mn)As substrates, and RIE testing carried out with the aid of Chris Mellor over a number of etch times between 15 s and 35 s using the same base gases. After the etch process the overexposed PMMA was removed by two minute oxygen plasma exposures allowing the etch depth of the substrate to be measured directly via AFM.

SEM imaging of the etch-tested rings, as shown in figure 4.4.5, showed that etch times of more than 20 seconds were not suitable for the nanoring fabrication. Whilst the RIE method is highly anisotropic there is still a small amount of lateral etching that is enough to cause an undercut leading to ring and inner contacts collapse. The rings were, however, reasonably well defined in the 15 s and 20 s samples, but in order for them to be truly isolated the etch depth needed be more than 10 nm.

Etch depth measurements of these samples were carried out via the use of AFM imaging and profiling. Initial imaging proved difficult partly due to the height and size of the rings, and partly because of the required precision set-up of the system. Unfortunately, early measurements resulted in damage to some of the

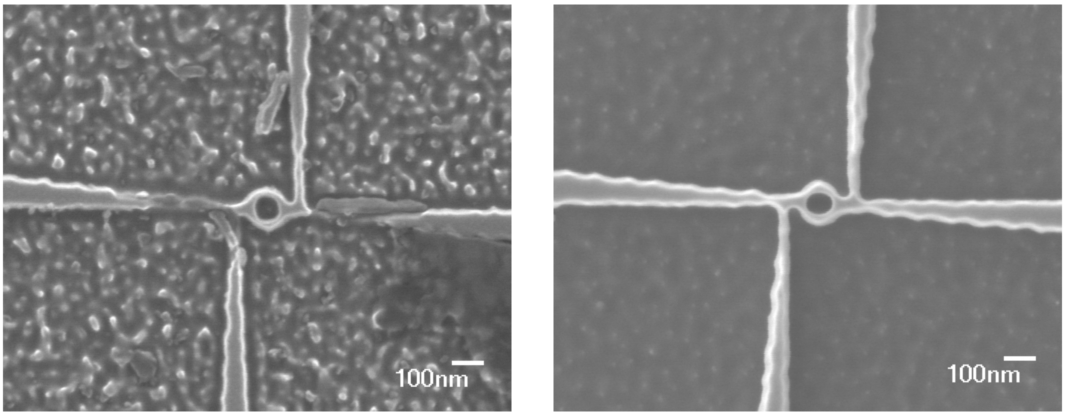

(a) 15 seconds **(b)** 20 seconds

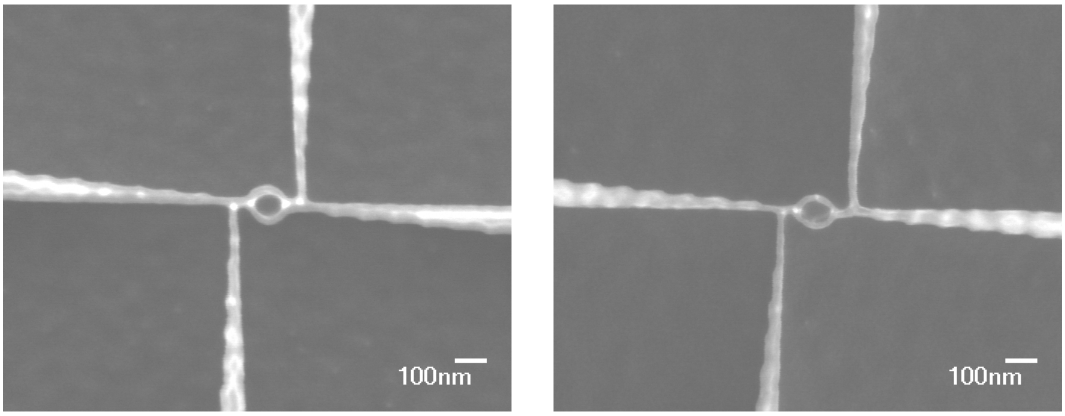

(c) 25 seconds **(d)** 30 seconds

Figure 4.4.5: SEM images of the RIE etch test rings taken after both PMMA removal and AFM profiling. The damage of the 15 s etch inner contacts shown in (a) was caused by difficulties with AFM rather than the etch process itself and should therefore not be a problem during final fabrication.

imaged structures due to a low voltage set point leading to a tip collision with the surface. Once set up correctly, however, full images were taken of the 15 s and 20 s etched rings, and etch depths measured for all samples.

As shown in table 4.3 the depths were found to be considerably more than that by Ehsan. The most probable cause of this was an increased etch rate of the GaAs substrate to that of the (Ga,Mn)As. Previous RIE showed that higher nominal concentrations of manganese generally led to lower etch rates. For the 25 nm samples an etch time of roughly 25 seconds was enough to remove most of the overexposed resist, but not enough to etch through the (Ga,Mn)As film.

Etch Time /s	**Depth, 25 nm /nm**	**Depth, 10 nm /nm**
15	17	60
20	20	105
25	23	170
30	24	250
35	-	300

Table 4.3: Etch depths measured via AFM for both 25 nm and 10 nm (Ga,Mn)As samples.

Thus after this point the measured depth remained almost constant with a dramatic increase in etch rate expected at higher etch times once the GaAs is reached.

For the 10 nm samples this point was reached much more quickly before all the resist had been removed resulting in the greater measured depth seen over the original tests. Unfortunately, whilst this does mean that the required depth is reached relatively easily, etching for too long significantly increases the undercut potentially causing a collapse of the finer structure areas such as the ring itself. Whilst the ring appears well defined in 4.4.5b, even for an etch time of 20 seconds the etch depth at the centre is more than that at the larger contacts. This could imply that at this point the central structure has already partially collapsed, for this reason, and the fact that even shorter etch times could pose a problem, a 15 second etch time was chosen for final device fabrication.

Figures 4.4.6 and 4.4.7 show an AFM image of the 15 second etched sample and a surface profile across the ring respectively. The profile shows that the surface of the substrate over the etched areas is quite rough close to the structure. However, the ring itself is clearly visible, but with dimensions noticeably larger than that viewed in the SEM. One possible reason for this is a slight deformation of the tip shape; broken or damaged tips, such as that after collision with the inner contacts in 4.4.6, can lead to two scan points and therefore a double image that is not always apparent. Such a problem would also explain the shape of the left edges with respect to the right. These appear to be more vertical and have a far better definition. What is crucial about the ring is that the etch depth even in the central hole is between 50 and 60 nm, considerably more than the measured substrate roughness and 10 nm (Ga,Mn)As thickness.

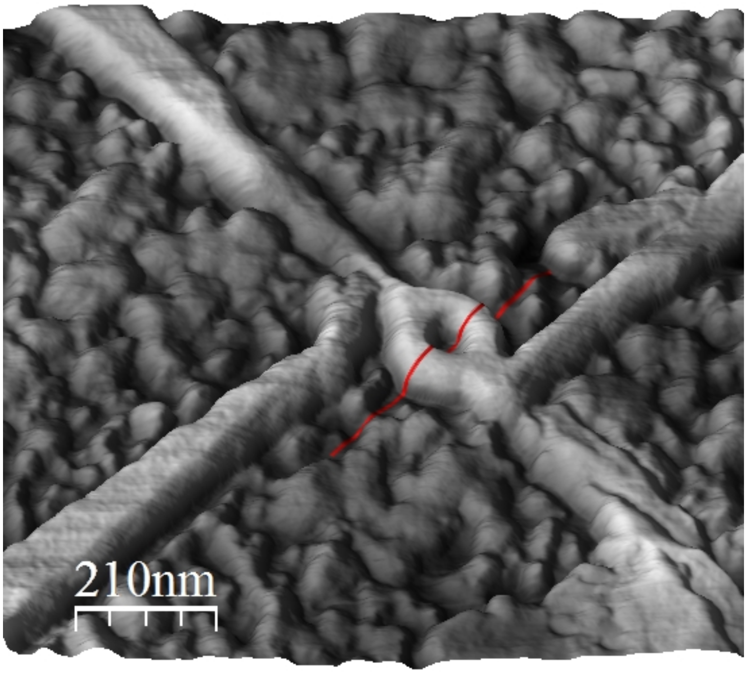

Figure 4.4.6: A 1 μm x 1 μm three-dimensional AFM image of a 15 s etched structure taken at 45°C with a set point of 700 mV and a gain of 25 V.

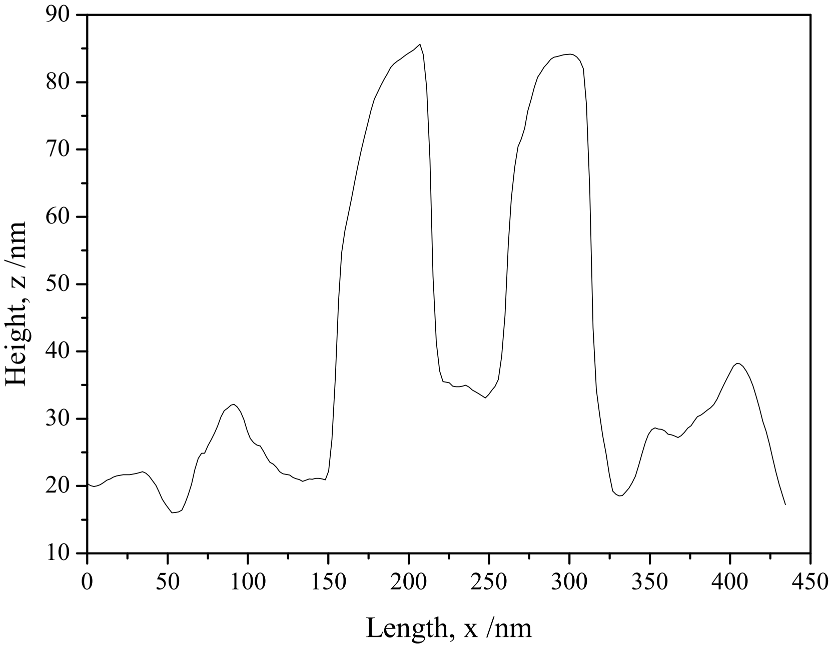

Figure 4.4.7: An AFM image profile along the red line shown in figure 4.4.6 from left to right.

4.4.2 Final Recipe

With optimisation and testing carried out for all of the fabrication stages as well as imaging of all of the resulting structures, the final fabrication process chosen consisted of two exposures. During the initial testing and for the first set of structures both stages were EBL-based. However, for the final samples the first was changed to a photolithographic exposure in order to avoid the use of large writefields and to reduce fabrication time. This was used to lay down gold contact pads and alignment marks via metallisation, and the second, an EBL exposure, to define the inner contacts and rings using RIE. This approach of laying the contacts first was taken so that the gold could effectively be used as a second mask for the etch step and allowed a greater freedom for any potential misalignment. The full device fabrication procedure is summarised below; four structures are fabricated together with a total production time of roughly two to three days. A total of five sets of four structures of varying ring diameter were fabricated for measurement.

First layer processing

The first stage in the fabrication process was to prepare the (Ga,Mn)As, this was done by scribing GaAs wafer with a 10 nm layer of (Ga,Mn)As 6% Mn grown on it into six 9.7 mm x 9.7 mm substrates. Each of these substrates led to a fabrication of four nanoring structures with different contact layout orientations. Cleaning was performed using ethyl lactate, acetone, methanol and IPA for 10 minutes each along with 1 minute in an ultrasonic bath. Each were then dried using an N_2 gun and dehydrated in an oven prebake at 180°C for 15 minutes to remove any remaining unwanted surface residue.

The next step after cleaning was the lithography; this was initially carried out via EBL using a bilayer resist of A5 495 PMMA and A2 950 PMMA following a similar procedure to that of Ehsan using 500 μm writefields with a uniform dose of 250 μCcm^{-2}. For the final structures, however, substrates were spun with BPRS-150 photoresist for 30 s at 5 krpm using a spin coater and disposable pipette. A hotplate was then used to remove the resist solvent by baking for 5 minutes at 100°C. This led to an even resist coverage of roughly 1.5 μm at the centre as measured via a Dektak stylus profiler during testing.

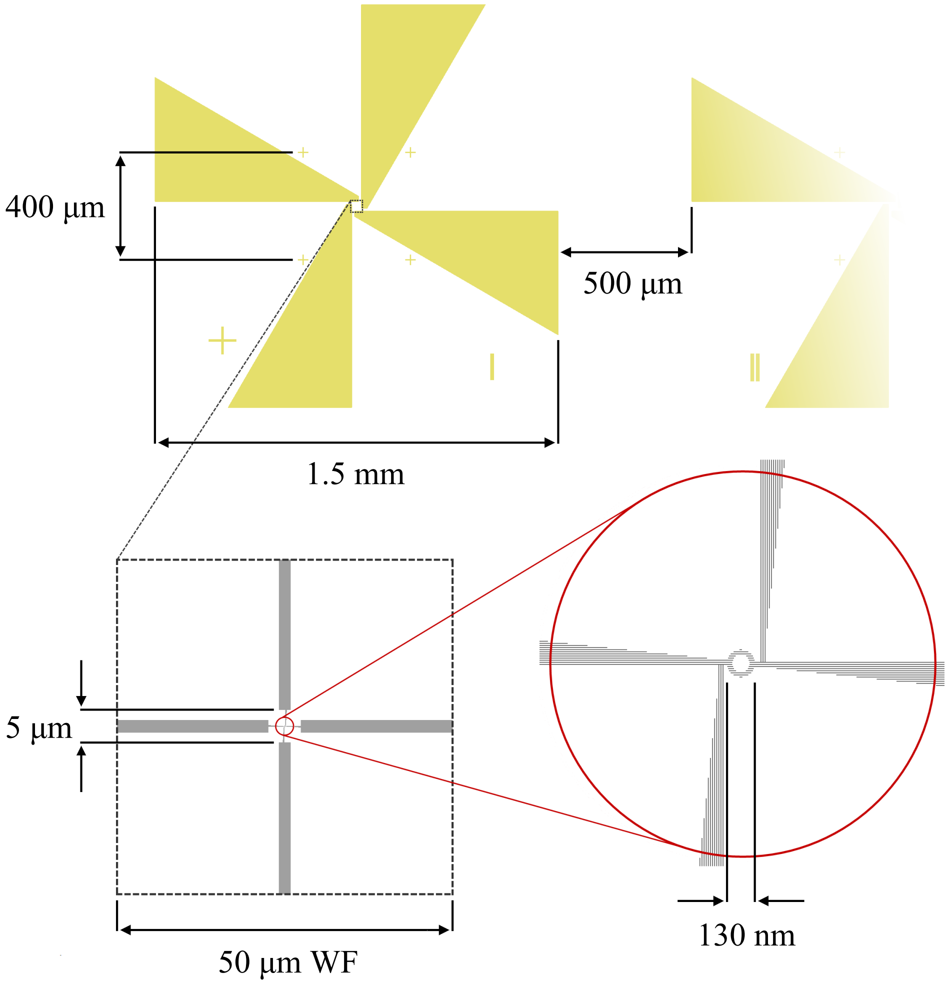

Figure 4.4.8: A schematic diagram of both the final gold contacts design and the nanoring EBL exposure. The gold contacts shown at the top were exposed in groups of four with a central square of 36 μm resulting in a perpendicular overlap of 7 μm with each nanoring contact. The nanoring and internal contacts were all performed in 50 μm writefields via individual line writing as shown at the bottom. The vertical inner contact positions were tailored to the nanoring diameter which ranged from 130 nm up to 250 nm; this diagram shows the 130 nm design.

Photolithography was carried out using a SÜSS MicroTec mask aligner and a chrome on soda-lime glass mask with an exposure time of 6.5 s. Samples were then developed in a mixture of 20 ml BPRS developer and 70 ml water for 50 s before being profiled and viewed under optical microscope for defects.

Finally, the contact pads were laid down using a standard metal evaporator to deposit 20 nm of titanium followed by 100 nm of gold. Lift-off then consisted of soaking the samples in acetone to remove the resist along with the unwanted areas of gold, and then rinsing with IPA to clear the contact edges of any remaining gold flakes. The full cleaning process performed prior to fabrication was then repeated to ensure an uncontaminated surface for the second layer exposure.

Second layer processing

With the gold contacts and alignment marks fabricated, the second stage was to define the rings themselves via EBL. High molecular weight PMMA resist (A2 950) was applied to the samples using a 5 ml pipette to guarantee total surface coverage. This was then spun at 5000 rpm for 45 seconds and oven baked at 180°C for 1 hour to remove the anisole casting solvent. The resulting resist had a thickness of 60 nm that was then reduced to roughly 30 nm after exposure due to the effects of crosslinking.

The second layer exposures were then carried out with four optimised pattern design ring exposures performed separately per substrate in order to avoid large amounts of stage movement after focus and astigmatism set up. In each case alignment was made using the gold contacts' respective inner alignment marks before the sample stage was moved and the focus and astigmatism adjusted before carrying out the next exposure. Exposures of variable diameter nanorings between 130 nm and 250 nm were performed with an acceleration voltage of 30 kV and 500 pA current. After exposing a ring and inner contacts for each of the sets of gold contacts on the substrates, the samples were developed in acetone for 2 minutes, rinsed in IPA and then blow-dried with nitrogen.

Samples were etched for 15 seconds in a Corial 200RL RIE system using $SiCl_4$ as the etch gas and SF_6 as the plasma cleaner with flow rates of 25 sccm and 2 sccm respectively, and an RF power of 60 W. This process was performed at a pressure of roughly 9.6 mTorr and temperature of 20°C. Etch depths measured via AFM were roughly 60 nm; however, unlike the previous etch testing this also included the thickness of any remaining crosslinked PMMA.

The samples were not originally exposed to oxygen plasma to remove this resist because of the potential damage caused to the (Ga,Mn)As surface and

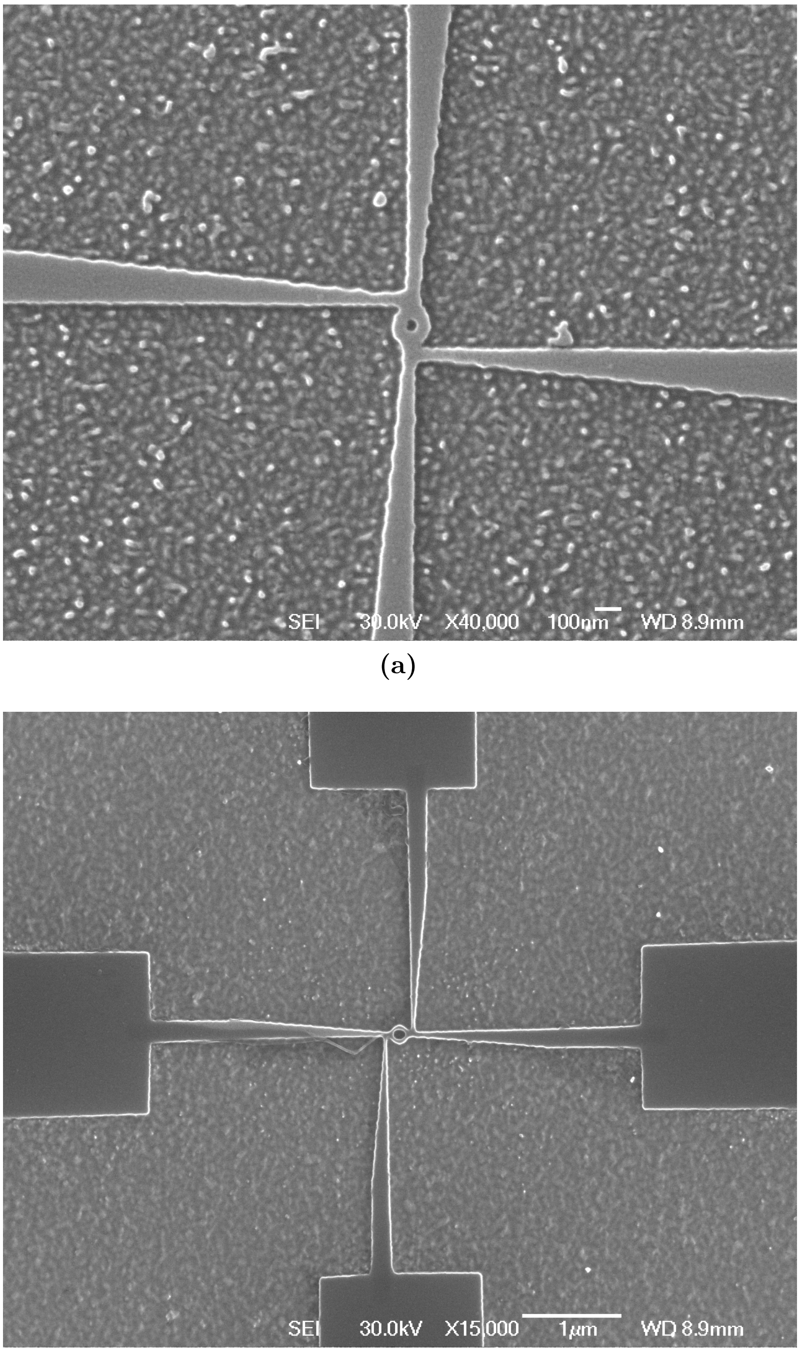

(a)

(b)

Figure 4.4.9: SEM images of typical (a) 130 nm and (b) 180 nm nanoring structures fabricated in Nottingham via the recipe detailed in this section.

structures leading to undesired effects on the electrical properties. It was thought that leaving the resist on could act to protect the rings after fabrication without affecting measurements. Unfortunately, initial dilution refrigerator measurements showed that in fact the remaining resist does have serious adverse effects on the resistance measurements. Structures were therefore later placed in the barrel asher to remove this unwanted surface contamination.

Once the structures had been defined the substrates were all scribed down to chip sizes of 5 mm x 4 mm, and then cleaned in acetone and IPA. These chips were then mounted into non-magnetic 12 pin headers using GE varnish, and bonds made to two of the four nanorings on each using an ultrasonic wire bonding machine. Bonding was limited to only two structures per chip due to the number of usable wires built into the dilution fridge probe.

4.4.3 Glasgow Nanorings

Nanoring fabrication in Glasgow was performed by Dr. Gary Ternent based off designs and processes which I suggested following a two-stage lithography process. A number of changes were made to the original Nottingham procedure due to the difficulties associated with the PMMA overexposure method and the equipment available. The most notable change to the final recipe detailed in section 4.4.2 was the use of hydrogen silsesquioxane (HSQ) to define the structures rather than PMMA. This is an inorganic negative-tone resist that consists of a cube-shaped monomer base molecule composed of silicon (Si), oxygen (O) and hydrogen (H) with molecular formula $H_8Si_8O_{12}$. It potentially offers a better etch resistance whilst retaining the high-resolution required for nanostructure fabrication, and is both well understood and frequently used in Glasgow as part of standard fabrication processing.

During the first stage of nanoring fabrication HSQ was used as part of a bilayer resist with PMMA to define the ring and (Ga,Mn)As contacts via EBL. This bilayer technique was developed in order to avoid the use of hydrofluoric acid which is commonly required to remove HSQ after processing due to its structural similarities to silicon dioxide. Whilst hydrofluoric acid is known not etch standard GaAs it has been observed to damage (Ga,Mn)As leading to rough structure edges that could significantly affect nanoring transport properties. The use of a PMMA layer below the HSQ meant that the resist could be removed via soaking in acetone.

After development the structures were defined in the (Ga,Mn)As following the same process as that in Nottingham using RIE with $SiCl_4$ and SF_6. Earlier test samples were etched using CH_4, but this was found to severely damage the structures. The second processing stage was then used to fabricate bond pads to the (Ga,Mn)As defined contacts via a standard photolithography and evaporation method using 20 nm Ti and 100 nm Au. Samples were bonded and mounted in Nottingham into non-magnetic 12 pin headers.

All Glasgow nanorings were fabricated on 6%, 10 nm (Ga,Mn)As having been annealed for eight hours at 180℃. The fabrication process was performed on 10 mm x 10 mm chips due to EBL system restrictions. These were then diced into 5 mm x 5 mm samples for packaging with each containing two sets of six structures of diameters 100 nm, 130 nm, 150 nm, 200 nm, 250 nm and 300 nm. SEM imaging shows the actual outer diameters to be approximately 20 nm greater than these nominal values with ring widths of between 30 nm and 50 nm. Unfortunately, such variable widths resulted in many of the 100 nm and 130 nm nanorings having no central hole due to overexposure thus leaving them unusable for Aharonov-Bohm measurements. Figure 4.4.10 shows SEM imaged examples of each diameter nanoring.

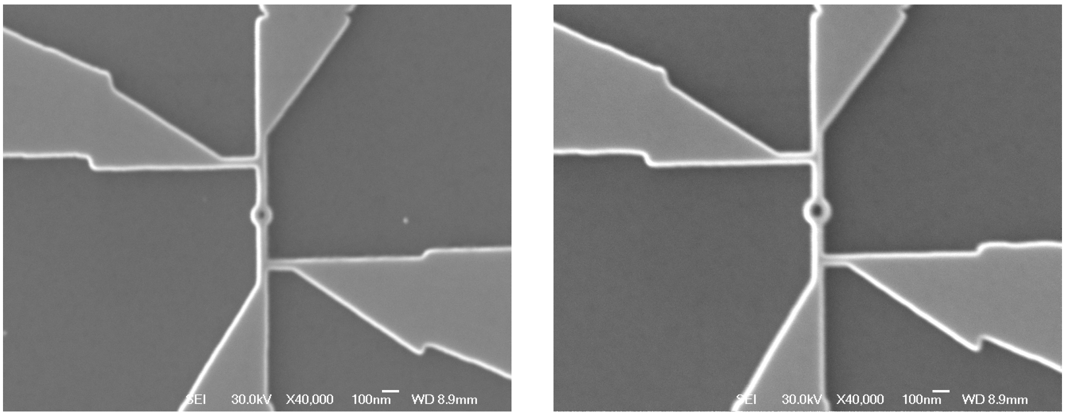

(a) 100 nm **(b)** 130 nm

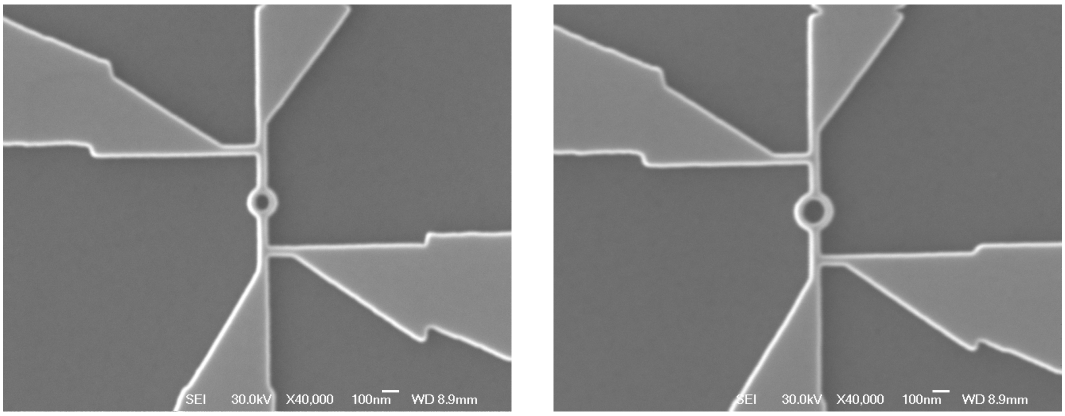

(c) 150 nm **(d)** 200 nm

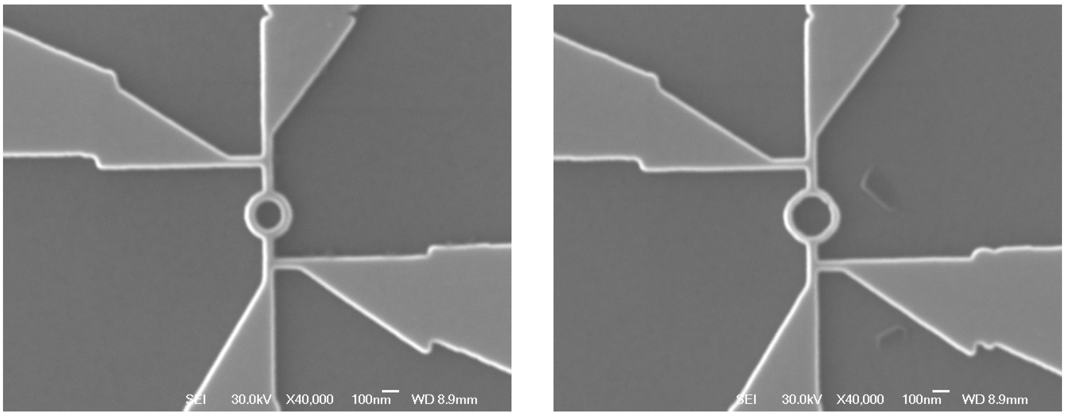

(e) 250 nm **(f)** 300 nm

Figure 4.4.10: SEM images of nanoring structures fabricated in Glasgow with defined outer diameters of (a) 100 nm, (b) 130 nm, (c) 150 nm, (d) 200 nm, (e) 250 nm and (f) 300 nm. The step-like edge visible on all contacts is due to a slight misalignment between the inner and outer (Ga,Mn)As contacts possibly due to write order.

4.5 Experimental Methods

A first batch of nanorings of diameters ranging from 130 nm up to 300 nm was fabricated in Nottingham following the recipe detailed in section 4.4.2. Test measurements on these structures using a Keithley source meter showed a variety of resistances at room temperature with some demonstrating resistances approaching that expected of 6%, 10 nm (Ga,Mn)As, but many clearly broken with much higher megaohm resistances. A set of six of the lower resistance structures were selected for low temperature measurements with nominal outer diameters of 130 nm and 180 nm. Resistances of these structures ranged from 12 kΩ to 35 kΩ at room temperature. These structures were measured within a dilution refrigerator at temperatures as low as 50 mK, sweeping the magnetic field between 0 T and 8 T. An overview of dilution refrigeration is given in appendix B.2.

Resistance measurements proved difficult with two methods employed to try to observe the expected oscillations. Structures were initially measured using an AVS-47 resistance bridge with a set excitation voltage of 10 μV equivalent to a 1 nA constant current. A number of other excitation voltages were also tested with values as low as 1 μV, but these resulted in significant amounts of noise. Most structures demonstrated oscillations in the measured resistance when sweeping the magnetic field. However, these oscillations had periods roughly a quarter of that expected, and had a sawtooth-like profile uncharacteristic of the Aharonov-Bohm effect. An example of this behaviour is shown in figure 4.5.1. Further testing showed that these measurements suffered from severe grounding issues, a problem that was later resolved.

One possible explanation for this behaviour is a coulomb blockade due to single-electron transport through the structures. Standard single-electron devices consist of a central localised region of electrons isolated from a source and drain by low-capacitance tunnel junctions. Within the nanorings this structure could be formed by nanoconstrictions in the contacts with the ring taking the role of the isolated central island. Due to the complex form of this structure and the large number of unknowns associated with such a setup exact calculations of the expected oscillation periods are not possible. Measurements of single-electron transport are typically performed on quantum dot structures with dimensions much smaller than the nanorings. However, past work on larger-scale structures (1 μm) have demonstrated similar sawtooth behaviour with periods of 0.2 T (Stopa *et al.* (1994)) approaching that seen in figure 4.5.1.

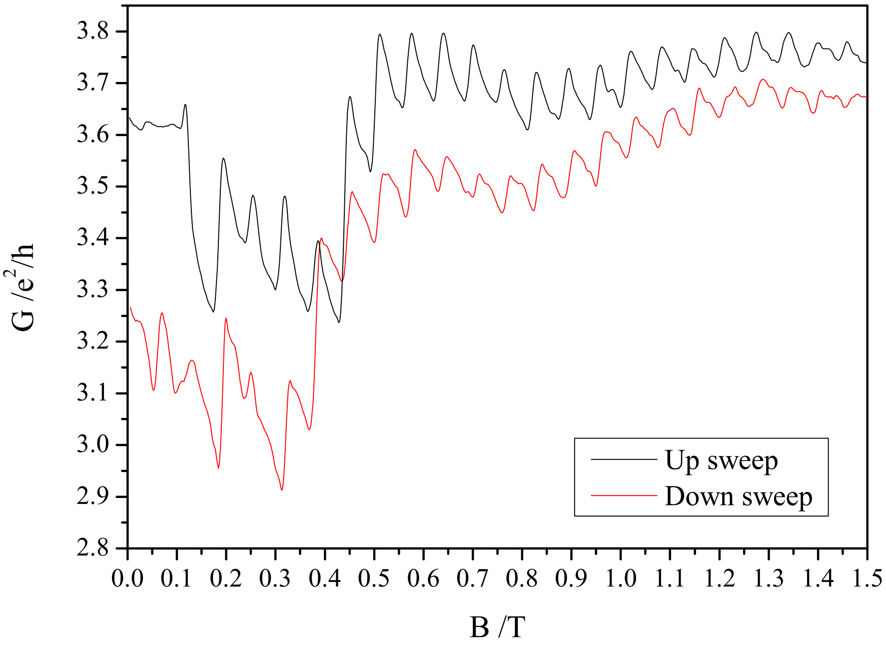

Figure 4.5.1: Magneto-transport data of a 130 nm diameter Nottingham nanoring measured at 100 mK using a four-terminal resistance bridge setup with an applied current of 1 nA. Both the up and down sweeps display a sawtooth oscillation with a period of roughly 0.07 T. The expected Aharonov-Bohm period for nanorings of this size is 0.31 T as calculated from equation (4.2.8).

These structures were also measured using a Signal Recovery 5210 lock-in amplifier applying a constant current of 100 pA with a ballast resistor of 10 MΩ. Various setups were used with later measurements also using a potential divider and a preamplifier. Structures showed a strong dependence on the applied frequency implying the presence of capacitive effects that could explain the observed sawtooth oscillations as charging and discharging. Samples also displayed a large amount of shorting between contacts potentially the source of this charging and discharging.

The most likely cause of the shorting between contacts in structures was residual overexposed PMMA or surface oxidation. Oxygen plasma ashing was therefore used on a number of structures to try to remove any remaining resist, and reduce the effects of shorting. Resistances between structures increased dramatically, but structures were partially damaged by the process.

Given these inherent problems with the structures these results are not presented within this chapter. The remaining dilution refrigerator time was dedicated to setup optimisation in preparation for future measurements. A better low-noise preamplifier was also purchased to improve signal-to-noise with greater noise having a significant effect on oscillation data analysis.

A second batch of structures was fabricated in Glasgow, and transport measurements performed within a standard ^{4}He cryostat on a range of nanorings again with diameters of between 130 nm and 300 nm. Sample resistances were measured using a standard four-terminal method using a Keithley Model 2400 source meter as a 100 nA constant current source and a Model 2000 meter to measure the voltage drop across the ring. Samples were cooled from room temperature down to 4.2 K at roughly 5 K per minute manually controlled via the needle valve, and data measured at 0.2 K to 0.3 K intervals. Section 4.6 presents some of the more encouraging low resistance datasets; however, there were still a significant number of broken or high resistance structures similar to that seen in the original Nottingham samples. Full sweep measurements were not performed on all structures, many were only tested at room and base temperatures.

4.6 Results

Figure 4.6.1 shows transport data from two Nottingham nanoring structures fabricated on separate chips taken from the same wafer. Both samples show a clear peak in resistance close to 150 K with rough plots of $\frac{\mathrm{d}R}{\mathrm{d}T}$ indicating T_c values around 125 K. A value typical of a fully-annealed 6%, 10 nm (Ga,Mn)As sample. The first of these, a 130 nm diameter ring, demonstrates a gradual linear rise from room temperature up to a peak, before dropping away with no appreciable rise at low temperatures. Such behaviour is very close to that of the standard profile discussed in section 1.7.1 with the resistance per square approaching the 1.3 kΩ of a typical Hall bar structure on 6%, 10 nm (Ga,Mn)As.

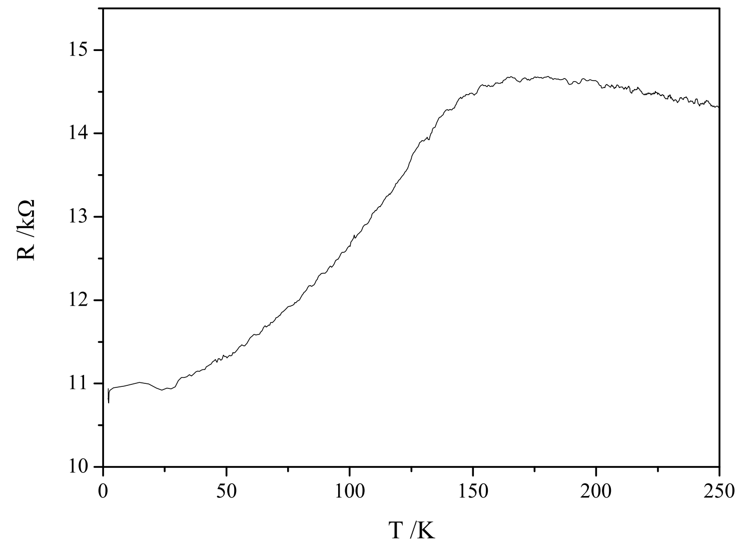

(a)

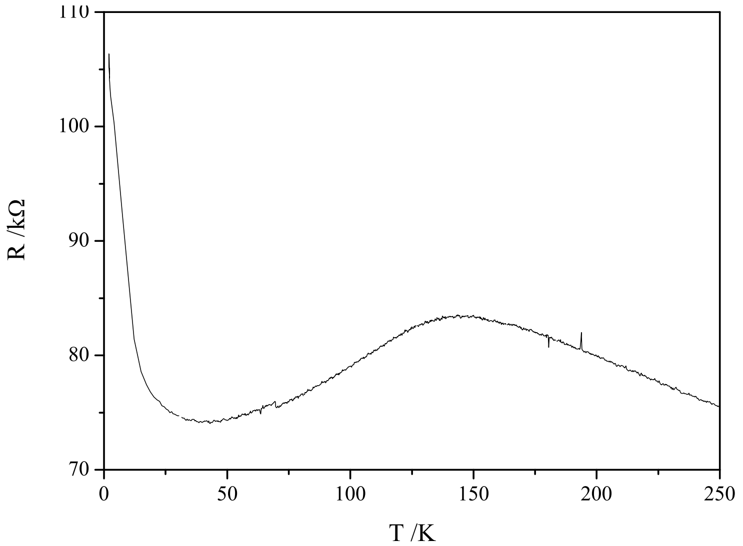

(b)

Figure 4.6.1: Transport data on (a) 130 nm and (b) 250 nm diameter nanorings fabricated in Nottingham.

Unfortunately, this sample is an exceptional case with most other measured structures demonstrating behaviour closer to that of the 250 nm nanoring shown in 4.6.1b. This shows an additional resistive component that leads to a general upward trend with a dramatic rise below 50 K and a much greater resistance per square. Measurements on other samples of the same nominal diameter frequently showed a variation with resistances per square generally appreciably larger than that demonstrated in larger structures. Many nanoring structures even demonstrated highly resistive behaviour with no discernible peak.

Figure 4.6.2 shows data from two Glasgow-fabricated samples of diameter (a) 200 nm and (b) 250 nm. Both structures demonstrate resistances appreciably lower than that seen in the 250 nm Nottingham sample, but still some way from that of the 130 nm sample. Both display behaviour with a strong resistive component at lower temperatures with T_c values predicted to be between 80 K and 90 K. This is substantially less than the Nottingham samples suggesting that these samples are not fully optimised. This is backed up by test measurements on large transmission line structures which showed the sheet resistance per square to be close to 2 kΩ, significantly higher than the wafers used for the Nottingham fabrications. This high resistance goes some way to explaining the measured nanoring resistances.

Whilst these larger structures offer an improvement in terms of resistance over many of the Nottingham samples no working 100 nm or 130 nm samples were measured. Typically these had megaohm resistances or, as discussed in section 4.4.3, no central hole. In general, smaller diameter Glasgow nanorings showed resistances higher than the Nottingham equivalents. Figure 4.6.3 shows two examples of high-resistance datasets, both from 150 nm diameter structures. Whilst these structures show very different resistances for nominally the same diameter nanorings both still demonstrate profiles very close to that of the 250 nm Nottingham sample with peaks suggesting T_c values close to 100 K.

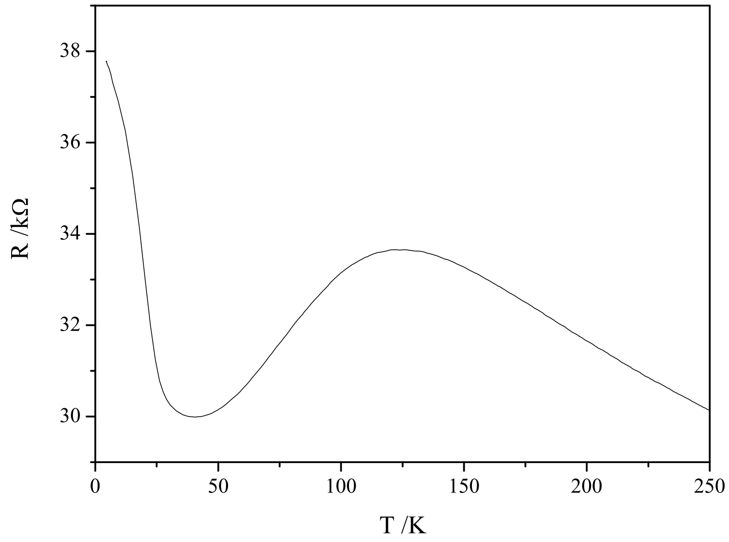

(a)

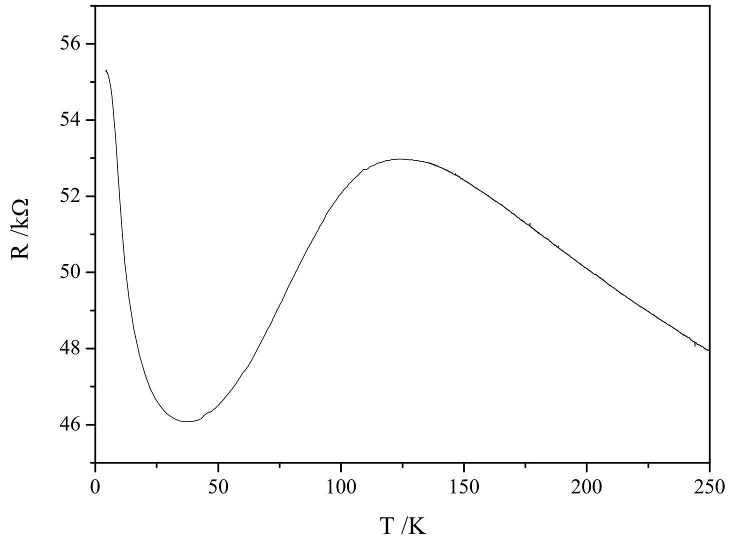

(b)

Figure 4.6.2: Transport data on (a) 200 nm and (b) 250 nm diameter nanorings fabricated in Glasgow. Both structures demonstrate larger resistances than the 130 nm nanoring fabricated in Nottingham, but due to the longer contact pattern design still display a resistance per square approaching that expected especially when compared to much larger transmission line structures on the same chip.

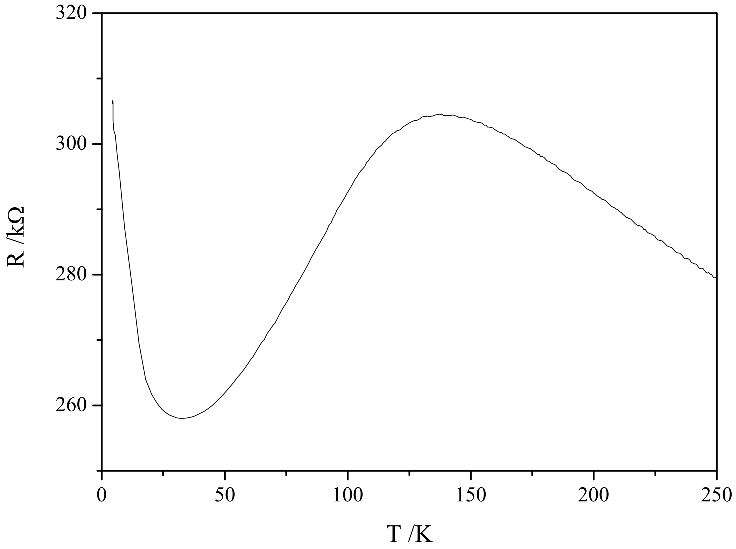

(a)

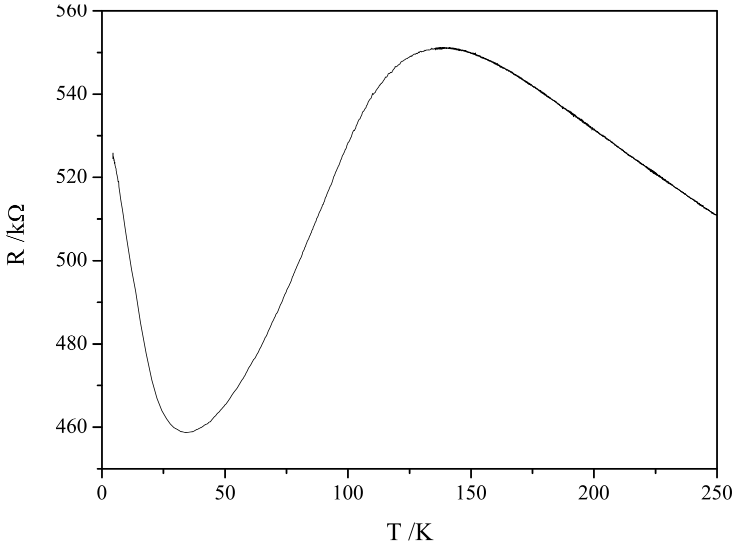

(b)

Figure 4.6.3: Transport data on two 150 nm diameter nanorings fabricated in Glasgow. Both samples demonstrate very high resistances per square, but still show very similar peak behaviour to that shown in 4.6.2.

4.7 Conclusions

This chapter has presented a comprehensive look at (Ga,Mn)As nanorings with the primary focuses being on nanofabrication, and early structure testing. Whilst the original aim of this work was to complete an in-depth study of phase coherent transport in high quality Nottingham grown samples, fabrication of nanoscale structures in (Ga,Mn)As proved difficult. A significant amount of time was invested in the development and optimisation of fabrication methods made necessary by problems related to the required structure size, and a lack of previous work on (Ga,Mn)As nanofabrication in Nottingham.

The first nanoring structures fabricated following the recipe developed in section 4.4 displayed encouraging resistance oscillations at millikelvin temperatures. However, these had periods and amplitudes roughly a quarter of that predicted by theory, and had a sawtooth profile uncharacteristic of Aharonov-Bohm oscillations. If produced by the expected interference of electrons such oscillations would suggest a much larger ring diameter than that defined via EBL or a smaller phase coherence length than originally postulated. These measurements also showed no signs of UCF which could again be indicative of a small phase coherence length with the fluctuations not easily distinguishable due to the restricted magnetic field sweep range. The magnetic field correlation length was predicted to be appreciably larger than the Aharonov-Bohm oscillation periods and comparable to the sweep range. Reducing the phase coherence length would further increase this calculated correlation field.

Both of these findings could indicate the need for smaller structures, however given the unusual profile of the observed oscillations it is more likely that these early measurements were affected by problems. This explanation is supported by later testing that showed that these structures suffered from serious shorting between contacts and structures with the oscillatory behaviour attributed to charging and discharging. These problems were likely caused by the presence of residual resist after fabrication, or oxidation linked to the RIE processing. Attempts to remove any unwanted overexposed PMMA via O_2 plasma ashing suppressed the effects of shorting between structures, but lead to further difficulties, and damage to the nanorings. Such unpredictable shorting and sample damage could also result in a larger apparent structure size potentially explaining the lack of UCF within these measurements.

Due to these difficulties the results from these early dilution refrigerator measurements were not fully presented within this chapter. However, these measurements did offer the opportunity for equipment setup optimisation, and allowed problems such as grounding and signal amplification to be identified and solved in preparation for the final studies. These measurements also illustrated the key problems in the fabrication procedure allowing a revised version to be developed at the University of Glasgow without the need for PMMA overexposure.

Despite these initial problems further work has shown that it is possible to fabricate nanorings approaching the expected phase coherence length in size with (Ga,Mn)As-like behaviour observed at ^{4}He cryostat temperatures. Measurements were performed on a variety of Nottingham and Glasgow samples with many demonstrating peaks in resistance that indicated Curie temperatures close to that expected for 6%, 10 nm (Ga,Mn)As. Most samples also showed an additional resistive component on top of the typical (Ga,Mn)As behaviour with a sharp rise at temperatures below 50 K. Similar behaviour has been observed in the past in early Nottingham-grown layers less than 10 nm thick. Given that this behaviour is seen in both Nottingham and Glasgow samples it is possible that this is unavoidable within nanoscale structures.

As well as this rise at low temperatures a large variation was observed between structures suggesting that consistent fabrication is still very difficult. However, this is not likely to be a problem given the fabrication processing time, and the number of structures that can be fabricated together on a single 5 mm x 5 mm chip.

With the fabrication procedure finalised the next step is to perform a full study of these nanoring structures at millikelvin temperatures within a dilution refrigerator applying the knowledge gained from the previous measurements. Successful calculation of the phase coherence length from these studies could potentially pave the way for further work on other quantum effects including UCFs or weak localisation. These fabrication methods could easily be adapted to produce other nanoscale structures in (Ga,Mn)As such as nanowires.

References

Aharonov, Y. and Bohm, D. ‘Significance of electromagnetic potentials in the quantum theory’. *Physical Review*, **115** (3) 485–491, (1959).

Al’tshuler, B. L. ‘Fluctuations in the extrinsic conductivity of disordered conductors’. *Journal of Experimental and Theoretical Physics*, **41** (12) 648–651, (1985).

Al’tshuler, B. L., Aronov, A. G., and Spivak, B. Z. ‘The Aaronov-Bohm effect in disordered conductors’. *Journal of Experimental and Theoretical Physics Letters*, **33** (2) 94–97, (1981).

Chambers, R. G. ‘Shift of an Electron Interference Pattern by Enclosed Magnetic Flux’. *Physical Review Letters*, **5** (1) 3–5, (1960).

Dirac, P. A. M. ‘Quantised singularities in the electromagnetic field’. *Proceedings of the Royal Society of London. Series A, Containing Papers of a Mathematical and Physical Character*, **133** (821) 60–72, (1931).

Ehrenberg, W. and Siday, R. E. ‘The Refractive Index in Electron Optics and the Principles of Dynamics ’. *Proceedings of the Physical Society. Section B*, **62** (1) 8–21, (1949).

Lee, P. A. and Stone, A. D. ‘Universal Conductance Fluctuations in Metals’. *Physical Review Letters*, **55** (15) 1622–1625, (1985).

Lee, P. A., Stone, A. D., and Fukuyama, H. ‘Universal conductance fluctuations in metals: Effects of finite temperature, interactions, and magnetic field’. *Physical Review B*, **35** (3) 1039–1070, (1987).

Lee, P. A. and Ramakrishnan, T. V. ‘Disordered electronic systems’. *Review of Modern Physics*, **57** (2) 287–337, (1985).

Matsukura, F., Sawicki, M., Dietl, T., Chiba, D., and Ohno, H. ‘Magnetotransport properties of metallic (Ga,Mn)As films with compressive and tensile strain’. *Physica E*, **21** (4) 1032–1036, (2004).

Neumaier, D., Wagner, K., Wurstbauer, U., Reinwald, M., Wegscheider, W., and Weiss, D. ‘Phase coherent transport in (Ga,Mn)As’. *New Journal of Physics*, **10** (5) 055016, (2008).

Osakabe, N., Matsuda, T., Kawasaki, T., Endo, J., Tonomura, A., Yano, S., and Yamada, H. 'Experimental confirmation of Aharonov-Bohm effect using a toroidal magnetic field confined by a superconductor'. *Physical Review A*, **34** (2) 815–822, (1986).

Stopa, M., Bird, J. P., Ishibashi, K., Aoyagi, Y., and Sugano, T. 'Magneto-coulomb oscillations in GaAs-AlGaAs quantum dot structures'. *Superlattices and Microstructures*, **15** (2) 99–103, (1994).

Umbach, C. P., Washburn, S., Laibowitz, R. B., and Webb, R. A. 'Magnetoresistance of small, quasi-one-dimensional, normal-metal rings and lines'. *Physical Review B*, **30** (7) 4048–4051, (1984).

van Oudenaarden, A., Devoret, M. H., Nazarov, Y. V., and Mooij, J. E. 'Magneto-electric Aharonov-Bohm effect in metal rings'. *Nature*, **391** 19, (1998).

Vila, L., Giraud, R., Thevenard, L., Lemaître, A., Pierre, F., Dufouleur, J., Mailly, D., Barbara, B., and Faini, G. 'Universal Conductance Fluctuations in Epitaxial GaMnAs Ferromagnets: Dephasing by Structural and Spin Disorder'. *Physical Review Letters*, **98** (2) 027204, (2007).

Wagner, K., Neumaier, D., Reinwald, M., Wegscheider, W., and Weiss, D. 'Dephasing in (Ga,Mn)As nanowires and rings'. *Physical Review Letters*, **97** (5) 56803, (2006).

Washburn, S. and Webb, R. A. 'Aharonov-Bohm effect in normal metal: Quantum coherence and transport'. *Advances in Physics*, **35** (4) 375–422, (1986).

Webb, R. A., Washburn, S., Umbach, C. P., and Laibowitz, R. B. 'Observation of h/e Aharonov-Bohm oscillations in normal-metal rings'. *Physical review letters*, **54** (25) 2696–2699, (1985).

Chapter 5

Conclusions and Future Work

5.1 Conclusions

This thesis has presented a number of studies on the transport and magnetic properties of the dilute magnetic semiconductor (Ga,Mn)As. The primary focuses have been critical phenomena, and low-temperature quantum interference effects.

Chapters 2 and 3 detailed two separate studies on critical phenomena. Fundamental theory of critical phenomena predicts power-law scaling relations between a material's properties upon approaching a critical point with the same behaviour across many different physical systems. Exponents are expected to fall into a number of distinct universality classes with theoretical work predicting Heisenberg-like behaviour in (Ga,Mn)As (Priour and Das Sarma (2010)).

The first of these two chapters detailed comprehensive magnetometry measurements around the critical region on two high manganese, high T_c samples. These measurements allowed accurate critical exponents to be calculated for the remanent magnetisation and the susceptibility with both samples demonstrating values closely matching that of the Heisenberg model. The effects of sample inhomogeneity were considered when performing these calculations with a strong agreement observed between the modelled T_c broadening, and the calculated exponent behaviour upon approaching the Curie temperature. This

Heisenberg-like behaviour was also confirmed over a much broader spectrum of samples via past-dataset analysis.

The conclusions from this work, whilst in agreement with theoretical calculations, contrasted with that of a previous study on (Ga,Mn)As performed by Khazen *et al.* (2010). Within this work an intrinsic limit to the Curie temperature was postulated based on analysis of the magnetisation critical behavior and models of disordered/amorphous ferromagnets. A log-log method was used to calculate the critical exponent to be 0.407, a value appreciably higher than that predicted by the Heisenberg model, and the work presented within this thesis. The author concluded that this enhancement of the exponent was consistent with an intrinsically limited T_c caused by a reduction in the magnetic interactions range. References were made to observations of similar behaviour in amorphous materials. However, the analysis techniques applied within this work are questionable with the log-log fitting method shown to be inaccurate without a precise value for T_c, and the fitting ranges used being much larger than the expected critical region. Long range fitting to Nottingham datasets supports these views with many samples demonstrating a clear move to higher exponents at temperatures below the critical region with values closely matching that calculated by Khazen *et al.* (2010).

The second critical phenomena chapter concentrated on the transport properties close to T_c with the SQUID system adapted to permit simultaneous resistance and magnetometry measurements. Measurements of the resistance allowed the differential to be calculated with the critical behaviour expected to follow that of the specific heat. Unfortunately, critical exponent calculations similar to that of the magnetometry work were not possible due to the need for a double numerical differential, and additional terms expected in the specific heat power-law behaviour. Open fitting to datasets resulted in inconsistent results between samples due to the required number of parameters and the addition of T_c broadening.

Whilst this critical behaviour characterisation proved dificult, these measurements did confirm the behaviour observed by Novák *et al.* (2008). Both samples demonstrated a strong agreement between the magnetisation-measured T_c value, and the peak in $\frac{\mathrm{d}R}{\mathrm{d}T}$. Such behaviour invalidates the frequently used resistance peak measurement of T_c. Within a recent paper, Chen *et al.* (2011) used this method to predict sample Curie temperatures of between 190 K and 200 K; values appreciably higher than samples grown in Nottingham. However, the work within this thesis has shown that this method consistently overestimates the Curie temperature of fully annealed samples with the behaviour demonstrated by these structures indicating T_c values closer to 170 K. A value much more in-line with that observed in previous studies.

Chapter 4 focused on the preparation work necessary for a in-depth study of Aharonov-Bohm oscillations in (Ga,Mn)As with the aim of calculating the phase coherence length, and confirming the behaviour observed by Neumaier *et al.* (2008). The Aharonov-Bohm effect is derived from the additional phase an electron acquires when passing through a region of zero magnetic field, but non-zero magnetic vector potential. The effects of this change in phase can be demonstrated within the standard double-slit experiment by adding a long solenoid in the region between the slits. The result is a shift in the expected interference pattern due to different changes in phase around each path. The effect also manifests itself within material ring structures if the electron phase coherence length is comparable to or greater than the arc length. Oscillations can be observed in the conductance under swept magnetic field with a period related to the enclosed magnetic flux.

The phase coherence length of (Ga,Mn)As is expected to be of the order 100 nm at millikelvin temperatures thus prompting the need for nanoring structures of comparable size. An extensive discussion of the methodology used to develop the techniques required for these fabrications was presented with details regarding the difficulties encountered and the steps taken to overcome them. Initial dilution refrigerator measurements on these devices proved difficult due to both shorting and grounding problems, but did offer an opportunity for setup optimisation applicable to future measurements. An alternative fabrication method was developed at the University of Glasgow heavily based on that used for the first Nottingham samples. Preliminary test measurements on later structures at ^{4}He temperatures demonstrated encouraging behaviour over a range of ring diameters, however, a complete low-temperature study of phase coherence phenomena has not yet been performed due to time constraints.

5.2 Future Work

Despite the compelling results seen in chapters 2 and 3 on critical phenomena the field still remains relatively unexplored in (Ga,Mn)As with a vast scope for future work. This is particularly true of the transport behaviour with the work presented in chapter 3 demonstrating a strong agreement between the peak in $\frac{\mathrm{d}R}{\mathrm{d}T}$ and T_c, but characterisation of the observed behaviour proving difficult. Samples appeared to show non-power law behaviour resulting in inconsistent exponent values.

One possible source of this problem could be the unconventional SQUID setup which included a very simple clamp-based design for the probe-header used to avoid unnecessary magnetic components. However, whilst a redesign of the probe-header could potentially improve contact problems it is also possible that the apparent non-power law behaviour is intrinsic to the transport data itself. No measured confirmation has yet been made in (Ga,Mn)As of the expected equivalence of $\frac{\mathrm{d}R}{\mathrm{d}T}$ to the specific heat critical behaviour.

Similar to the magnetometry, past work on specific heat critical behaviour in (Ga,Mn)As has been very limited with only Yuldashev *et al.* (2011) performing calculations of the critical exponent. Unfortunately, whilst sharp peaks were observed at T_c the results from these studies were inconclusive with samples demonstrating significantly different calculated values suggesting no clear single critical model. This inconsistent behaviour was most probably derived from the quality of the (Ga,Mn)As used which was only as-grown with Curie temperatures as low as 50 K. Magnetisation critical behaviour data analysis on as-grown samples in Nottingham has in the past shown equally inconsistent, and difficult to interpret results.

Given this current situation one potential avenue for future research is therefore to perform specific heat measurements on high T_c Nottingham samples. Simultaneous transport measurements would then allow a comparison to the $\frac{\mathrm{d}R}{\mathrm{d}T}$ behaviour with the aim of confirming the expected equivalence in (Ga,Mn)As. A direct measurement of the specific heat would also permit the calculation of the critical exponent without the influence of additional resistive terms typically observed in transport datasets.

Whilst the work on critical behaviour proved successful largely achieving the original aims, the work on nanorings presented in chapter 4 remains work-in-progress. With the fabrication processes finalised, and prelimenary test measurements performed clearly the next stage in this work is to proceed with a complete low-temperature study on the highest conductance structures. Observations of Aharonov-Bohm oscillations within these sample would then allow the phase coherence length to be calculated for Nottingham-grown (Ga,Mn)As.

These studies could potentially pave the way for further work on phase coherent transport in (Ga,Mn)As with measurements of other quantum mechanical effects such as weak localisation or UCFs. However, given the problems found in device fabrication, an alternative and potentially more profitable direction to pursue for future work would be to branch out to the antimonides. Performing Aharonov-Bohm studies on these materials would in principle be much easier than that on (Ga,Mn)As due to their metallic behaviour. The longer mean free paths of the antimonides would permit the use of larger structures alleviating many of the device fabrication difficulties as well as reducing the effects of UCFs during measurements. The higher mobilities would also leave them less susceptible to structure damage.

References

Chen, L., Yang, X., Yang, F., Zhao, J., Misuraca, J., Xiong, P., and von Molnár, S. 'Enhancing the Curie Temperature of Ferromagnetic Semiconductor (Ga,Mn)As to 200 K via Nanostructure Engineering'. *Nano Letters*, **11** (7) 2584–2589, (2011).

Khazen, K., von Bardeleben, H. J., Cantin, J. L., Mauger, A., Chen, L., and Zhao, J. H. 'Intrinsically limited critical temperatures of highly doped $Ga_{1-x}Mn_xAs$ thin films'. *Physical Review B*, **81** (23) 235201, (2010).

Neumaier, D., Wagner, K., Wurstbauer, U., Reinwald, M., Wegscheider, W., and Weiss, D. 'Phase coherent transport in (Ga,Mn)As'. *New Journal of Physics*, **10** (5) 055016, (2008).

Novák, V., Olejník, K., Wunderlich, J., Cukr, M., Výborný, K., Rushforth, A. W., Edmonds, K. W., Campion, R. P., Gallagher, B. L., Sinova, J., and Jungwirth, T. 'Curie Point Singularity in the Temperature Derivative of Resistivity in (Ga,Mn)As'. *Physical Review Letters*, **101** (7) 077201, (2008).

Priour, D. J. and Das Sarma, S. 'Critical behavior of diluted magnetic semiconductors: Apparent violation and eventual restoration of the Harris criterion for all regimes of disorder'. *Physical Review B*, **81** (22) 224403, (2010).

Yuldashev, S. U., Igamberdiev, K. T., Lee, S., Kwon, Y., Kang, T. W., and Shashkov, A. G. 'Study of $Ga_{1-x}Mn_xAs$ Critical Behavior by Using Thermal Diffusivity'. *Journal of the Korean Physical Society*, **59** (2) 431–434, (2011).

Appendix A

List of Acronyms

AC alternating current

AES auger electron spectroscopy

AFM atomic force microscope

AMR anisotropic magnetoresistance

DC direct current

DIW deionised water

DMS dilute magnetic semiconductor

EBL electron beam lithography

GMR giant magnetoresistance

HSQ hydrogen silsesquioxane

IPA isopropyl alcohol

MBE molecular beam epitaxy

MIBK methyl isobutyl ketone

MPMS Magnetic Property Measurement System

PCD probe current detector

PMMA poly(methyl methacrylate)

PTFE polytetrafluoroethylene

RF radio frequency

RHEED reflection high-energy electron diffraction

RIE reactive-ion etching

RSO reciprocating sample option

SEM scanning electron microscope

SQUID superconducting quantum interference device

UCF universal conductance fluctuations

UHV ultra-high-vacuum

UV ultraviolet

XPS x-ray photoelectron spectroscopy

Appendix B

Equipment

B.1 The Quantum Design Magnetic Property Measurement System

In 1962 Brian David Josephson (Josephson (1962)) postulated the existence of Cooper pair quantum tunnelling between superconductors separated by a resistive barrier. He suggested that Cooper pairs could tunnel through the barrier with no voltage drop for distances less than the superconductor phase coherence length and derived a relation between the resulting current I_s and the phase difference $\Delta\varphi(t)$ between the two superconducting wavefunctions. The result of this coupling of superconductors in the absence of an applied voltage is known as the DC Josephson effect.

$$I_\mathrm{s} = I_\mathrm{c} \sin\big(\Delta\varphi(t)\big) \tag{B.1}$$

Within a superconductor there is critical limit to the resistance-less current that can pass through dependant on the size of the conductor. Similarly a Josephson junction also has a critical current I_c above which superconductivity through the barrier is destroyed. This critical current is less than that of the superconductors either side. Josephson junctions are therefore frequently referred to as a weak-links. If a current greater than I_c is driven through the junction from an external source then a direct voltage appears across it related to the difference in the chemical potentials of the two superconductors. A direct voltage leads to an AC current with the time derivative of $\Delta\varphi(t)$ proportional to the voltage across the junction. This behaviour is known as the AC Josephson effect.

$$\frac{\partial\Delta\varphi(t)}{\partial t} = \frac{2eV}{\hbar} \tag{B.2}$$

One of the first practical applications of the Josephson effect was in the SQUID magnetometer developed in the 1960s at the Ford Research Labs (Jaklevic *et al.* (1964, 1965)). These act as accurate flux-to-voltage converters offering extremely sensitive magnetic field detection with the best systems capable of field resolutions as small as 10^{-17} T. SQUID magnetometry is therefore one of the most effective methods for measuring the magnetic properties of materials such as (Ga,Mn)As.

A SQUID consists of a loop of superconductor within which there are one or more Josephson junction weak-links. Such closed-circuit loops of superconductor have two very useful properties. The first is that the total flux threading the loop remains constant due to induced screening currents derived from Lenz's law. These tend to compensate for any flux change resulting from an applied external field. The second is that they can only contain discrete units of magnetic flux $\phi_0 = \frac{h}{2e}$. This is again ensured by screening currents.

When a SQUID is subjected to an external magnetic field a screening current I_s is induced with the size and direction determined by the applied field. A bias current I_b is applied to the SQUID so that the total current through the loop therefore becomes the sum of both the bias and screening currents. When this total current through the Josephson junction becomes greater than I_c the superconductivity breaks down. Once the magnetic flux created by the screening current becomes greater than half a fluxon $\frac{\phi_0}{2}$ the Josephson junction momentarily becomes normal and the internal magnetic flux increases by a single fluxon. The superconductivity is then restored with the screening current flowing in the opposite direction around the loop. This screening current then begins to drop until the external flux is equal to one fluxon at which point the induced current becomes zero. As the external field continues to increase the screening current begins to rise again in opposite direction. The whole process is then repeated with the total flux within the loop steadily increasing by a single fluxon.

When using a SQUID as a magnetometer a bias current is applied which is slightly greater than the Josephson junction critical current. Under such conditions there is a periodic relation between the voltage across the SQUID and the applied magnetic flux. Due to this inherent periodicity a SQUID cannot distinguish between zero applied field and any other field that generates an integer number of fluxons within the loop. In order to measure an absolute value a SQUID must therefore first be calibrated to a known magnetic field.

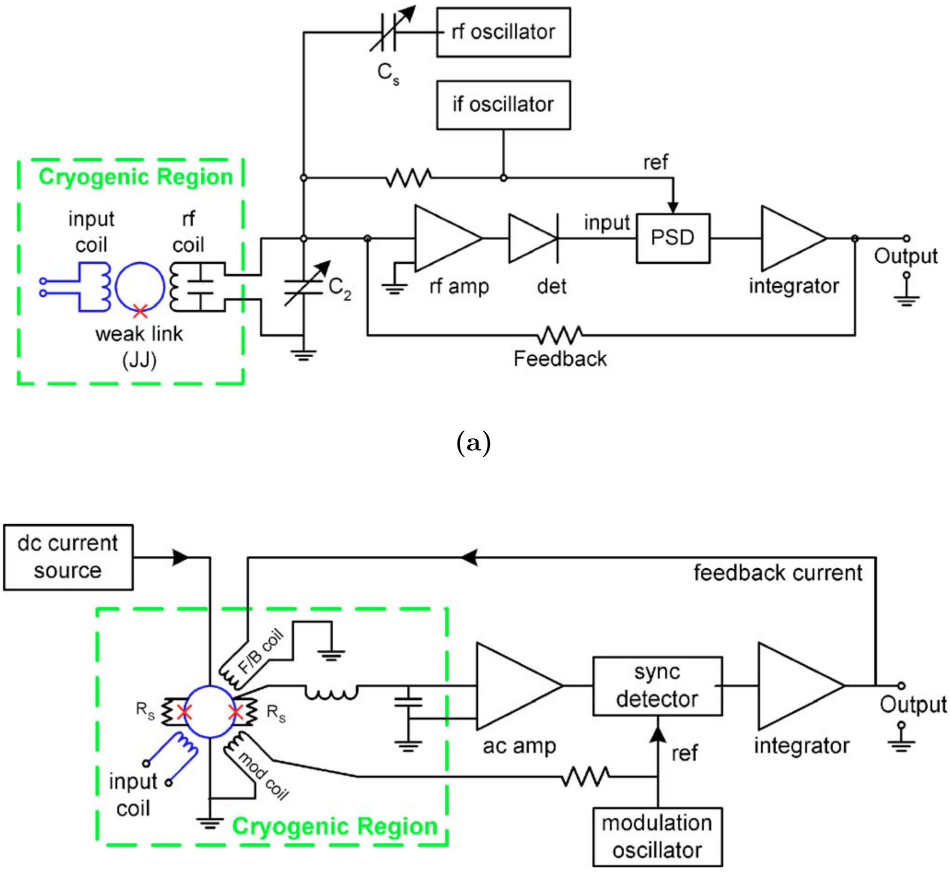

(a)

(b)

Figure B.1: Block diagrams of typical (a) RF and (b) DC SQUID circuits taken from Fagaly (2006).

The Ford Research Labs group lead by Robert Jaklevic invented two variations of the SQUID magnetometer. The first type was the DC SQUID developed in 1964. This contained a pair of Josephson junctions in parallel within a superconducting loop and made use of the DC Josephson effect operating with a steady current bias. The second type, developed only a year later, contained a single junction and operated with an alternating current bias employing the AC Josephson effect. Although developed after the DC magnetometer these RF SQUID are not as sensitive, but are typically cheaper produce and still capable of measuring flux changes much less than a single fluxon. Figure B.1 shows typical SQUID circuitry without the detection coils for both (a) RF and (b) DC magnetometer variants. A much more in-depth review of both types of SQUID, theory of operation, circuitry, applications and limitations is given by R. L. Fagaly (Fagaly (2006)).

The SQUID system used to perform measurements on (Ga,Mn)As samples in Nottingham is a MPMS XL. This is a commercially built RF magnetometer from Quantum Design that uses both SQUID technology and a number of patented enhancements. Sample signals are measured via a superconducting four-coil gradiometer which together with a SQUID antenna forms part a superconducting circuit that transfers the magnetic flux from the sample to an RF SQUID located in a niobium shielded helium bath. The SQUID output voltage is then amplified and read out by the MPMS electronics. The system is computer-automated allowing measurement sequences to be programmed in advance before being executed without the need for user intervention.

The MPMS is capable of both DC magnetisation and AC susceptibility measurements over a temperature range of 1.9 K to 400 K. DC magnetometry is performed via the use of an reciprocating sample option (RSO) which moves the sample up and down through the pick-up coils to produce an alternating flux. This leads to an oscillating output voltage from the SQUID. By locking the frequency of the readout to the frequency of the RSO the system is capable of an absolute DC magnetisation sensitivity of 10^{-8} emu at 2500 Oe. Hysteresis loop measurements can also be performed with the RSO using the systems high-homogeneity superconducting magnet which is capable of fields up to ±1 T with a uniformity of 0.01% over 4 cm.

AC susceptibility measurements are performed by superimposing a small AC magnetic field on the DC field causing a time-dependent moment in the sample. This induces a signal in the pick-up coils allowing measurement without sample

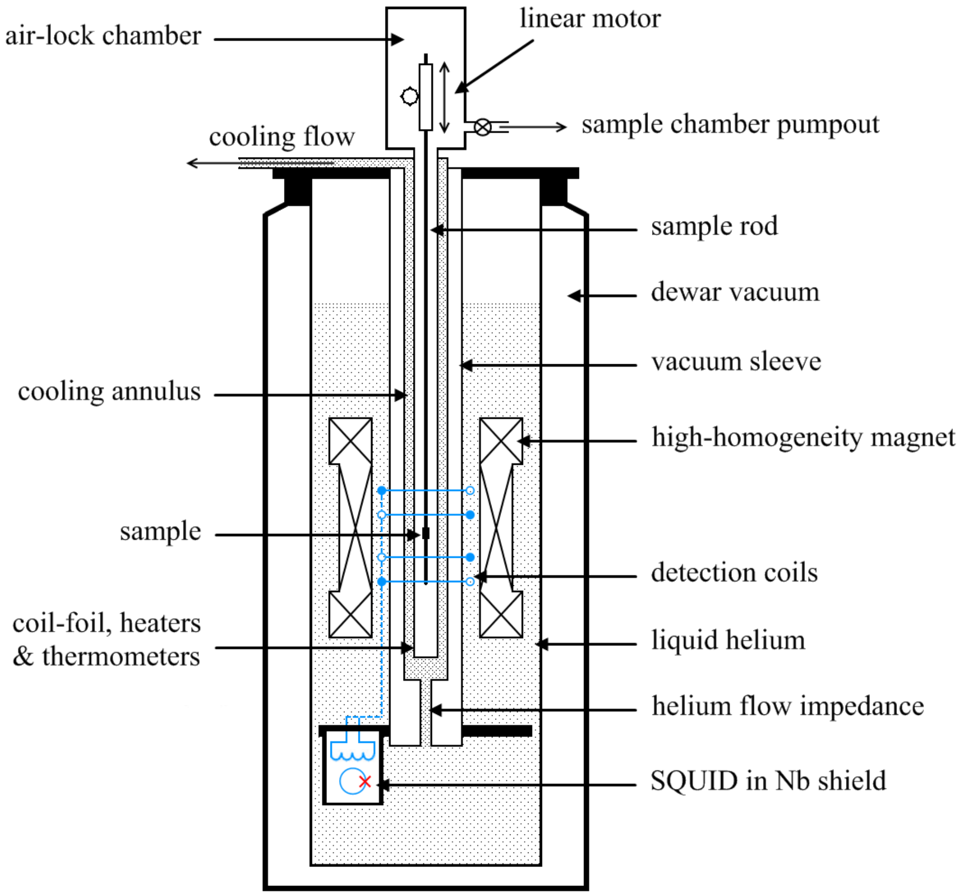

Figure B.2: A cross-sectional diagram of the MPMS SQUID system adapted from Clarke and Braginski (2007).

motion. The detection circuitry is configured to only detect over a narrow frequency band. Measurements within the MPMS system can be made over a frequency range of 0.1 Hz to 1 kHz with a sensitivity of 2×10^{-8} emu at 0 T. A diagram of the MPMS system is shown in figure B.2. A more complete review of the capabilities of the MPMS system is given by M. Sawicki (Sawicki *et al.* (2011)).

B.2 Dilution Refrigeration

The standard method used to cool samples for measurement is via the evaporation of helium-4 or -3 liquid within a cryostat. However, the lowest temperatures that can be reached using this technique are limited by the vapour pressure which falls exponentially with temperature. A typical ^{4}He cryostat can operate at temperatures as low as 1.3 K, a value less than the 4.2 K boiling point of helium-4. This is achieved by pumping away the helium vapour to increase the evaporation rate. The use of helium-3 permits even lower temperatures due to the lower mass of the ^{3}He atom resulting in a higher vaporisation pressure, but this is still limited to 0.3 K. An alternative method is therefore required in order to perform measurements at temperatures in the milliKelvin range.

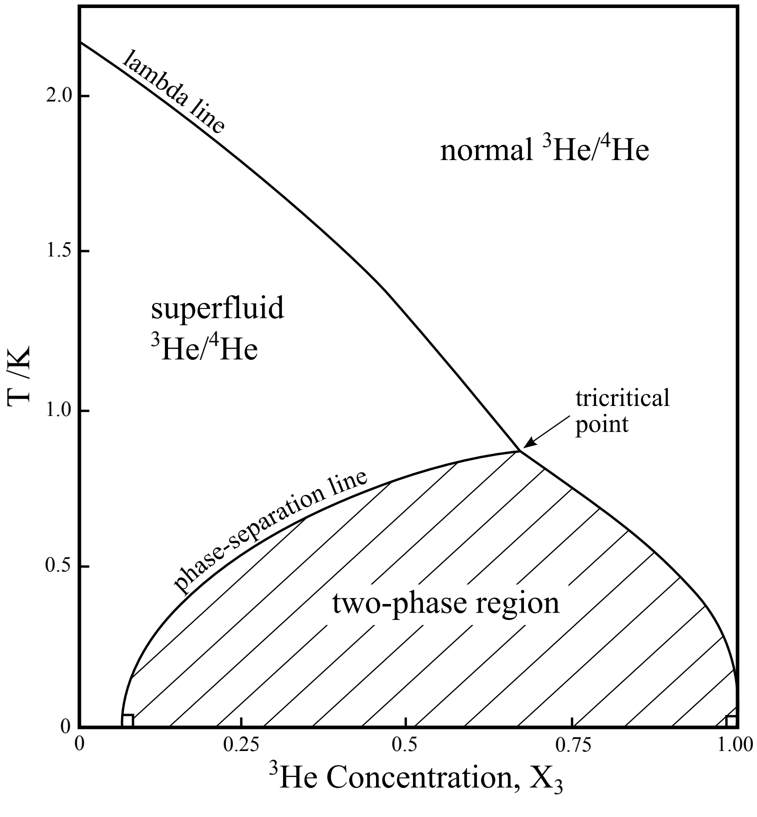

Figure B.1: A phase diagram of the ^{4}He and ^{3}He mixture within a dilution refrigerator.

This limitation of helium evaporation is overcome by using a mixture of both liquid ^{4}He and liquid ^{3}He, a technique originally proposed by Heinz London in 1951. The first dilution refrigerators, built in 1964, were capable temperatures of 0.22 K, but performance of these systems has greatly improved with typical systems used within research capable of temperatures around 20 mK. The operating principles of a dilution refrigerator are based on the unusual properties exhibited by the mixture at temperatures below 0.8 K. Figure B.1 shows the phase diagram of a mixture of ^{4}He and ^{3}He below 2 K.

At temperatures below the triple point the mixture can only exist in one of two states: that in the superfluid region on the left or that in normal fluid region on the right. The mixture therefore separates into two liquid phases divided by a phase boundary, one rich in helium-3 called the concentrated phase and the other rich in helium-4 called the dilute phase. Equilibrium concentrations within each of these layers are dictated by the phase-separation line. As can be seen from the diagram at very low temperatures the concentrated phase is composed almost entirely of ^{3}He whilst the dilute phase must contain at least 6.6% ^{3}He. It is this percentage of helium-3 within the dilute phase that makes the dilution refrigerator possible.

Both phases form a layer with the concentrated phase floating on top due to the lower density of the ^{3}He. A good analogy to this behaviour is that of oil and water when mixed together. If the mixture is held at a high temperature both components mix together, but if the temperature is lowered the oil separates from the water and floats on the surface forming two distinct phases. This is the behaviour commonly observed at room temperature with each of the layers containing a small amount of the other material, similar to that seen in the helium mixture.

Since there is a boundary between the two phases, additional energy is required for a particle to move from one phase to another. This endothermic process can be made use of for cooling by removing ^{3}He from the dilute phase, this forces ^{3}He from the concentrated phase across the phase boundary in order to restore equilibrium. The removal of ^{3}He within a dilution refrigerator is performed via pumping, made possible by the much smaller vapour pressure of the ^{4}He below 0.8 K. The lost ^{3}He within the concentrated phase is then replenished by a constantly circulating flow of helium-3.

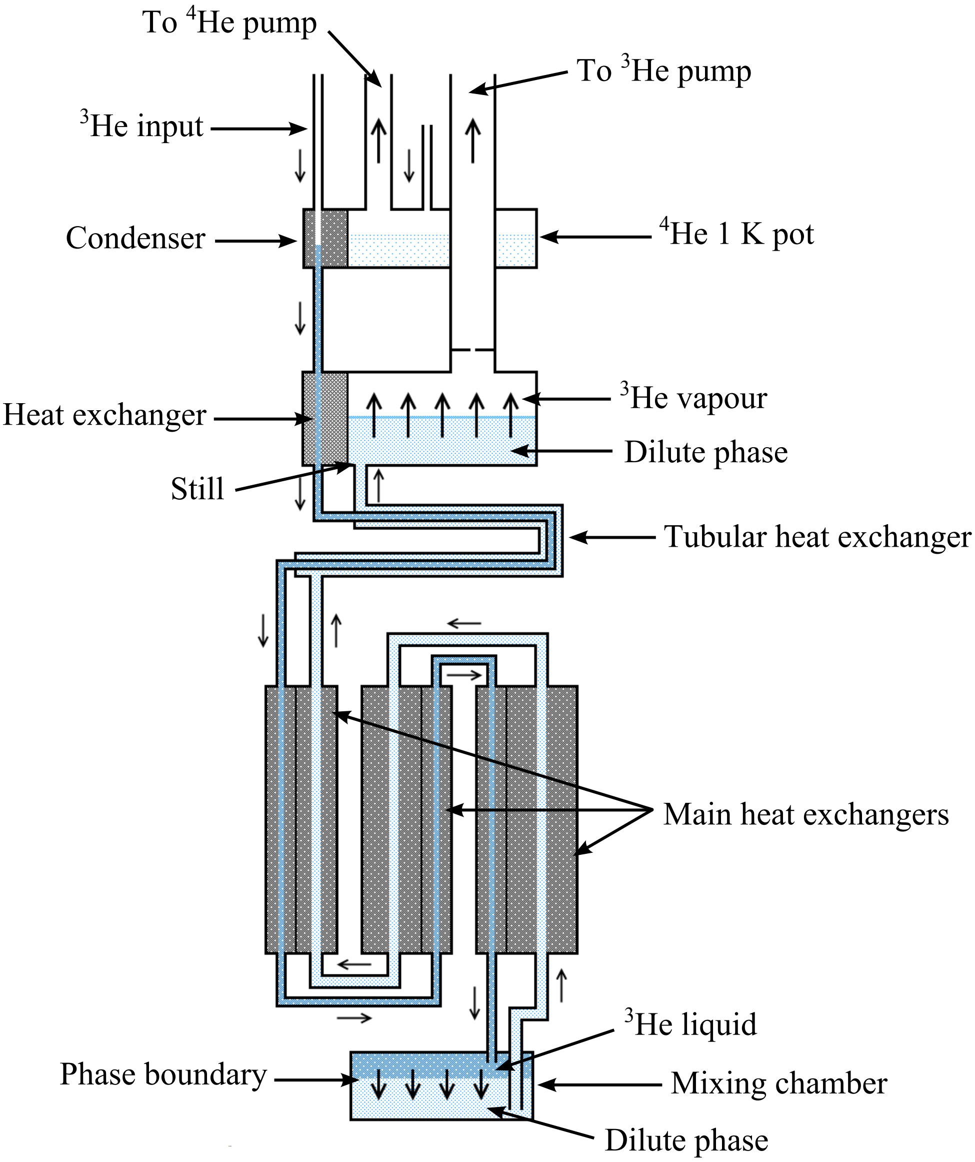

Figure B.2: A schematic diagram of the low-temperature components of a conventional dilution refrigerator adapted from Lounasamaa (1979). The heat exchangers and condenser are filled with a sintered copper or silver sponge in order to increase the thermal contact area, and have clear holes in the middle for unimpeded ^{3}He flow. The temperatures within the condenser and the still are roughly 1.1 K and 0.7 K respectively.

Figure B.2 shows a schematic diagram of a typical dilution refrigerator. Incoming ^{3}He gas is pre-cooled and liquefied in the condenser using a pumped

^{4}He bath at 1.1 K. The liquid ^{3}He is then further cooled by passing through a series of heat exchangers linked to the returning helium flow before entering the mixing chamber. It is here that the ^{3}He is mixed with ^{4}He and crosses the phase boundary taking heat from the walls of the chamber. The ^{3}He atoms then proceed in reverse order through the heat exchangers in a dilute superfluid phase cooling the downward flowing ^{3}He until the still is reached. Here helium vapour consisting almost entirely of pure ^{3}He is removed via pumping with heat supplied to the still to maintain a steady flow of ^{3}He. This vapour is then further purified before being reintroduced to the system at the ^{3}He input thus completing the cycle.

Appendix C

Low-Temperature Magnetoresistance Studies

This section gives a brief overview of a low-temperature study of the magnetoresistance properties of (Ga,Mn)As following on from earlier work by Dr. Kaiyou Wang. Resistance measurements were performed between 20 mK and 300 mK within a dilution refrigerator on 25 nm thick, 6% (Ga,Mn)As sample Mn107_a. This sample had been annealed for 50 hours at 190℃ prior to this study with past magnetometry measurements on similar samples from the same wafer displaying Curie temperatures around 140 K.

Preliminary test measurements of the longitudinal resistance of Mn107_a performed within a standard helium-4 cryostat exhibited behaviour very close to past datasets on other Mn107 samples. Figure C.1a shows this data along with the associated $\frac{\mathrm{d}R}{\mathrm{d}T}$ plot. The $\frac{\mathrm{d}R}{\mathrm{d}T}$ data shows a broad peak by comparison to that seen in the chapter 2 datasets most likely due to the large data step-size and temperature sweep rate, both of which were much higher than that used when focusing on the critical phenomena. This peak in the differential is also seen to be slightly lower than the 140 K Curie temperature measured via magnetometry shown in figure C.1. Such a shift can again be explained by the high rate of cooling especially when also considering the additional effects of T_c broadening covered in section 2.5.5.

Measurements of both R_xx and R_xy were performed on Mn107_a using a standard Hall bar setup. This structure had a channel width of 200 μm and length

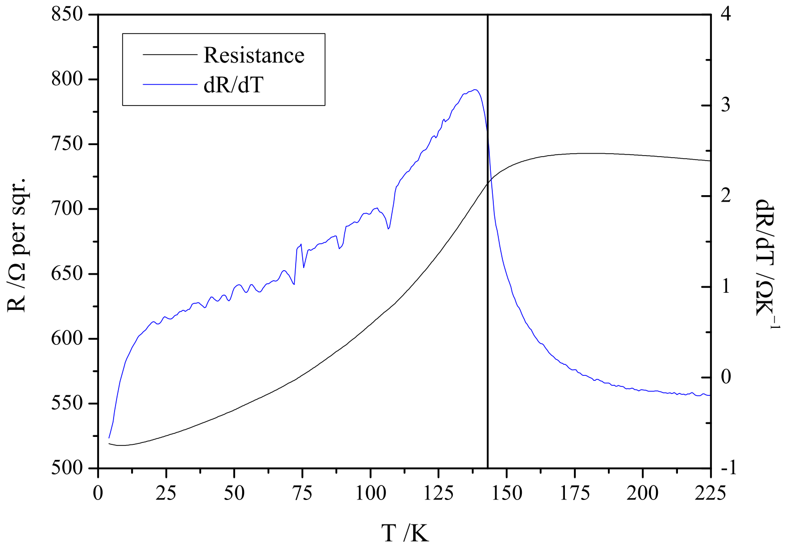

(a)

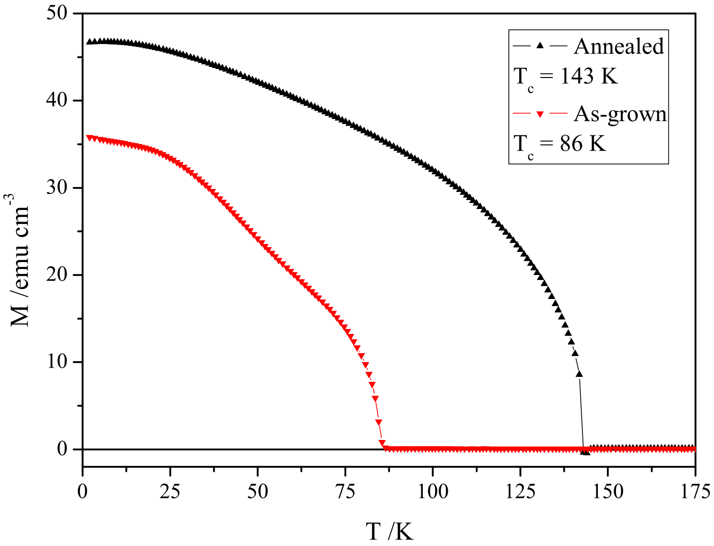

(b)

Figure C.1: Resistance (a) and remanent magnetisation (b) measured as a function of temperature for annealed Mn107 samples.

of 400 μm with the current applied along the $[1\bar{1}0]$ direction. The magnetic field was swept between ±5 T parallel to the current, and an AVS-47 AC resistance bridge used to measure the resistance. The sample temperature was monitored through the use of both an RuO_2 thermometer mounted on the probe and the in-built Kelvinox system used to heat above base temperature.

The AVS-47 was used rather than a lock-in amplifier to avoid difficulties with signal phase introduced by capacitance within the circuit. The resistance bridge consists of two feedback loops with the first maintaining a constant amplitude AC excitation voltage across a room temperature reference resistor. This is connected in series with the sample and has a resistance half that of the selected range. The second loop converts this low AC voltage into a measurable DC voltage. Both excitation and feedback currents are symmetrical square waves generated by a chopper so that the amplitude is accurately proportional to a DC voltage.

Due to the small changes in sample resistance ($< 1\%$) when sweeping magnetic field the AVS-47 was used in $10 \times \Delta\mathrm{R}$ mode. This employs a differential amplifier to attain an additional decimal of accuracy over the standard mode by amplifying the difference between two voltages and then adding this signal to a reference taken at either zero or maximum field.

Initial test measurements were performed at base temperature with applied excitation voltages of between $3\,\mu\mathrm{V}$ and $300\,\mu\mathrm{V}$. Lower voltage R_{xx} measurements demonstrated overwhelming levels of noise with only voltages above $100\,\mu\mathrm{V}$ resulting in well defined datasets. Measurements taken at higher temperatures showed optimum results at $300\,\mu\mathrm{V}$ with only slight increases in resistance over the lower voltage measurements, but with significant reductions in noise due to heating. This is equivalent to a current of 300 nA. By comparison R_{xy} could be measured at the lowest excitation voltage due to its magnitude being more than one hundred times smaller than that of R_{xx}. However, even at $3\,\mu\mathrm{V}$ the associated current is $3\,\mu\mathrm{A}$, a value most likely high enough to cause appreciable levels of sample heating.

The initial work at base temperature also showed a noticeable rise in temperature when sweeping the magnetic field at higher rates. The field was therefore quickly swept out to the maximum and the power supply left in persistent mode for the system to cool before taking measurements. The field was also swept slower over the ±1 T range in order to clearly see low field features such as AMR, and to avoid significant thermal hysteresis. Base temperatures measured via the $\mathrm{RuO_2}$ thermometer were found to be around 25 mK when applying

100 μV and around 40 mK when applying 300 μV.

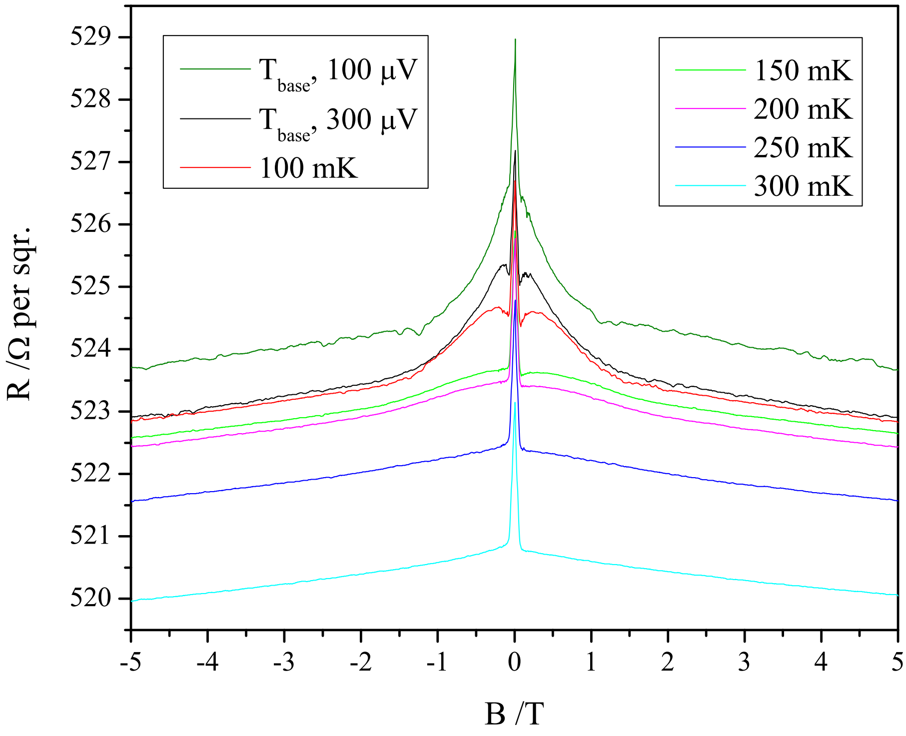

Figure C.2: Longitudinal resistance R_{xx} measured at base temperature, 100 mK, 150 mK, 200 mK, 250 mK and 300 mK whilst sweeping the magnetic field parallel to the current between ±5 T.

After this testing full R_{xx} measurements were performed at base temperature, 100 mK, 150 mK, 200 mK, 250 mK and 300 mK using a sweep rate of 0.2 T/min. These higher temperatures were attained by heating the sample space using the Kelvinox system. The temperatures specified are therefore those measured by the dilution refrigerator system thermometer in the helium mixture and not the RuO_2 resistor. However, periodic measurements of the RuO_2 resistance showed only slight increases above that specified as the measurements progressed due to the sweeping magnetic field. Figure C.2 shows R_{xx} datasets for all temperatures including a 100 μV measurement at base temperature.

All of the datasets show a very narrow peak at zero tesla. This comes about as the result of anisotropic magnetoresistance (AMR): the dependence of the

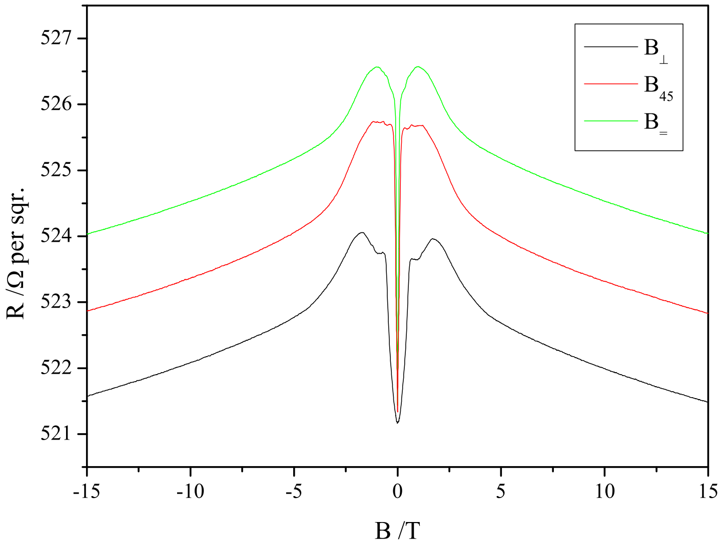

(a)

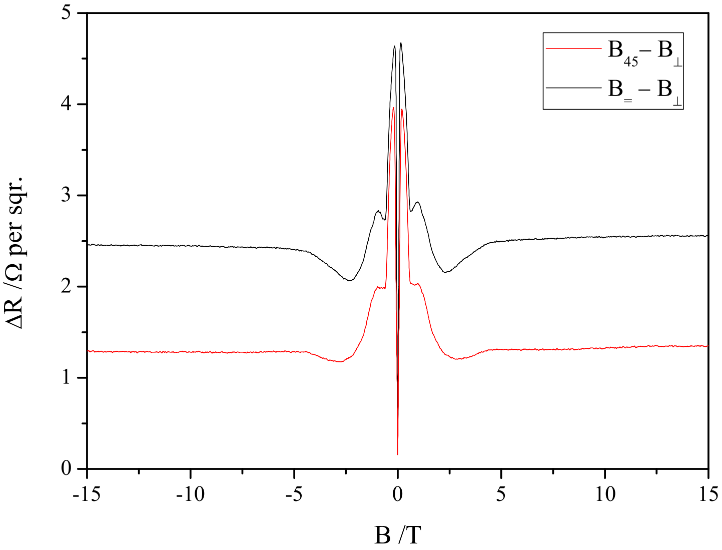

(b)

Figure C.3: (a) Longitudinal resistance measured within a helium-3 system close to 300 mK applying the magnetic field parallel (green), perpendicular (black) and at 45° (red) to the sample surface. (b) Subtracting the perpendicular-field data from both the parallel and 45°data results in a roughly flat plot above 5 T thus demonstrating that the high-field negative magnetoresistance is highly isotropic.

resistivity on the relative directions of the magnetisation, applied current and crystal orientation. Within (Ga,Mn)As this is caused by the effects of spin-orbit interactions on charge carrier scattering (Rushforth *et al.* (2006, 2009)). The application of an external magnetic field leads to the rotation of the sample magnetisation. The magnetisation then saturates in the direction of the applied field at a sufficiently high magnitude with typical saturation fields for (Ga,Mn)As being less than 0.7 T. The observed peak is therefore the difference in magnitude of the resistance with the magnetisation along the magnetic easy-axis to that of the magnitude with the magnetisation in the direction of the applied magnetic field.

For fields above the AMR peak at temperatures greater than 200 mK a smaller negative magnetoresistance is then observed which remains roughly constant all the way out to the ±5 T sweep range. This same behaviour is also seen within the lower temperature datasets above ± 2 T. High-field measurements performed within a helium-3 cryostat showed that this constant negative magnetoresistance persists to more than 15 T, and is isotropic with the magnetic field swept parallel, perpendicular and at 45° to the sample surface.

Figure C.3 shows the high field sweeps performed within the ^{3}He system with $B_\perp$ along the [110] direction parallel to the surface, but perpendicular to that of the dilution refrigerator data. This explains the different behaviour of this data to the dilution refrigerator measurements taken at 300 mK. Differing magnetic field directions were performed due to the limitations of the probe and system designs. This isotropic magnetoresistance is related to weak localisation which is caused by the destructive quantum interference of an electron with itself along self-intersecting scattering paths. The application of a magnetic field results in a shift in phase of the electronic wavefunction thus suppressing the effects of localisation and decreasing the sample resistance.

As well as this negative magnetoresistance, additional shoulders are seen in the lower temperature datasets either side of the AMR peak. Figure C.4a shows a comparison of the datasets shifted such that the resistances at -2 T are equal to that at 300 mK. This figure demonstrates the gradual evolution of these shoulders as the temperature is reduced below 200 mK. Figure C.4b then shows the datasets below 300 mK with both the low-field AMR and the high-field isotropic magnetoresistance removed by subtracting the 300 mK sweep without the additional shoulders.

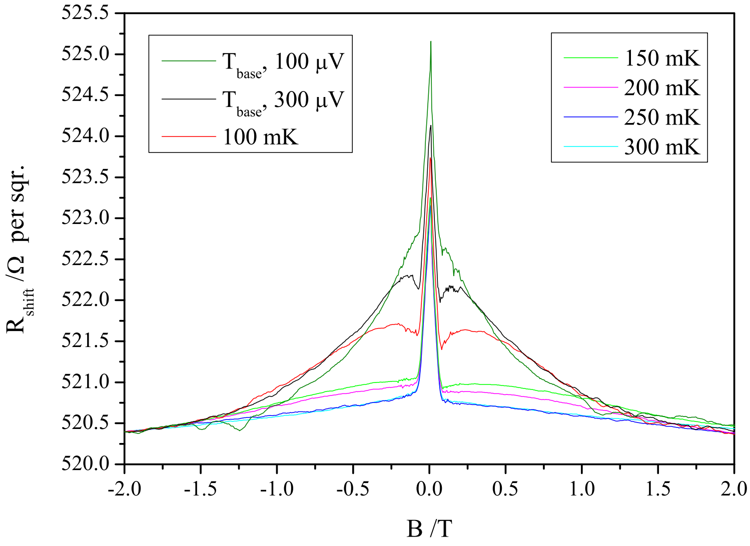

(a)

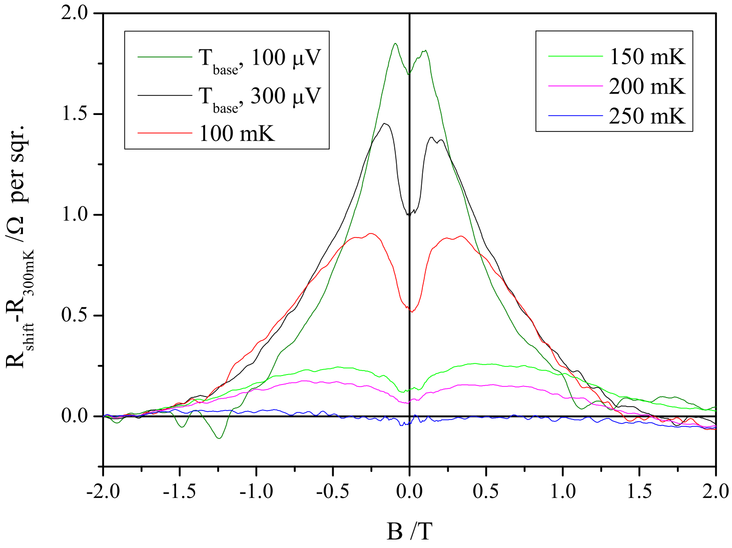

(b)

Figure C.4: (a) Shifted plots of the R_{xx} dilution refrigerator data shown in figure C.2 comparing the 300 mK sweep to the lower temperature datasets. (b) The same shifted data with the low-field AMR removed by subtracting the 300 mK data demonstrating the gradual development of the shoulders prominent in both the base temperature datasets.

Measurements of R_{xy} at base temperature were also performed between ±2 T with a sweep rate of 0.2 T/min. Figure C.5 shows this data after adjacent-average smoothing along with both the symmetric and asymmetric components calculated using equations (C.1) and (C.2) respectively.

$$R_{\mathrm{sym}} = \frac{R_{\mathrm{xy}}(\pm B \uparrow) + R_{\mathrm{xy}}(\mp B \downarrow)}{2} \tag{C.1}$$

$$R_{\mathrm{asym}} = \frac{R_{\mathrm{xy}}(\pm B \uparrow) - R_{\mathrm{xy}}(\mp B \downarrow)}{2} \tag{C.2}$$

The sharp peak observed in the symmetrical part of R_{xy} is again the result of AMR brought about by the rotation of the magnetisation. The unusual behaviour in the asymmetric component close to $B = 0$ is caused by hysteresis, and the resulting misalignment of the AMR peaks when applying equation (C.2) to the up and down sweeps. In an ideal case this asymmetric contribution should pass through the graph origin and arises from a combination of both the ordinary and anomalous Hall effects.

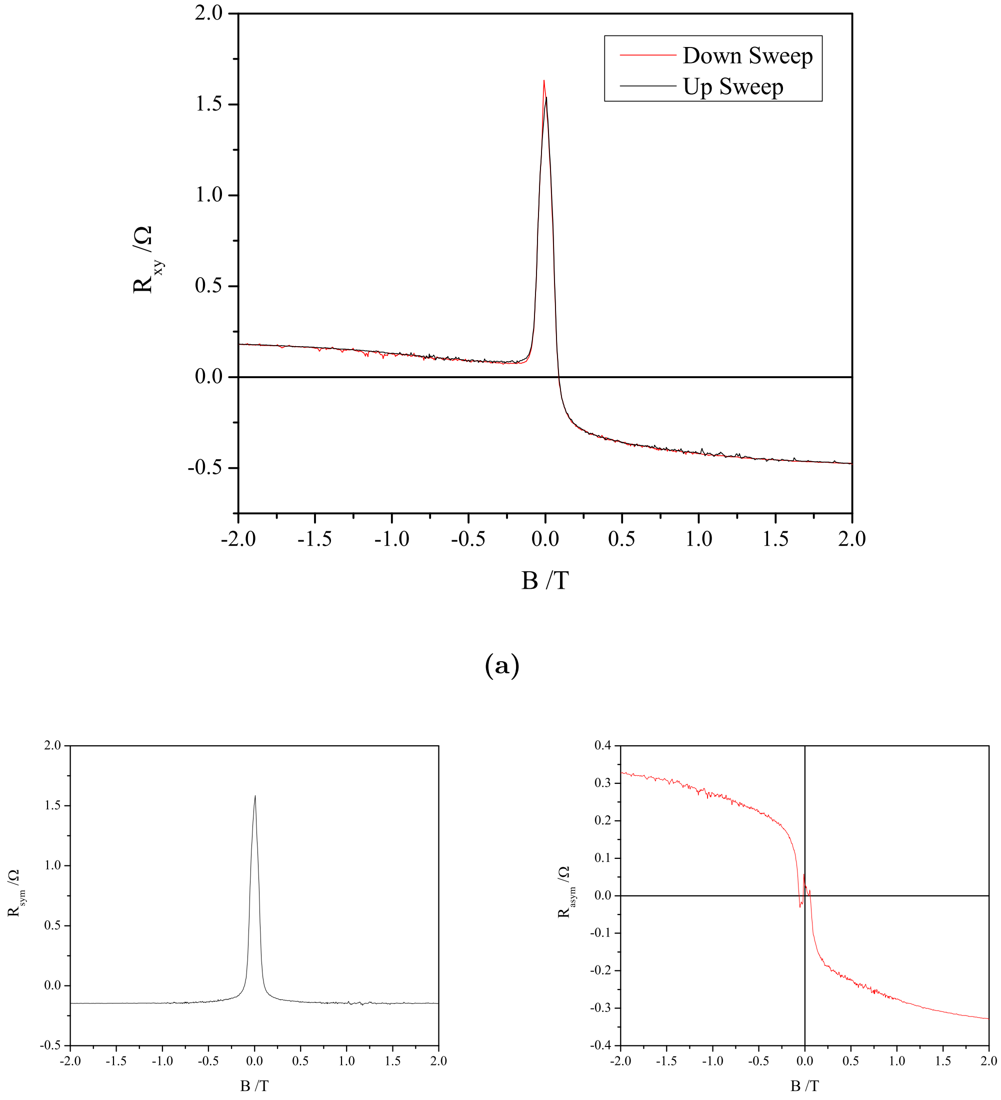

(a)

(b)

(c)

Figure C.5: (a) The transverse resistance R_{xy} measured at base temperature before separating both the symmetric (b) and asymmetric (c) components using equations (C.1) and (C.2) respectively.

References

Clarke, J. and Braginski, A. I. *The SQUID Handbook: Applications of SQUIDs and SQUID Systems, Volume 2*. Wiley, (2007).

Fagaly, R. L. ‘Superconducting quantum interference device instruments and applications’. *Review of Scientific Instruments*, **77** (10) 101101, (2006).

Jaklevic, R. C., Lambe, J., Silver, A. H., and Mercereau, J. E. ‘Quantum Interference Effects in Josephson Tunneling’. *Physical Review Letters*, **12** (7) 159–160, (1964).

Jaklevic, R. C., Lambe, J., Mercereau, J. E., and Silver, A. H. ‘Macroscopic Quantum Interference in Superconductors’. *Physical Review*, **140** (5A) A1628–A1637, (1965).

Josephson, B. D. ‘Possible new effects in superconductive tunnelling’. *Physics Letters*, **1** (7) 251–253, (1962).

Lounasamaa, O. V. ‘Dilution refrigeration’. *Journal of Physics E: Scientific Instruments*, **12** (8) 668–675, (1979).

Rushforth, A. W., Giddings, A. D., Edmonds, K. W., Campion, R. P., Foxon, C. T., and Gallagher, B. L. ‘AMR and magnetometry studies of ultra thin GaMnAs films’. *Physica Status Solidi (c)*, **3** (12) 4078–4081, (2006).

Rushforth, A. W., Výborný, K., King, C. S., Edmonds, K. W., Campion, R. P., Foxon, C. T., Wunderlich, J., Irvine, A., Novák, V., Olejník, K., Kovalev, A., Sinova, J., Jungwirth, T., and Gallagher, B. L. ‘The origin and control of the sources of AMR in (Ga,Mn)As devices’. *Journal of Magnetism and Magnetic Materials*, **321** (8) 1001 – 1008, (2009).

Sawicki, M., Stefanowicz, W., and Ney, A. ‘Sensitive SQUID magnetometry for studying nanomagnetism’. *Semiconductor Science and Technology*, **26** (6) 064006, (2011).